Observational Properties of Gigaelectronvolt-Teraelectronvolt Blazars and the Study of the Teraelectronvolt Blazar RBS 0413 with VERITAS

Güneş Demet Şentürk

Submitted in partial fulfillment of the

requirements for the degree

of Doctor of Philosophy

in the Graduate School of Arts and Sciences

COLUMBIA UNIVERSITY

2013

ABSTRACT

Observational Properties of Gigaelectronvolt-Teraelectronvolt Blazars and the Study of the Teraelectronvolt Blazar RBS 0413 with VERITAS

Güneş Demet Şentürk

Blazars are active galactic nuclei with a relativistic jet directed towards the observer's line of sight. Characterization of the non-thermal continuum emission originating from the blazar jet is currently an essential question in high-energy astrophysics. A blazar spectral energy distribution (SED) has a typical double-peaked shape in the flux vs. energy representation. The low-energy component of the SED is well-studied and thought to be due to synchrotron emission from relativistic electrons. The high-energy component, on the other hand, is still not completely understood and the emission in this part of the blazar spectrum can extend to energies as high as tera electron volts in some objects. This portion of the electromagnetic spectrum is referred to as the very-high-energy (VHE or TeV, $E > 0.1$ TeV) regime. At the time of this writing, more than half a hundred blazars have been detected to emit TeV gamma rays, representing the high energy extreme of these objects and constituting a population of its own. Most of these TeV blazars have also been detected in the high-energy (HE or GeV, 0.1 GeV $< E <$ 0.1 TeV) gamma-ray range.

In this work, we report on our discovery of the TeV emission from the blazar RBS 0413 and perform a detailed data analysis on this source, including contemporaneous multi-wavelength observations to characterize the broad-band SED and test various emission models for the high-energy component. Further, we extend our focus on the high-energy component to all archival TeV-detected blazars and study their spectral properties in the framework of GeV and TeV gamma-ray observations. To do this, we assemble for the first time the GeV and TeV spectra of a complete sample of TeV-detected blazars available in the archive to date. In the Appendix we present an analysis method for improved observations of large zenith angle targets with VERITAS.

Table of Contents

List of Figures

List of Tables

List of Abbreviations

AGN: Active galactic nucleus

APL: Absorbed power law

BL Lac: BL Lacertae

BLR: Broad line region

BPL: Broken power law

CFD: Constant fraction discriminator

CR: Cosmic ray

EAS: Extensive air shower

EBL: Extragalactic background light

EGMF: Extragalactic magnetic field

FADC: Flash Analog Digital Converter

FSRQ: Flat spectrum radio quasar

GeV: Giga electronvolt

HBL: High-frequency-peaked BL Lacertae

HE: High energy

HV: High voltage

IACT: Imaging atmospheric Cherenkov telescope

IBL: Intermediate-frequency-peaked BL Lacertae

IR: Infrared

L1: Level 1

L2: Level 2

L3: Level 3

L4: Level 4

LAT: Large area telescope

LBL: Low-frequency-peaked BL Lacertae

LIV: Lorentz Invariance Violation

LZA: Large zenith angle

MSCL: Reduced mean scaled length

MSCW: Reduced mean scaled width

MSL: Mean scaled length

MSW: Mean scaled width

NLR: Narrow line region

NSB: Night sky background

OSS: Optical support structure

PDE: Photon detection efficiency

PL: Power law

PMT: Photomultiplier tube

PSF: Point spread function

QE: Quantum efficiency

RMS: Root mean square

SED: Spectral energy distribution

T1: Telescope 1

T2: Telescope 2

T3: Telescope 3

T4: Telescope 4

TeV: Tera electronvolt

UV: Ultraviolet

VHE: Very high energy

VPM: VERITAS pointing monitor

Introduction

The highest energy phenomena in galactic and extragalactic scales have been among the most intensely investigated areas in astrophysics over the past decade or two. Its genesis, however, has its roots in early 1900's. The discovery of cosmic rays about a century ago is perhaps the first incidence that aroused the scientific curiosity about high-energy phenomena in the universe. This curiosity was enhanced by later discoveries such as active galaxies that first came into the picture in the optical band and extraterrestrial gamma-ray sources detected by military satellites. However, the development of the high-energy astrophysics into an established discipline took long due to the technically challenging nature of the observations.

Information that can be obtained from the high-energy phenomena is limited and tricky, still it is well-accepted that non-thermal emission involving relativistically accelerated particles and massive objects is in play. Therefore the observables expected from these phenomena include cosmic rays, neutrinos, gravitational waves and gamma rays. Cosmic rays reach the Earth in abundant amounts and they contain valuable spectral information. However, since they consist of charged particles, their trajectory is altered on their way to the Earth due to the inter- or intra-galactic magnetic fields, making it impossible for the terrestrial observer to trace them back to their source of emission. As for the neutrino observations, they have been actively in operation for several decades but present detectors are not sensitive enough to characterize the extreme astrophysical objects that harbor highest-energy phenomena. Gravitational waves on the other hand is an emerging experimental field, with no established results yet. It follows that gamma-ray astronomy is currently the best available and most promising option to study the high-energy astrophysical phenomena.

This work focuses on extragalactic high-energy phenomena, in particular on gamma-ray observational properties of blazars. Techniques used in very high energy gamma-ray astronomy are

described in Chapter 1: an overview of instrumentation and principles are given, with an emphasis on Imaging Atmospheric Cherenkov Telescopes. Chapter 2 is dedicated to the VERITAS instrument: hardware, electronics, and the analysis of VERITAS data are described. Chapter 3 portrays the general properties of active galactic nuclei (AGNs) and in particular blazars, the astrophysical objects that are studied in this work. Chapter 4 depicts our detailed analysis of the blazar RBS 0413 from a TeV perspective supported with multiwavelength data, in particular in the GeV band. Chapter 5 presents our study on spectral properties of TeV-detected blazars in the GeV-TeV energy band.

Part I

TeV Astronomy

Chapter 1

Cherenkov Technique

Very high energy (VHE or TeV, $E > 100$ GeV) gamma rays constitute the highest-energy band of the whole electromagnetic spectrum, with a commonly accepted lower bound of 100 GeV. This lower energy bound has somewhat instrumental origins: this is roughly the energy where the space-based telescopes become ineffective because of their limited collection area, while the current ground-based telescopes come into play with a decent sensitivity, extending up to energies of ~ 10 TeV. It should be noted that one of the main prospects of the next-generation ground-based gamma-ray telescopes is to reach a lower energy threshold with an increased effective collection area, thereby overlapping with space-based observations. Perhaps the main difficulty in gamma-ray astronomy is that the atmosphere is practically opaque to gamma rays. Space-based satellites prove to be useful for energies only up to ~ 100 GeV. Luckily, the interactions undergone by VHE gamma rays from the moment they enter the upper layers of the atmosphere are well understood, permitting the study of this otherwise inaccessible energy window of the EM spectrum, leading to the development of TeV astronomy as an independent discipline. To date, more than a hundred of galactic and extragalactic sources of VHE gamma rays have been detected and catalogued[1].

Techniques for ground-based indirect detection of VHE gamma rays have been explored and developed over the past several decades. A gamma ray entering the atmosphere initiates a cascade of electromagnetic interactions. The particles that are produced in these interactions move at

[1]For an up-to-date catalog of VHE sources, see http://tevcat.uchicago.edu/

relativistic speeds, exceeding the speed of light in air, hence inducing Cherenkov radiation. This Cherenkov emission in turn contains valuable information about the primary gamma ray and its source. In the following sections we describe the method that is used to detect VHE gamma rays with ground-based observatories, known as the Cherenkov technique, and give a historical background for the field of TeV astronomy. Then we discuss the techniques used in the Imaging Atmospheric Cherenkov Telescopes (IACTs) and introduce the VHE gamma-ray instruments that were used in the study presented in this work. Finally, we briefly describe the *Fermi* Large Area Telescope, whose public data were analyzed in this study.

1.1 Extensive Air Showers

1.1.1 Shower Formation

A gamma ray entering the outer layers of the atmosphere subsequently interacts with air molecules and initiates a cascade of electromagnetic interactions that develop and form extensive air showers (EASs). The dominant interactions responsible for the formation of gamma-initiated EASs are pair production and bremsstrahlung. The minimum energy for a photon to pair produce into an electron-positron pair is 1.02 MeV, which corresponds to the total rest energy of the created particles. The primary gamma ray ('primary' hereafter) pair-produces into an electron-positron pair after about one radiation length, that in turn emits gamma rays through Bremsstrahlung, and the process repeats, with new charged leptons ('electron' hereafter) created after each radiation length (see Figure 1.1 left). It is assumed that at each step, the newly created electrons share the total energy equally, and energy losses due to, e.g., ionization are negligible at this phase. As the shower develops, the average bremsstrahlung radiation losses per electron equal the ionization losses, which marks the "shower maximum", where the number of particles peaks. After this point, energy loss from ionization start to prevail and the shower energy attenuates with an exponential dependence on the radiation length [Aharonian and others, 2008b]. Typically, for gamma rays in the energy range $\sim$ 100 GeV to several tens of TeV, the shower maximum occurs at altitudes of $\sim 10-5$ km above sea level (ASL). For a gamma ray of 1 TeV energy, the shower maximum contains

$\sim 10^3$ particles and occurs at an atmospheric depth of ~ 9 radiation lengths (one radiation length is ~ 37 g cm^{-2}), that corresponds to an altitude of ~ 8 km ASL [Ong, 1998].

EASs can be caused by cosmic rays as well ('hadronic' EAS, see Figure 1.1 right). In cosmic-ray (CR) initiated air showers, particle cascades mostly involve hadronic interactions. Being much more abundant than gamma-initiated EASs, they constitute an overwhelming background for ground-based gamma-ray observations. Details on how to eliminate the CR background are discussed in Section 1.2.3.

1.1.2 Cherenkov Radiation

A charged particle that moves in a given medium with refractive index n causes polarization in nearby molecules, which subsequently radiate and return to their original state. The speed of light in the same medium is given by $c_n = c/n$, where c is the speed of light in vacuum. If the charged particle is traveling faster than c_n, the perturbed molecules emit the so-called Cherenkov light, characterized by constructive interference along a shock front. The power per unit frequency of Cherenkov light is approximately proportional to its frequency [Schwinger and others, 1998] and peaks in the blue/UV region, whereas the night sky background (NSB) from starlight is dominant in longer wavelengths. Another useful property of Cherenkov radiation from the point of view of gamma-ray astronomy is that it is emitted with a very small opening angle (see Section 1.1.3) and thus propagates mostly along the trajectory of the emitting particle, preserving the directional information of the primary. Most of the relativistic particles in the shower maximum of an EAS emit Cherenkov radiation, which propagates down the atmosphere with little attenuation and can be captured by a detector on the ground. The number of Cherenkov photons that are created in a given EAS is related to the energy of the primary.

1.1.3 Cherenkov Light Pool

The emission angle θ of the Cherenkov radiation from relativistic electrons in the cascade is given by the following relation:

$$\theta = \cos^{-1}(1/(\beta n)), \tag{1.1}$$

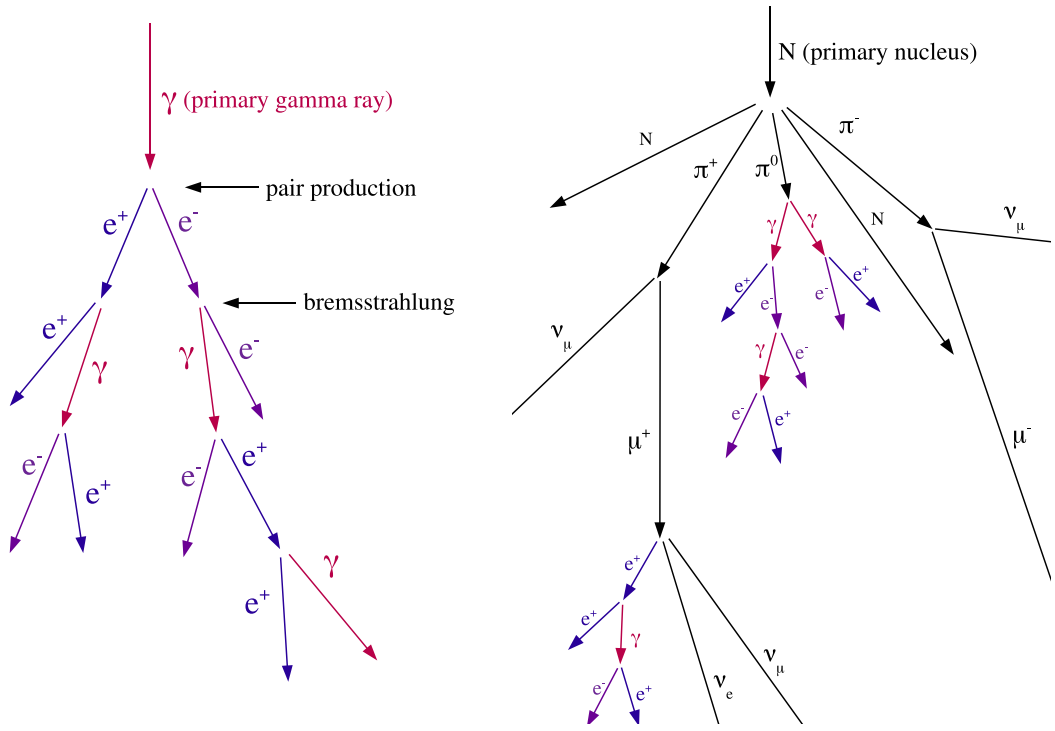

Figure 1.1: **Left:** Development of a gamma ray initiated extensive air shower. After one radiation length, the primary gamma pair produces. The electron-positron pair created in pair production undergo bremsstrahlung after another radiation length and emit secondary gamma rays. The process repeats and the emitting particles multiply geometrically about every two radiation lengths until the shower maximum is reached, which occurs at ~ 8 km above sea level for a typical 1 TeV primary gamma ray. **Right:** Development of a cosmic ray initiated (hadronic) extensive air shower. The primary particle is mostly a proton and can also be a heavier nucleus. This type of EAS involve hadronic interactions that generate many new particles including pions, kaons and baryons, that have large transverse momenta, resulting in a larger lateral spread compared to a gamma-initiated EAS. Neutral pions and secondary electrons in a hadronic shower initiate electromagnetic sub-showers, as shown in the diagram.

where β is the ratio of the speed of the relativistic particle to the speed of light in vacuum (c) and n is the refractive index of the medium. The refractive index of the air equals ~ 1.00028 for a wavelength of 350 nm, at 1 atm pressure, 20°C temperature and 50% relative humidity[2]. The refractive index is inversely related to temperature and humidity, but directly related to pressure, and therefore is an inverse function of the altitude. The emission angle θ (see Eq. 1.1) increases with decreasing altitude due to the inverse altitude dependence of the refractive index. As a consequence, the opening angle of the Cherenkov lightcone created by the relativistic electrons expands as they travel forward down the atmosphere, resulting in a circular uniform light pool with a blurry outer ring on the ground. A typical gamma ray will create a Cherenkov light pool with a radius of $\sim$ 120 m and a thickness of $\sim$ 1 m at the detector level (see Figure 1.2). The average number of Cherenkov photons that will reach the ground as a result of a 1 TeV gamma-ray EAS is about 3×10^6 [Ong, 1998]. The time it takes for a typical Cherenkov light pool to pass through a detector located on the ground is a few nanoseconds, requiring very fast electronics to record the information. Given its uniformity, a detector located anywhere in the light pool will be able to detect the air shower. Therefore, the *effective* collection area (effective area hereafter) of an atmospheric Cherenkov detector is equal to the size of the light pool which is around 5×10^5 m^2, or in other words much larger than its mirror collection area. Moreover, by placing multiple detectors within the area of the size of a typical light pool, one can increase the effective area of a TeV gamma-ray experiment.

1.2 Details of the Cherenkov Technique

The Cherenkov technique is based on extracting information from the light emitted at the shower maximum of an EAS. A camera composed of photomultiplier tubes (PMTs) as pixels is used to capture the faint Cherenkov flash. A mirror serving as a reflecting surface is used to focus the light onto the PMT camera, thereby increasing the physical collection area. PMTs have a peak sensitivity in the blue/UV range and make use of the photoelectric effect to convert the Cherenkov

[2]Calculated using http://emtoolbox.nist.gov/Wavelength/Edlen.asp (National Institute of Standards and Technology)

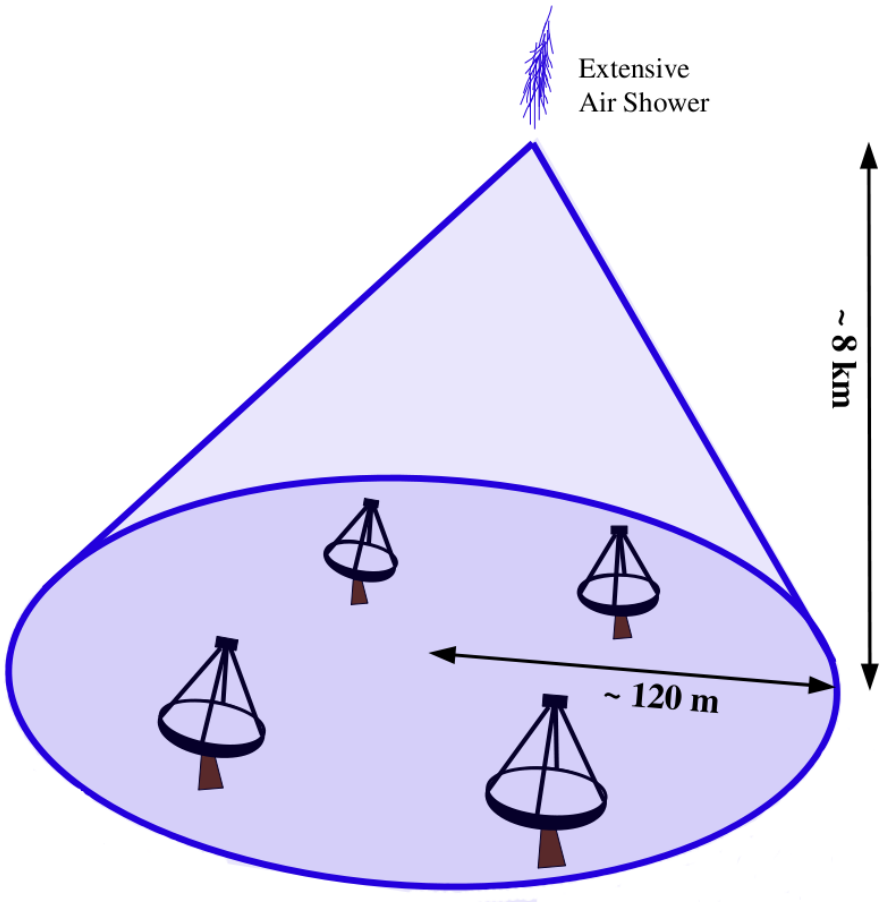

Figure 1.2: Cherenkov light pool that forms on the ground. For a typical extensive air shower initiated by a gamma ray of 1 TeV energy, the shower maximum occurs at an altitude of $\sim$ 8 km, and the Cherenkov photons reach the ground forming a light pool of radius $\sim$ 120 m.

light into an electric current. The electric pulse that is generated as a result of the Cherenkov photons that hit the PMT is then digitized and analyzed further.

1.2.1 Energy of the Primary

The number of relativistic particles that are present at the shower maximum is related to the primary gamma ray's energy. Most of these particles emit Cherenkov radiation, that in turn propagates down with some loss due to absorption and scattering through the atmosphere. Therefore, with a careful estimation of atmospheric losses, one can use the photon density information at the detector level to estimate the energy of the primary. This is done by means of simulations that take into account the atmospheric conditions, the altitude of the detector's location, the reflectivity of the mirror and the efficiency of the PMTs. The signal S detected at the PMT during the Cherenkov flash is expressed in units of photoelectrons with the following relation:

$$S = \int_{\lambda min}^{\lambda max} F_C(\lambda)\epsilon(\lambda)A\,\mathrm{d}\lambda \tag{1.2}$$

where $F_C(\lambda)$ is the number of Cherenkov photons per unit area (accumulated over a time window τ longer than the Cherenkov flash), $\epsilon(\lambda)$ is the quantum efficiency of the PMTs in use, and A is the collection (mirror) area. S is also referred to as the 'deposited charge'. The integral limits are set by the wavelength range to which the PMTs are sensitive. On the other hand, the PMTs also detect light from the NSB. In order to claim a detection, a reasonable signal-to-noise (S/N) ratio should be achieved. From equation 1.2, one can see that for a given quantum efficency and mirror area, the signal is directly related to $F_C(\lambda)$, which increases with the primary's energy. In other words, for a given instrument and NSB level, the S/N ratio increases with increasing gamma ray energy. In addition to this, the desired energy threshold of the instrument, if defined as the minimum gamma-ray energy with a detectable S/N ratio, depends on the quantities $\epsilon(\lambda)$, A, and NSB level. Quantitatively, the noise from the NSB is defined as follows:

$$B = \int_{\lambda min}^{\lambda max} F_B(\lambda)\epsilon(\lambda)A\tau\Omega\,\mathrm{d}\lambda \tag{1.3}$$

where $F_B(\lambda)$ is the NSB flux, defined as the number of photons per unit area per unit time, τ is the integration time, and Ω is the solid angle subtended by a PMT. The fluctuations are expressed by the square root of the noise level, such that $S/N = S/\sqrt{B}$. It follows that $S/N \ \alpha \ F_C(\lambda)\sqrt{\epsilon(\lambda)A/F_B(\lambda)\tau\Omega}$. Increasing the overall S/N ratio of an instrument would mean lowering the minimum energy at which a detection can be claimed, thus the threshold energy E_{th} is inversely related to S/N, in other words:

$$E_{th} \ \alpha \ 1/F_C(\lambda)\sqrt{F_B(\lambda)\tau\Omega/\epsilon(\lambda)A} \tag{1.4}$$

Equation 1.4 shows that there are several ways to lower the energy threshold for a VHE gamma-ray instrument. At the design level, one can increase the size of the mirror collection area A, which could be more easily done by using an array of small mirrors mounted together in a special arrangement (see 2.1.2). Other useful strategies would be to increase $\epsilon(\lambda)$ by using higher efficiency PMTs, and choosing the experiment site to be as dark as possible, to reduce $F_B(\lambda)$.

1.2.2 Sensitivity

In a general sense, for a given source flux, the sensitivity of the telescope depends on the collection area and the exposure time. However, for atmospheric Cherenkov telescopes, the field of view is overwhelmed by cosmic ray events that mimic the gamma ray events with their electromagnetic cascades and Cherenkov light generation. Thus the sensitivity of the instrument really depends on its efficiency to eliminate cosmic-ray background. The cosmic ray flux follows a power law of the form

$$F_{cr}(> E) \ \alpha \ E^{-a} \tag{1.5}$$

with an integral spectral index $a \sim 1.7$ in the energy range that is relevant for VHE gamma-ray astronomy [Weekes, 2003]. Therefore, the cosmic-ray background that the TeV telescope detects can be expressed as follows:

$$B = F_{cr}(E)A_{cr}(E)\Omega t \tag{1.6}$$

where A_{cr} is the energy dependent effective collection area for cosmic rays. Eliminating the cosmic ray events at the analysis level will decrease A_{cr}. Ω is the solid angle subtended by the telescope and t is total observing time. Similarly, the gamma-ray flux can be assumed to follow a power-law spectrum so that

$$F_\gamma(> E) \; \alpha \; E^{-b} \tag{1.7}$$

where the spectral index b takes a value between 1 and 4, and has an inverse energy dependence. The gamma-ray signal detected by the telescope during the same exposure duration t will be:

$$S = F_\gamma(E) A_\gamma(E) t \tag{1.8}$$

where A_γ is the gamma-ray collection area, which is a function of energy as well. The significance of the γ ray signal above the cosmic ray background is defined as $\sigma = S/\sqrt{B}$. It follows that the significance for a given energy can be expressed as

$$\sigma \; \alpha \; E^{a/2-b} A_\gamma(E) \sqrt{(A_{cr}(E)\Omega)} \sqrt{t}. \tag{1.9}$$

This expression tells us that the significance of a detection increases with the square root of exposure time in the background dominated regime. In terms of energy, given that b is typically greater than $a/2$, operating at the minimum possible energy would contribute to the detection significance. Most importantly, reducing the product $(A_{cr}\Omega)$ is essential to making it possible to detect a gamma-ray source. Since the TeV telescopes cannot distinguish between gamma-ray events and cosmic-ray events, this is done by eliminating the cosmic ray contamination at the analysis level. The principles of cosmic-ray background elimination are summarized in the next section.

1.2.3 Gamma/Hadron Separation

Like gamma rays, cosmic rays (mostly consisting of protons) initiate electromagnetic cascades that result in extensive air showers with relativistic electrons that emit Cherenkov radiation. These cosmic-ray-initiated air showers are much more abundant than their gamma-initiated counterparts

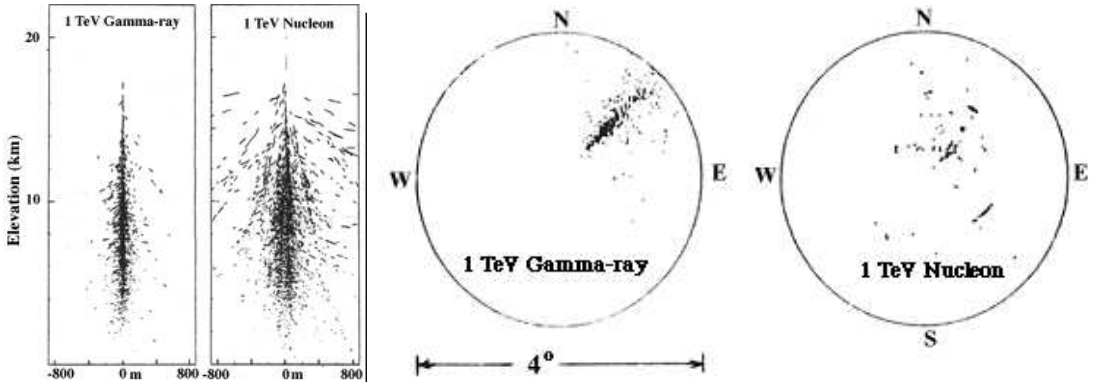

Figure 1.3: Simulated air showers for a 1 TeV gamma ray and a 1 TeV nucleon (figure from imagine.gsfc.nasa.gov). Gamma-ray-initiated showers develop with less lateral spread compared to the cosmic-ray-initiated ones (left), that is also manifested in the shower images on the camera plane (right).

and therefore constitute a heavy background for atmospheric Cherenkov detectors. To give an example, the cosmic ray integral flux above 1 TeV is 400 times higher than that of the Crab Nebula, the standard candle of TeV gamma-ray astronomy [Ong, 1998]. On the other hand, there are many properties of CR-initiated EASs that help distinguish them from gamma-initiated ones at the analysis level. One important aspect of CR-initiated showers is that they contain mostly hadronic particles that leave a relatively smaller fraction of energy for photon-initiated sub-showers. Thus for a given primary energy, a cosmic-ray-initiated EAS yields two to three times less Cherenkov light [Weekes, 2003]. Another favorable fact is that these two types of air showers undergo different processes of shower development and are distinguishable to a high degree of accuracy. In a cosmic-ray generated EAS, secondary particles have relatively larger lateral momenta, resulting in a cascade of particles that is laterally more spread apart compared to a gamma-ray air shower. The EAS images on the camera plane, that have roughly elliptical shapes, can be distinguished to a sufficient extent for identifying and rejecting cosmic-ray air showers (see Section 2.4.2). Figure 1.3 shows simulated air shower images along the atmosphere and at the detector level for both gamma-ray and CR primaries. In addition, a large lateral spread combined with a diversity of particle interactions in a CR-initiated EAS result in a fairly non-uniform photon distribution on the ground, whereas a gamma-initiated EAS forms a single uniform light pool (see Figure 1.4). Furthermore, cosmic rays reach the Earth isotropically and consequently will have randomly distributed orientations on the

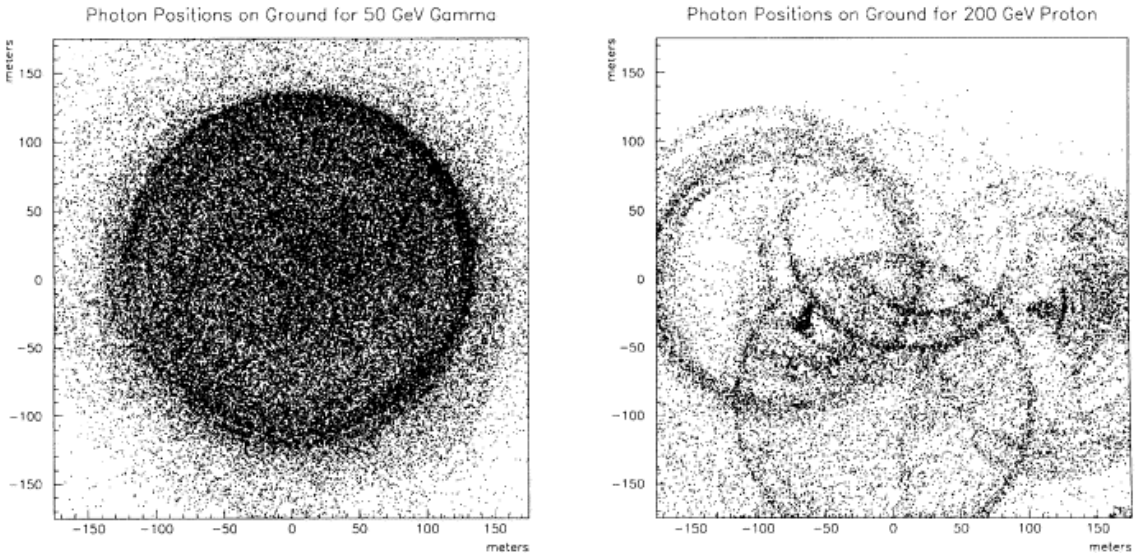

Figure 1.4: **Left:** Lateral distribution of Cherenkov photons on the ground for a gamma-ray initiated EAS. Photons are evenly spread in a single light pool. **Right:** Same distribution for a cosmic-ray initiated (hadronic) EAS. Multiple light pools are formed, with photons accumulated in rings, in an irregular fashion, following the irregular development of the air shower involving diverse types of particles (Figure from [Ong, 1998]).

camera plane. Gamma-ray images, however, will be pointing to the putative source location on the camera plane. In addition, ring-shaped Cherenkov images caused by local muons originating from cosmic-ray particle cascades, if crossing the camera, look very similar to EAS images and constitute background for the VHE gamma-ray data. Using stereoscopic observations eliminates this muon background, since these are locally formed images that cannot be seen by multiple telescopes at a time. It should be also noted that the time spread of a cosmic-ray air shower is about twice as long as a gamma-initiated one [Weekes, 2003].

1.3 TeV Instruments

1.3.1 Imaging Atmospheric Cherenkov Telescopes

The Whipple Telescope was the first Imaging Atmospheric Cherenkov Telescope (IACT) that successfully established the detection of a VHE gamma-ray source, the Crab Nebula [Weekes and others, 1989]. Whipple was installed in 1968 and originally it operated with a camera that consisted of a single

pixel (i.e. PMT), which did not permit imaging of the air showers. Hence, no gamma/hadron separation was possible and no source detection was made. In the mid 80's, the Whipple team developed a gamma/hadron separation technique that made use of imaging with a 37-pixel camera, which eventually led to the first unambiguous ground-based detection of a gamma-ray source [Weekes and others, 1989]. Whipple had many more detections and stayed in operation until 2011. By the 1990's, many IACT observatories making use of similar designs were set to explore the TeV gamma-ray sky (HEGRA [Pühlhofer and others, 2003], Durham Mark 6 [Armstrong and others, 1999], and Telescope Array [Aiso and others, 1997]. Some of these consisted of multiple telescopes that operated in array mode.

Operating in array mode makes it possible to see an EAS from different angles and thus permits stereo imaging, offering many advantages. To begin with, the 'head-tail ambiguity' issue (see A.1) that is typical of one telescope observations is mostly eliminated. This improvement permits better direction reconstruction, that has two outcomes: first is improved angular resolution, that also makes it possible to study the morphology of extended sources. Second outcome is more effective gamma/hadron separation, where the hadron identification is based on the isotropic distribution property of cosmic ray arrival directions. Another advantage of having multiple images of an EAS will permit more accurate energy estimation and therefore improve the energy resolution. Currently, the second generation of IACT arrays are in operation: VERITAS (4 telescopes) in Amado, AZ, and MAGIC (2 telescopes) in LaPalma, Canary Islands cover the northern sky while HESS (5 telescopes) in Namibia covers the southern sky. The next generation IACTs will consist of two arrays, one in the northern hemisphere and one in the southern hemisphere. The arrays will include telescopes of three different sizes, covering a broader energy range (below 100 GeV and above 100 TeV) and with sensitivity up to an order of magnitude higher [Actis and others, 2011].

1.3.2 Other Instruments

Other ground-based gamma-ray instruments that make use of the Cherenkov phenomenon include air shower arrays and solar power stations used as Cherenkov detectors. Air shower arrays comprise a large number of individual particle detectors that are spread on the ground or in water (e.g.

Milagro [Atkins and others, 2004]). Their collection area exceeds 10^4 m^2 and they operate with an energy threshold around the high energy end of the IACT range. In contrast to IACTs that perform pointed observations, these instruments operate continuously in survey mode. A new generation instrument of this type is HAWC (High Altitude Water Cherenkov Experiment), a water Cherenkov telescope currently under construction in Mexico. In the case of solar power stations, the idea is to use a large array of heliostats as light collectors and a central detector (e.g. STACEE [Hanna and others, 2002], CELESTE [Paré and others, 2002]). The large mirror area allows operating at somewhat lower energies compared to IACTs ($E_{\rm th} < 100$ GeV), where the cosmic ray contamination is much weaker. There is currently no operating instrument of this type.

1.4 GeV Instruments: *Fermi* Large Area Telescope

High Energy (HE or GeV, 100 MeV $< E <$ 100 GeV) gamma rays are detected through space telescopes. In this energy range, the gamma-initiated extensive air showers are too small to be detected by ground-based observatories, but the gamma-ray flux is large enough to allow direct detection in space, with limited collection area. Currently, the Large Area Telescope aboard the *Fermi* Space Satellite (*Fermi*-LAT) is covering the GeV gamma-ray band and provides complementary data for ground-based TeV instruments. Joint GeV-TeV studies are essential in characterizing the gamma-ray emission of astrophysical sources and *Fermi*-LAT observations were extensively used in the studies presented in Chapters 4 and 5 of this work. This section gives a brief description of the *Fermi* instrument.

Fermi-LAT is a pair-conversion γ-ray detector sensitive to photons in the energy range from below 20 MeV to more than 300 GeV [Atwood and others, 2009]. The instrument consists of a tracker-converter, a calorimeter and an anti-coincidence detector (see Figure 1.5). The tracker-converter consists of layers of high-Z material foils where the incident gamma ray pair produces ($\gamma \rightarrow e^+ + e^-$), and starts a subsequent elecromagnetic particle shower. The trajectory of the particles are tracked by position-sensitive silicon strip detectors placed between the high-Z layers. The calorimeter is located at the bottom of the converter-tracker array, measuring the deposited

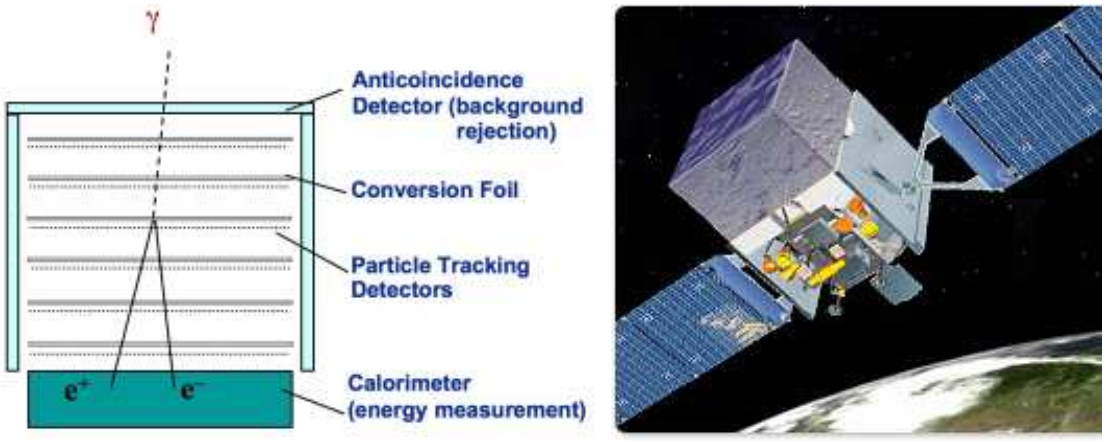

Figure 1.5: Schematic diagram of the *Fermi* instrument (left) and artist's impression of the *Fermi* satellite in Earth's orbit. Figure credit: http://www-glast.stanford.edu.

energy by the final particles that are formed along the converter-tracker. The anti-coincidence detector covers the converter-tracker unit and has a shielding function against the background created by charged particles.

Fermi was launched in June 2008, and has been taking science data since August 2008. It is mostly operated in sky-survey mode, and scans the whole sky every two orbits almost uniformly. This corresponds to an exposure of ~ 30 minutes for each region of the sky, every three hours. The effective collection area of the instrument is ~ 6500 cm^2 and the field of view is larger than 2 sr. The angular resolution is inversely related to the photon energy and the 68% containment radius is $\sim 0.8^\circ$ at 1 GeV [Nolan and others, 2012].

Fermi data has been public since the completion of the first year of its scientific data taking. The second and most recent *Fermi*-LAT source catalog (2FGL, [Nolan and others, 2012]) contains more than 1800 sources, including AGN, radio and Seyfert galaxies, supernova remnants, pulsar wind nebulae, and pulsars. Almost one third of the 2FGL sources have no positional association with a known objects. The catalog contains positional, temporal and spectral information of the sources in the energy range of 100MeV − 100GeV, as well as details about variability, spectral curvature, source extension. *Fermi*'s role in high-energy astrophyics is crucial not only due to its unique and critical energy coverage but its continuous all-sky observations that provide invaluable guidance for ground-based gamma-ray observatories that operate in pointing mode.

Chapter 2

VERITAS Instrument

VERITAS (Very Energetic Radiation Imaging Telescope Array System) is the Cherenkov Telescope array that was used for the TeV data analysis in this work (Figure 2.1). It is situated in Fred Lawrence Whipple Observatory near Tucson, Arizona, at +31 40' 30.21", -110 57' 7.77"; altitude 1268 m (4159 ft). VERITAS has a diverse science program including a variety of sources such as extragalactic objects (blazars, starburst galaxies, galaxy clusters), galactic objects (pulsar wind nebulae, supernova remnants, X-ray binaries), dark matter candidates (dwarf galaxies), gamma-ray bursts following alerts from various space telescopes, and our own galactic center. Observations started in winter 2005 with a single telescope. Additional telescopes were added subsequently, and the full array, comprising of four IACTs, saw first light in fall 2007. VERITAS takes data from September to June each year and shuts down during the Monsoon season (July-August) since the telescopes cannot operate at high humidity or under precipitation. After the start of full operations, VERITAS underwent many upgrades over time; including a new mirror alignment technique (see Section 2.3.6), relocation of Telescope 1, new trigger system, and camera upgrade. The relocation of Telescope 1 (T1) that was formerly too close to Telescope 4 resulted in an improvement in integral flux sensitivity of $\sim$ 30% for energies above 300 GeV [Perkins and others, 2009]. The VERITAS array layouts before and after the relocation of T1 are referred to as "old array" and "new array", respectively. The trigger upgrade consisted of redesigning the "level 2" trigger (see Section 2.2) to achieve a faster trigger system that allows for a better background rejection and lower

Figure 2.1: The VERITAS observing site. The array, composed of four imaging atmospheric Cherenkov telescopes surrounds the control building.

energy threshold [Schroedter and others, 2009]. The camera upgrade was carried out by replacing of the original "photomultiplier tubes" (see Section 2.1.3) with higher efficiency ones. Naturally, software programs that are used to control different parts of the system during operations and several independent data analysis packages are being modified and improved constantly. Currently, VERITAS can detect a gamma-ray source with a flux level of 1% of the Crab Nebula flux in less that 30 hours. In the first part of this chapter, we describe the current (i.e. as of spring 2013) status and performance of the array and give an overview of data taking modes, as well as regularly performed calibration works. In the second part, we describe the off-line analysis prodecure of the VERITAS data.

2.1 Structure and Hardware

A VERITAS telescope is seen in Figure 2.2: it consists of an altitude-over-azimuth positioner and a welded steel optical support structure (OSS) that bears the mirrors, the camera box and a counterweight. The reflector dish, with a focal length of 12 m follows the Davies-Cotton solar furnace design [Davies and Cotton, 1957] and consists of 350 hexagonal mirror facets that are arranged to form a concave spherical surface. The diameter of the reflector dish is 12 m, which is equal to its

Figure 2.2: A VERITAS telescope consisting of a 12 m mirror dish mounted on a welded steel optical support structure. The camera box kept across the reflector with quadrupole arms, balanced with a counterweight at the back can be seen.

radius of curvature. Quadrupole arms extending out from the OSS bear the camera box, such that the camera is placed at the focal plane. The camera box is balanced by the counterweight at the back of the OSS.

2.1.1 Tracking

VERITAS telescopes perform pointed observations and are maneuvered with a commercially manufactured altitude-over-azimuth positioner. The slew speed of the telescopes is 1° per second, and the positioner can be safely operated under wind gusts of 30 MPH. Fine-tuning of the pointing is achieved by the VERITAS pointing monitors (VPMs), that use the observed star field to calculate the pointing direction. A pointing monitor system is mounted on each telescope's OSS, consisting of a sky camera, a focal plane camera, and a control computer connected to the cameras. The information gathered by the pointing monitors is used to make corrections to the pointing in the offline analysis package, and also to improve the accuracy of the tracking software that controls and monitors telescope motion. VPM provides a pointing accuracy of < 50 arc seconds.

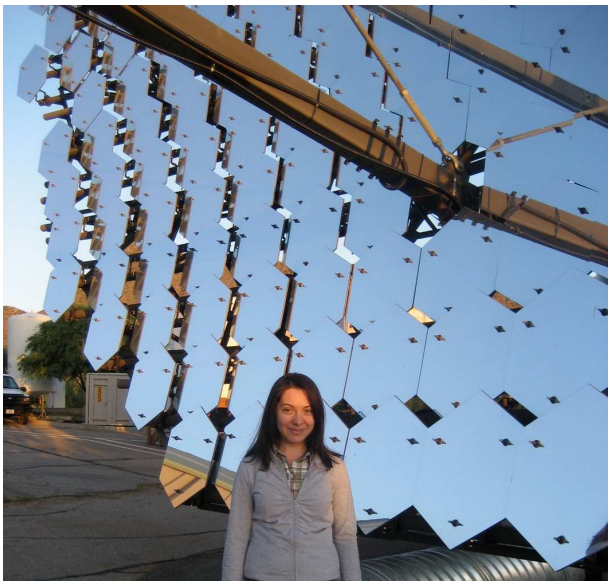

Figure 2.3: Author in front of the reflector dish of the Telescope 4. Hexagonal mirrors are slumped with a curvature radius of 24 m and mounted on the OSS that in turn has a curvature radius of 12 m. Each mirror is attached to the OSS frame by three adjustable bolts. Figure credit: R. Mukherjee, VERITAS Collaboration.

2.1.2 Optics and Light Collection

The mirror facets that constitute the reflector dish are of hexagonal shape, slumped with a curvature radius of 24 m, and made of glass coated with aluminum and anodized. Each facet has an area of 0.322 m^2 and is attached to the OSS by three bolts that are arranged in a triangular shape (see Figure 2.3). The alignment of a given mirror is done by adjusting the height of these bolts (see Section 2.3.6). The average mirror reflectivity of the array makes a plateau between 370-450 nm around the value of $\sim 85\%$. The Cherenkov light reflected on the mirror surface is focused on the camera pixellated with circular photomultiplier tubes (PMTs), located at the focal plane, 12 m from the center of the dish. To compensate for the gaps between the PMTs and to maximize the light collection efficiency of the camera, a so-called light cone is placed in front of each PMT. Light cones have hexagonal opening and circular bottom that coincides with the PMT entrance window. They are stacked together on a plate that is mounted in front of the camera (the light cone plate). Figure 2.4 shows the camera with the light cone plate. The camera is installed in such a way that the opening ends of the light cones coincide with the focal plane. The light cones were measured

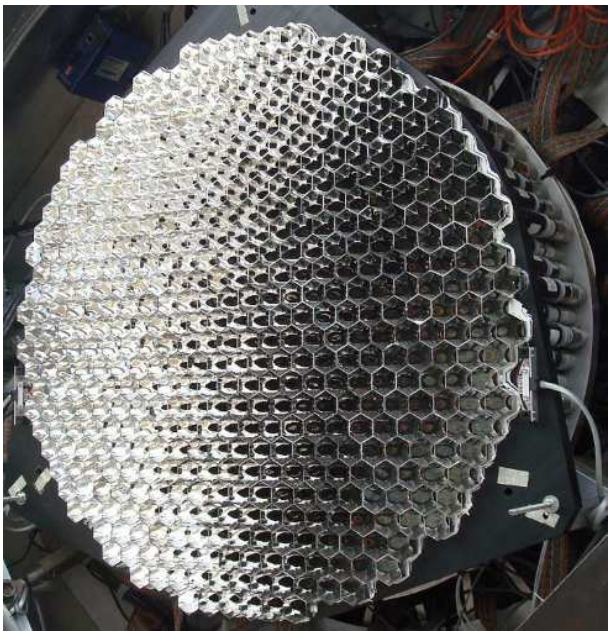

Figure 2.4: A VERITAS camera with 499 PMT pixels and a light cone plate mounted in front of the PMTs. Figure from [Griffin and others, 2011].

to increase the collected light by a factor of $\sim 25\%$. Each PMT views a solid angle of 0.15° in the sky and the total field of view of the camera is 3.5°.

2.1.3 Camera and PMTs

PMTs convert the Cherenkov light into an electrical signal. VERITAS is currently using R10560-100-20 MOD PMTs from Hamamatsu, that were installed during the summer of 2012, as part of the VERITAS upgrade program [Kieda, 2011]. The PMTs have a diameter of 1 inch and a UV-glass entrance window. Figure 2.5 shows the schematic structure of a PMT: it consists of a photo-cathode next to the entrance window, a series of electrodes called dynodes, and an anode at the end of the tube. A high voltage (HV) is applied acros the PMT. A Cherenkov photon entering the PMT window hits the photo-cathode and frees an electron from the photo-cathode material: this is called a photo-electron. Due to the electric field across the tube, the photo-electron moves forward and strikes the first dynode where it causes the release of several secondary electrons. The group of electrons move further down, strike the next dynode, and each one pulls out several more secondary electrons that will move further down the tube. The process is repeated at every dynode,

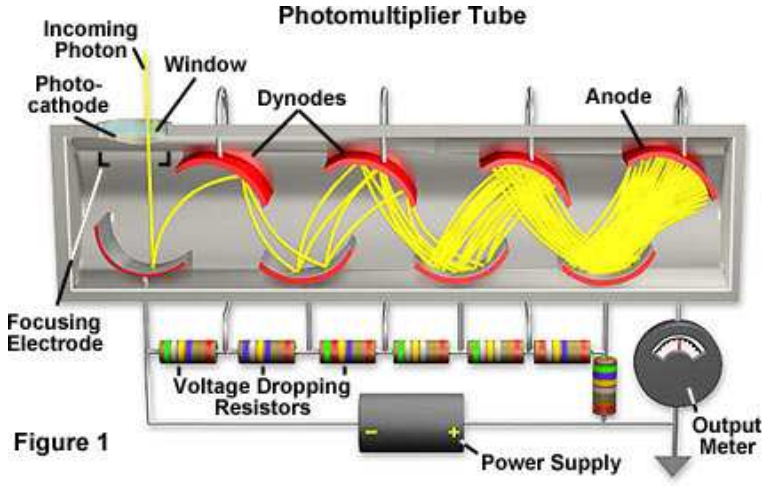

Figure 2.5: Schematic representation of the inner structure of a photomultiplier tube (PMT). Figure credit: Hamamatsu Photonics.

through which the number of electrons is geometrically multiplied and a current is generated at the anode. A VERITAS PMT contains 10 stages of dynodes and it is operated at a gain of 2×10^5, thus for each Cherenkov photon that creates a photo-electron, on average 2×10^5 of secondary electrons are generated. Figure 2.6 shows a PMT pulse from a data run in units of digital counts, recorded by the 'flash analog digital converter' (FADC) located at the PMT's signal output (see Section 2.2.2). A photoelectron corresponds to $\sim$ 5.5 digital counts, calculated as the total area under the pulse.

The PMTs are expected to age during their operation, due to the charge accumulation at the anode. This is important for VERITAS since the night sky background (NSB) causes a steady current of a few μA during normal operations. The current PMTs are expected to undergo a drop of 25% in gain over four years of operation, which will require a regular readjustment of the gain. Figure 2.7 shows the photon detection efficiency (PDE) measurements taken by two separate groups in VERITAS (UCSC and Purdue). A scaling factor of 74% is present between the UCSC and the Purdue University results, partly due to systematic errors in calibration. In the wavelength range of interest, the PDE of the PMTs was measured to be $\sim$ 30%, which is $\sim$ 90% of the Hamamatsu specifications for quantum efficiency (QE). This scaling factor of $\sim$ 90% between the measurements (PDE) and the specifications (QE) corresponds to the photoelectron

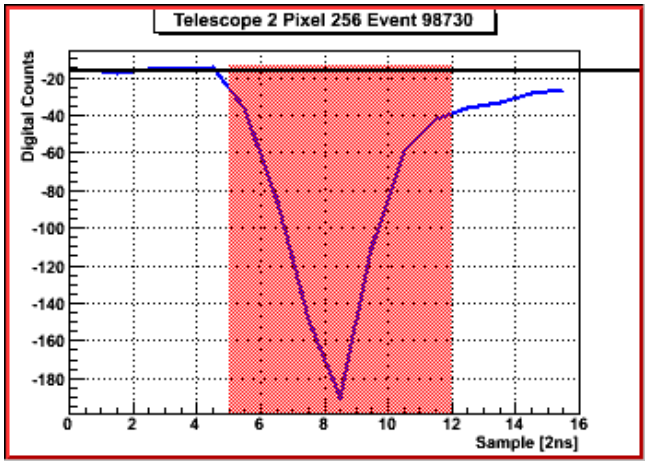

Figure 2.6: An actual Cherenkov pulse that is generated in a PMT pixel, from VERITAS data. The signal is sampled every 2 ns and recorded in units of digital counts (dc).

collection efficiency of the PMTs. With a photoelectron collection efficiency of $\sim 90\%$ and given the Cherenkov light spectrum, the average fraction of Cherenkov photons that are expected to be detected is $\sim 23\%$, that is $\sim 35\%$ higher compared to the performance of the former Photonis XP 2970 PMTs [Otte and others, 2011].

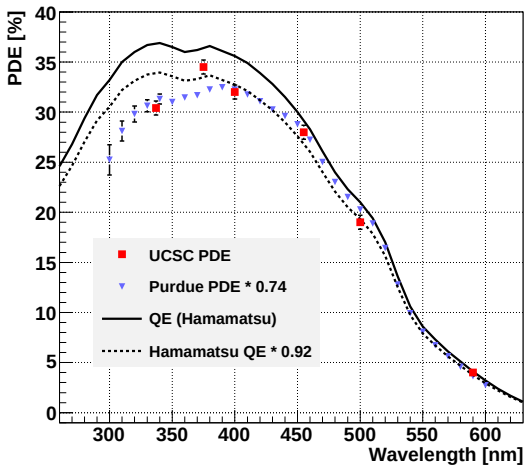

Figure 2.7: Photon detection efficiency (PDE) as a function of wavelength for the VERITAS R10560-100-20 MOD photomultipler tubes from Hamamatsu and measurements made by VERITAS in the lab [Otte and others, 2011]. See text for details.

2.2 Trigger and Data Acquisition System

The night sky, even in darkest conditions, contains an extensive amount of light that is detectable by the VERITAS PMTs and therefore represents a huge source of background. Without a trigger mechanism that helps eliminate irrelevant detections, it would not be possible to distinguish and capture extremely scarce air shower events. VERITAS uses a three-level trigger system [Weinstein and others, 2007] that significantly reduces the background from NSB fluctuations and Cherenkov radiation from local muons that are generated in cosmic-ray-initiated air showers.

2.2.1 Trigger Steps

The first trigger step in this three-level chain operates at the individual pixel level, referred to as pixel trigger or level 1 (L1) trigger, and provides a rejection mechanism for NSB fluctuations based on the output pulse amplitude of the PMTs. NSB fluctuations that are detected by the PMTs are more abundant than the air showers, but they create weaker signals at the PMT output. Therefore setting a minimum threshold voltage for the PMT pulses will reject most of the signal contamination caused by NSB fluctuations. This is achieved with the following technique: the output of each PMT is connected to a "constant fraction discriminator" (CFD) circuit that generates an output if the incoming pulse from the PMT exceeds a pre-set threshold voltage, referred to as CFD threshold (more below). CFD thresholds depend on the NSB level and are determined by taking a bias curve (see Section 2.3). VERITAS currently uses three different CFD threshold settings: 45 mV for regular dark sky observations, 60 mV for regular moonlight and 25 mV for bright moonlight observations. Naturally, the CFD thresholds are raised when the NSB levels increase. The lower thresholds in the case of bright moonlight observations is due to the simultaneous reduction applied to the PMT high voltage (see more in Section 2.3).

The second step of the trigger chain occurs at the telescope level and is based on temporal and geometric requirements on the L1 signals received from individual channels. This is called the pattern trigger or the level 2 (L2) trigger. To reject random NSB fluctuations, it is essential to

reduce the coincidence resolving time between triggers originating from the same EAS event. In other words, the signal arrival times from individual PMT channels should be as closely packed as possible. On the other hand, for a given shower event, the amount of received Cherenkov light varies from pixel to pixel. Consequently, the corresponding pulse amplitude varies accordingly as well. It follows that, if the crossing time of a constant threshold value is used for trigger, pulses with different amplitudes will cross that specific value at different times, causing an undesirable dispersion in trigger time. The CFDs come into play to alleviate this problem and reduce the time gap between L1 pulses regardless of their amplitude. In other words, the use of CFDs ensures that the time delay occurring between the individual PMT channel triggers is kept at a minimum level for a Cherenkov event, unlike random NSB fluctuations. With the addition of the geometric requirement, an L2 trigger at the telescope level is formed when at least three adjacent PMT channels send an L1 signal within a time window of 6 ns.

The third and last level in the trigger scheme is the array trigger, or the level 3 (L3) trigger, that is intended to distinguish the signals that are detected simultaneously on the array level. In order for an L3 trigger to occur, L2 signals from at least two telescopes (i.e. coincidence multiplicity of two) are required to arrive within a coincidence time window of 100 ns. There are two factors that create relative delays and affect the arrival times of L2 signals. First is the relative length difference of the cables that transmit the L2 signal from each telescope, which is calculated and corrected for precisely. The second factor arises from the relative distance of the telescopes from a given air shower, that becomes more significant in case of large zenith angle observations. The relative delay caused by this second factor is corrected for by taking into account the pointing of the observation and the location of each telescope. The L3 trigger is particularly important in rejecting the L2 signals caused by local muons that originate from cosmic ray air showers, since the Cherenkov light from these muons is produced nearby and usually cannot be seen by more than a telescope. See Figure 2.8 for a detailed diagram representing VERITAS trigger steps.

The time during which data is read out and the L3 is suppressed is referred to as the “dead time” of the array. A stable L3 trigger rate is desired in order to collect data with a reasonable dead time. Currently, the L3 trigger rate of 4-telescope VERITAS observations with a telescope

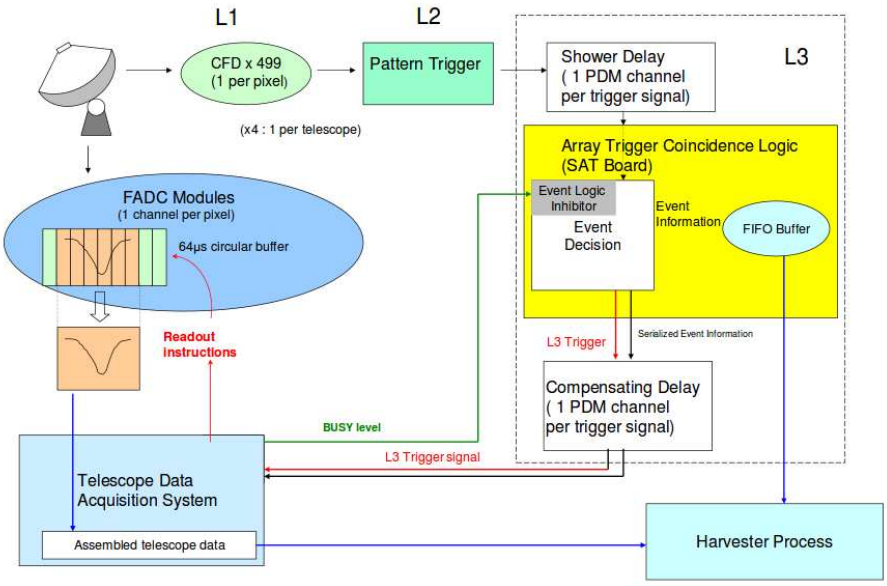

Figure 2.8: Schematic diagram that shows the communication between the three-level VERITAS trigger system and the data acquisition. Figure from [Weinstein and others, 2007].

multiplicity of two in the typical elevation range ($> 55°$) is around 350-400 Hz, with a dead time of $\sim 12 - 15\%$. Trigger rates are inversely related to the CFD thresholds. Increasing the CFD thresholds will in turn increase the energy threshold of the system, whereas decreasing the CFD thresholds will increase the trigger rate and consequently the dead time. So it is essential to determine an optimum CFD threshold for a given sky brightness, in other words NSB level (see Section 2.3 for details).

2.2.2 Data Acquisition

Once an L3 trigger is received, the system switches to a data reading mode during which no more L3 trigger can be formed, and the signal that caused the L3 trigger is read from a buffer and recorded. Each PMT channel is connected to a flash analog/digital converter (FADC) module that divides the signal in 2 ns samples, digitizes it in units of digital counts, and stores it in a buffer memory. As a result of the L3 trigger, each telescope receives a signal that orders the data acquisition system to read out a 16 sample portion of the FADC buffer after skipping a lookback time of ~ 3 μs. This lookback time accounts for the time elapsed between the formation of the L2 trigger and the

reception of the L3 trigger.

The data from each telescope along with additional information such as a GPS time stamp and an event number are then collected by a program called "Harvester". Harvester combines the data that is received from the telescopes and the L3, which it stores in a custom file format (VERITAS Bank Format, VBF). Another program that runs on the Harvester machine is Quicklook, which performs a real-time analysis while the data is being taken. Quicklook is useful for diagnostic purposes since it allows the monitoring of each trigger level. In addition, it carries out a preliminary signal extraction that helps the observers catch any unusually high flux from a target, that could indicate a gamma-ray flare.

2.3 Observing Modes and Calibration

2.3.1 Data Runs

VERITAS performs pointed observations and takes data in 20 or 30 minute durations. Unless a special elevation is required, a target is observed while it is above 55° elevation. Low elevation observations (or large zenith angle, LZA) can be performed down to 25°. The default VERITAS observation mode is called the "wobble mode", in which the telescopes point at a location 0.5° offset from the target. This method allows simultaneous background data taking at the expense of a slight drop in camera acceptance (more detail in 2.4.4). Observations are made with four alternating wobble offset directions (north, east, south, west) to eliminate biases that could occur from inhomogeneities in camera acceptance, due to the fact that it has a slight zenith angle dependence (see 2.4.4.2). For extended sources, a slightly larger offset of 0.7° is used in order to allow for morphology studies.

2.3.2 Flasher Runs

In order to achieve a bias-free analysis of the VERITAS data, one needs to perform a pixel-based calibration, since the PMT response varies across the camera. For this purpose, a two-minute flasher run is taken on a nightly basis. This is done by illuminating the telescopes uniformly with

an LED flasher that pulses at a rate of 300 Hz. For flasher runs, L2 trigger is created externally, with a telescope multiplicity requirement of four instead of two. The signal that is formed at each PMT in all four telescopes as a response to every flasher pulsation during the 2 minute run is read and recorded. Flasher data is used in the offline data analysis software (see 2.4.1) to correct for gain and timing differences in PMTs for all the data runs of the relevant night. If the high voltage and/or CFD threshold settings are changed for special conditions (e.g. moonlight observing) within a given night, additional flasher runs are taken.

In addition to the relative gain corrections that are applied at the data analysis level, a "flat-fielding" is performed across each camera once every two-three months. This consists of adjusting the high voltage applied to each PMT in such a way that a uniform signal is obtained at each FADC. On a flat-fielded camera, the spread of the relative gain distribution is around 0.02 (see Figure 2.12), and increases with time as a result of the fact that pixels age at different rates. A new flat-fielding is applied when the spread reaches a value of ~ 0.05. The most recent flasher run is used for the calculation of new HV adjustments.

2.3.3 Pedestals

In order to determine if a given PMT pulse originates from Cherenkov light or not, an accurate measurement of the NSB fluctuations is essential. Since the PMTs are AC coupled, the mean value around which they fluctuate as a result of the constantly present NSB light is reduced to zero. On the other hand, FADCs are only able to record the NSB fluctuations that are above the zero level. To be able to cover all fluctuations above and below zero, an offset is introduced by adding a small bias voltage to the signal. For NSB measurement, the array is externally triggered at a rate of 1 Hz, this is referred to as "pedestal". This simultaneously added pedestal is free of Cherenkov light, and the variance of the pedestal depends on the NSB level. A rate of 1 Hz during a 20-30 minute run provides enough statistics for determining the NSB level for that specific run. This information is then used in "image cleaning" for deciding whether or not a signal is due to Cherenkov light (2.4.1).

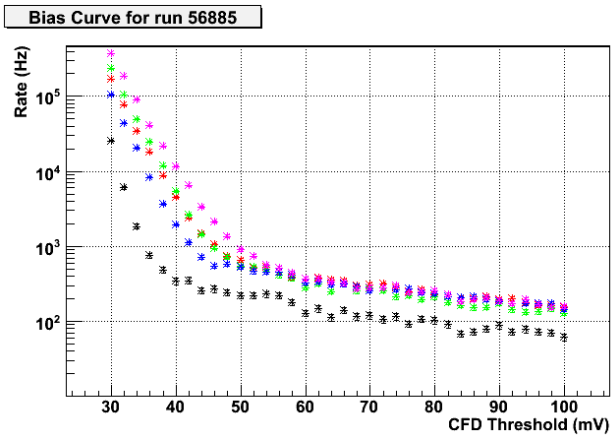

Figure 2.9: A dark sky bias curve from May 2011. Red, green, blue and pink markers represent L2 rates of the telescopes T1, T2, T3 and T4, respectively. Black markers represent the L3 rate with a telescope multiplicity of two. Note that even though the T4 L2 rate is higher than the rest for CFD thresholds below 50 mV, the overall L3 rate is well suppressed down to 45 mV.

2.3.4 Bias Curve

A bias curve is a plot of the trigger rate as a function of CFD thresholds taken on a monthly basis for dark and bright fields of view separately. A dark sky bias curve from May 2011 is shown in Figure 2.9. In the region where the CFD thresholds are low, the NSB fluctuations dominate and the trigger rates undergo a steep increase. On the other hand, a flat dependence is observed around 45 mV and beyond, where the triggers are dominantly due to air showers. Note that the NSB effects on L2 triggers are consistently higher than the L3, affirming the advantage of the array trigger system (in this case with a telescope multiplicity of two) in rejecting the accidental NSB triggers. The purpose of taking a bias curve is to determine the optimum CFD threshold for a given NSB level.

2.3.5 Pointing Monitors

Calibration measurements for pointing monitors (VPM, 2.1.1) are performed on a monthly basis under bright moonlight. ON-axis optical PSF (point spread function) measurements are also made simultaneously with this procedure, using the same data. See Figure 2.10 for various containment values for Telescope 1 (T1), from a PSF measurement made in March 2013. The VERITAS angular

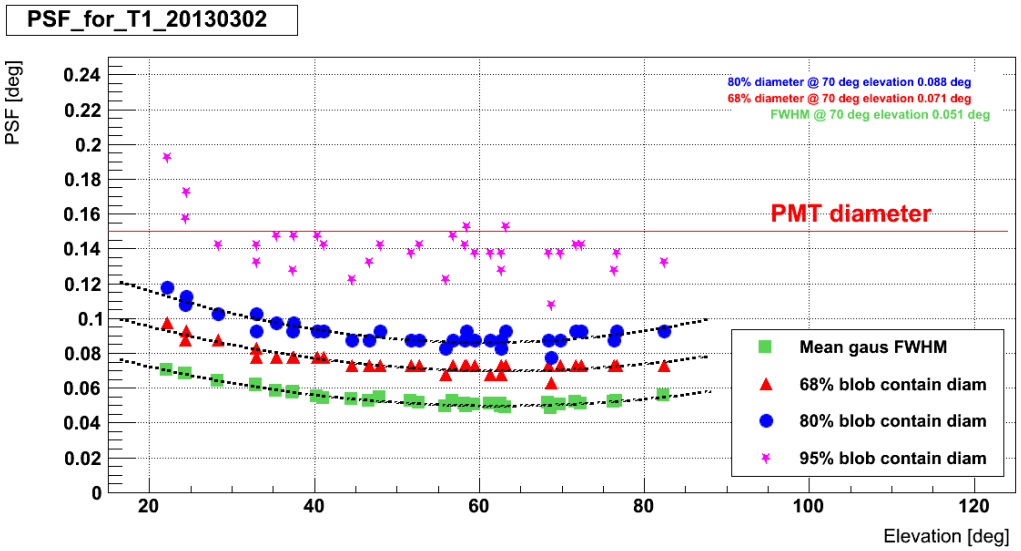

Figure 2.10: Point spread function (PSF) for Telescope 1 (T1) plotted against elevation, as of March 2013. At the typical observing elevation of 70°, 80% containment diameter, 68% containment diameter, and FWHM are 0.09°, 0.07°, and 0.05°, respectively. Figure credit: D. Gall, VERITAS Collaboration.

resolution is generally quoted as 68% containment radius, and is less than 0.04° for the standard elevation range ($> 55°$), in this recent T1 measurement. VPM calibration results are used to decide whether "TPoint correction" measurements are needed as well. TPoint is a model that describes the pointing offsets as a function of the pointing direction, by taking into account parameters like the change in shape of the OSS with elevation angle. TPoint corrections are applied to the tracking control software, and are usually performed once or twice a year.

2.3.6 Mirror Reflectivity and Alignment

The mirror reflectivity is tested at the beginning, around the middle and at the end of each season. This is done by removing 12 sample facets from each telescope, 4 from the top, 4 from the middle and 4 from the bottom parts. Each mirror facet is tested at three spots (high, low, center). If the reflectivity of a given sample of mirrors is found to be too low compared to a reference mirror, all facets in the corresponding group are re-coated. Figure 2.11 shows average reflectivity of each telescope as of March 2013, after a mid-season reflectivity check. Degradation in reflectivity due to dust and dirt is handled by washing the mirrors with soap and water on a monthly basis.

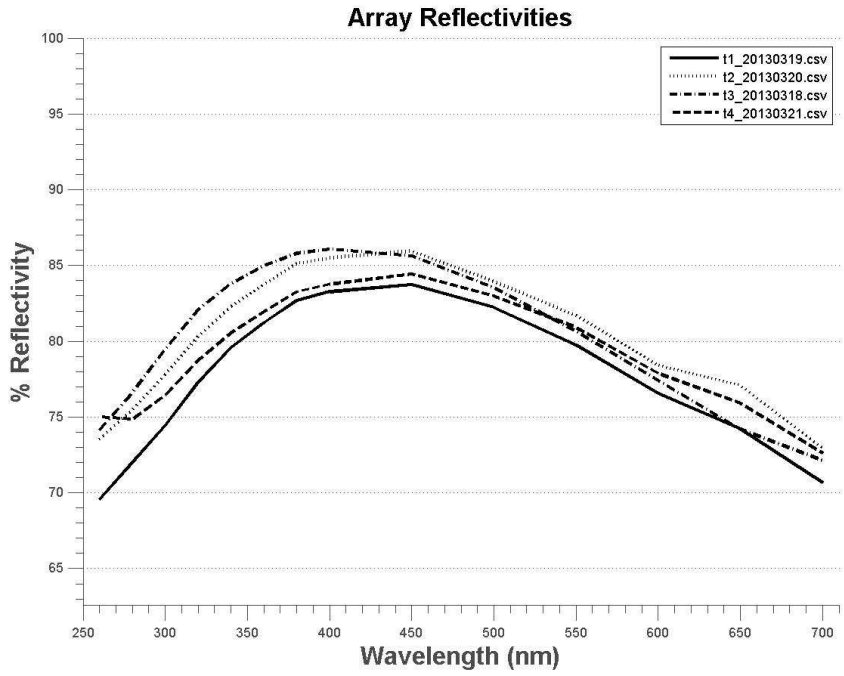

Figure 2.11: Telescope reflectivity as of March 2013, calculated based on measurement of 12 sample facets taken from different parts of each telescope (see the text for details). Given the results, mirrors in the bottom part of Telescope 2 were swapped. Figure credit: E. Roache, VERITAS Collaboration.

Following the monthly PSF measurements, mirrors are re-aligned if needed (usually twice a year). Mirror misalignment mostly originates from the replacement of mirror facets. To measure the misalignment of the facets, a method called "raster scan" is used. The raster scan method consists of directing the reflector dish to a bright star and taking pictures of the reflector while it directly points at the star as well as scanning a grid of points around it. The mirror facets that are correctly aligned will appear brightest when pointing at the star, while the misaligned ones will brighten when pointing outside of the star. The misalignment angle of a given facet is inferred from the pointing direction of the whole dish with respect to the star when that particular facet becomes brightest [McCann and others, 2010]. This is a new alignment technique that was introduced in spring 2009 and it provided an improvement of $\sim 30\%$ in the optical PSF.

2.4 Analysis of VERITAS Data

In addition to the real-time data analysis software Quicklook that was mentioned above, VERITAS has two independent standard offline analysis packages: Eventdisplay and VEGAS (VEritas Gamma-ray Analysis Suite). The VERITAS data analysis results given in Chapter 4 are from the VEGAS analysis and have been cross-checked with an Eventdisplay analysis carried out independently. It is standard procedure in VERITAS to use both analysis packages and cross-check the results for a publication. In this section, the analysis steps of VEGAS are described. VERITAS raw data is used as input at the first and second stages of VEGAS. The output files generated at each stage are in ROOT[1] format.

2.4.1 Calibration Calculation and Image Cleaning

The first thing to do in the data analysis chain is to eliminate biases that originate from hardware dependencies. As mentioned earlier, for each channel, the pedestal and its RMS spread (so-called "pedvar") are calculated from the pedestal events that have been recorded in a data run (2.3.3). Based on pedvar values, image cleaning is performed on each air shower event.

To construct an air shower image free of bias and distortions, it is essential to re-adjust the signals collected by individual pixels according to the differences in PMT gain and timing. The PMT signal that results as a response to a single photo-electron is called the absolute gain of that PMT, and varies across the camera due to PMT ageing. The quantity that is important to know for calibration is the relative gain, calculated as follows. First, for each pixel i, the arithmetic average for gain is calculated (g_i), by summing over all flasher events. Then the average gain for the entire camera $g_{\rm av}$ is found, by summing over all the pixels. The relative gain for the pixel i is then given by the ratio $g_i/g_{\rm av}$. Once the relative gains are determined for the whole array, for every event in the data file, the signal in each pixel is divided by its respective relative gain. The relative gain distribution across a camera peaks at 1 and has an RMS of ~ 0.02, right after the HV is flatfielded (see Figure 2.12). Similarly, each PMT signal has a slightly different arrival time,

[1] http://root.cern.ch

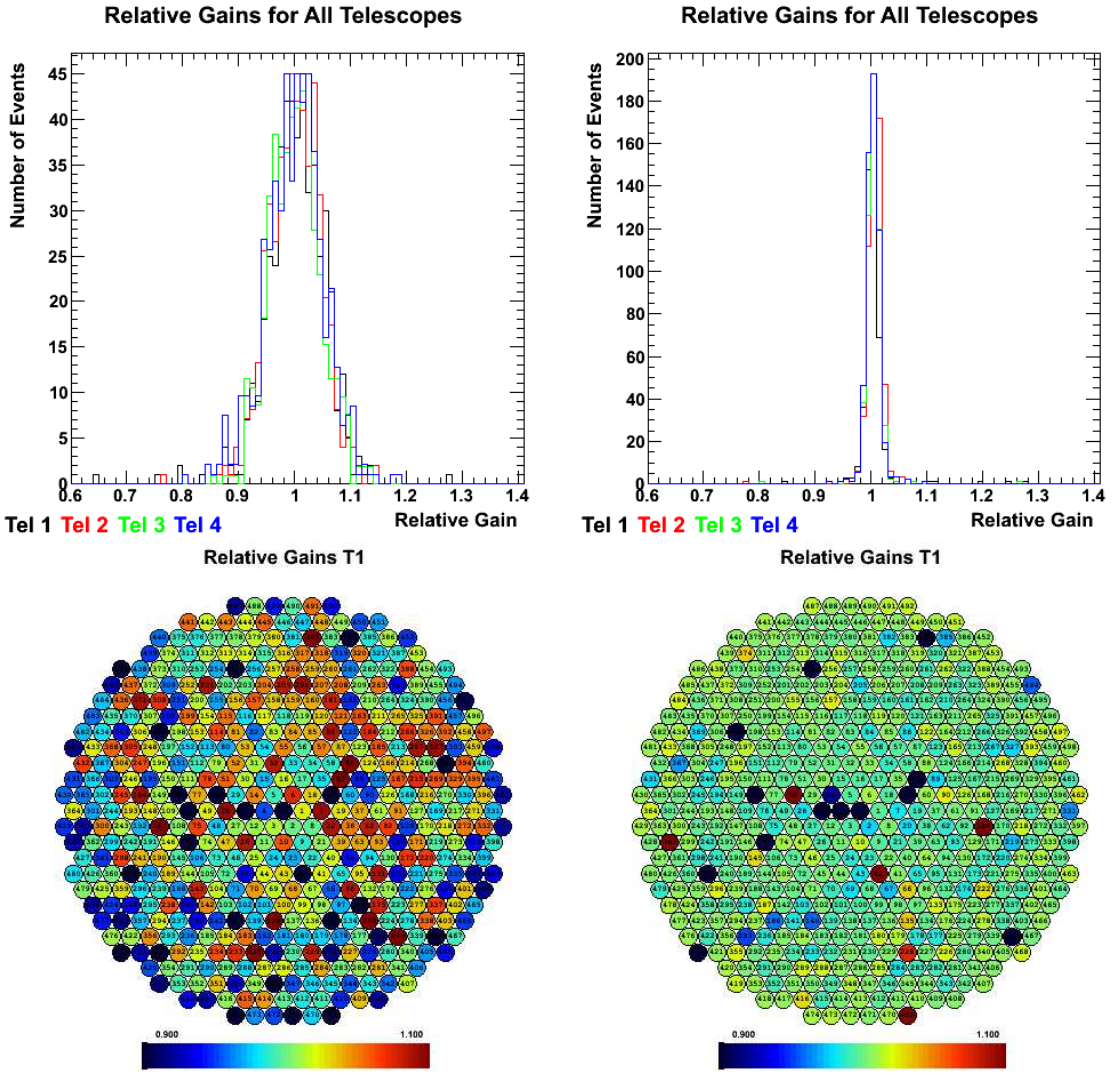

Figure 2.12: Top panel: Relative gain distributions of all telescopes before (left) and after (right) flatfielding. One can see that the RMS of the distribution drops from ~ 0.08 to ~ 0.02. Due to PMT ageing, the RMS increases with time. Flatfielding is usually done whenever the RMS reaches a value of ~ 0.04, or the gains drop by more than $\sim 2\%$. This occurs roughly every two to three months. Bottom panel: T1 camera distributions of relative gains for the same flasher runs. The color bar represents the relative gain.

due to the length difference in cables. Relative time differences are calculated for each pixel with respect to the camera average, and used for adjusting the arrival times.

Once the gain and timing calibrations have been applied, the data is ready to be cleaned from NSB fluctuations. For this purpose, the signal to noise ratio of each pixel is calculated the following way:

$$\sigma = (signal - pedestal)/pedvar \tag{2.1}$$

Pixels with $\sigma \geq 5$ are called "image pixels", they contain a significant signal that cannot be simply due to NSB fluctuations, and therefore is due to Cherenkov light. Image pixels contain most of the light that reaches the detector from the EAS, however, their neighboring pixels could contain Cherenkov light information as well, even if the signal they contain is not as strong. Capturing any possible neighboring pixel that contributes to the shower image is particularly important, because without them the shower image will tend to be slimmer in shape than it actually is, thereby introducing bias to the analysis at the gamma/hadron separation step (2.4.4). Therefore, once the image pixels are identified, the "boundary pixels" are determined, that is to say, those that neighbor at least one image pixel and have $\sigma \geq 2.5$. All the remaining pixels in a given event are excluded from the remainder of the analysis. This procedure is called image cleaning.

2.4.2 Image Parameterization

Air showers have elliptic images on the camera plane, as illustrated in Figure 2.13. The shape, signal content, and the orientation of the shower image contain essential information about the EAS, such as its direction in the sky, where it would land on the ground, energy of the primary particle, and whether it is gamma-initiated or not. The image centroid and major axis are found with a first-moment fit on the light distribution. Second moment fits in lateral and longitudinal directions with respect to the main axis yield the *width* and *length* of the shower image. Using the first and second moments, additional parameters such as *distance*, *disp* and *alpha* are calculated as described below. The third moment of the light distribution determines the *asymmetry* of the shower image. Image parameterization was first introduced by [Hillas, 1985] and then developed to

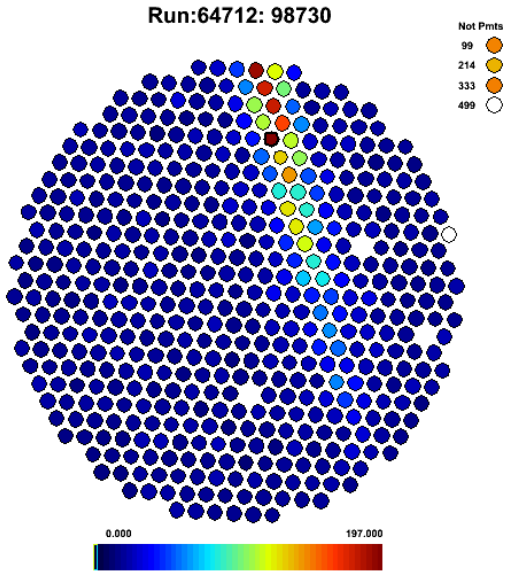

Figure 2.13: A cosmic ray shower image on the camera plane.

include more parameters for characterizing the shower image. Most commonly used and relevant Hillas parameters are as follows (also see Figure 2.14):

- **length:** RMS of the light distribution along the major axis.
- **width:** RMS of the light distribution perpendicular to the major axis.
- **size:** Total signal content of the contributing pixels, given in dc units.
- **distance:** Angular distance from the image centroid to the center of the field of view, on the camera plane.
- **alpha:** Angle between the major axis and the line along the *distance* parameter. This parameter represents a measure of the image orientation with respect to the camera center.
- **disp:** Angular distance from the image centroid to the projection of the putative source location on the image major axis.
- **asymmetry:** Skewness of the image along the major axis, either 1 or -1, depending on which side of the image has more light concentration.

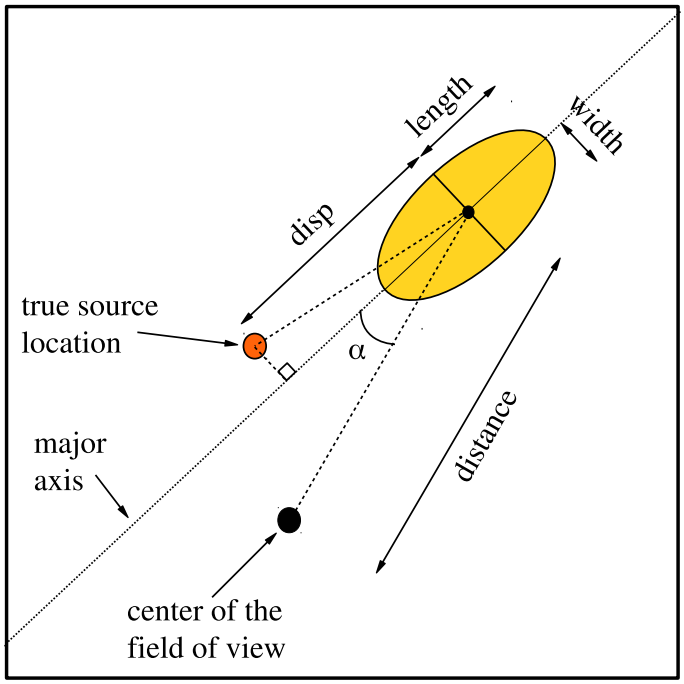

Figure 2.14: Diagram showing Hillas parameterization of a shower image on the camera plane.

After the shower images are parameterized, before proceeding to the reconstruction step, a set of "quality cuts" are applied to the data in order to discard the images that do not contain enough signal, or that are truncated due to being too close to the camera edge. The quality cuts include cuts on *NTubes* (number of the pixels present in the image), *size*, and *distance*. The purpose of the *distance* cut is to eliminate truncated images, since the biases introduced by truncation will affect the reliability of image parameterization and result in mischaracterization of the air shower. The quality cuts that were used in the analysis presented in Chapter 4 are as follows:

$size > 400$

$NTubes \geq 5$

$distance < 1.43$

2.4.3 Shower Reconstruction

Now that the images have been calibrated, cleaned, and have possibly survived the quality cuts, they are ready for stereo reconstruction of the air shower. The quantities that are determined at this step are direction, core location, and energy. Direction and impact distance are properties that are calculated based on the image geometry on the camera plane, whereas energy reconstruction is done by using lookup tables generated from Monte Carlo simulations. For an event to be reconstructed, images from at least two telescopes should be available.

Direction reconstruction consists of determining the direction of the primary gamma ray from image information. Once all the available images for a given shower image are superposed, the point with minimum total distance from each major axis gives the direction. In this calculation, the distances from each major axis are weighted by the *size* of their respective shower image. Figure 2.15 gives a schematic representation of stereo direction reconstruction. This direction reconstruction algorithm makes it possible to constrain the source location within an angular resolution smaller than 0.1° for regular observations. However, in the case of LZA observations, it dramatically loses its power. For this reason, another direction reconstruction method that employs the *disp* parameter is used for observations that are taken at LZA. The *disp* method was implemented in VEGAS by the author and details about the implementation along with performance test results are given in Appendix A.

Core location the position on the ground where the air shower would have landed. To reconstruct the core location, the major axes of shower images are extended out of the mirror planes of the telescopes and their intersection is found (see Figure 2.16). The distance between the core location and a telescope is the respective impact distance. This quantity is essential in finding the energy of the primary particle, since the size of the image, that is directly related to the energy, is affected by the impact distance. An air shower event whose trajectory extends to a location far from a given telescope (i.e. large impact distance) would appear fainter than another one with the same primary energy, but smaller impact distance.

After determining the direction and the impact distance, another important property to be calculated is the energy of the primary particle, since one is interested in constructing the spectrum of

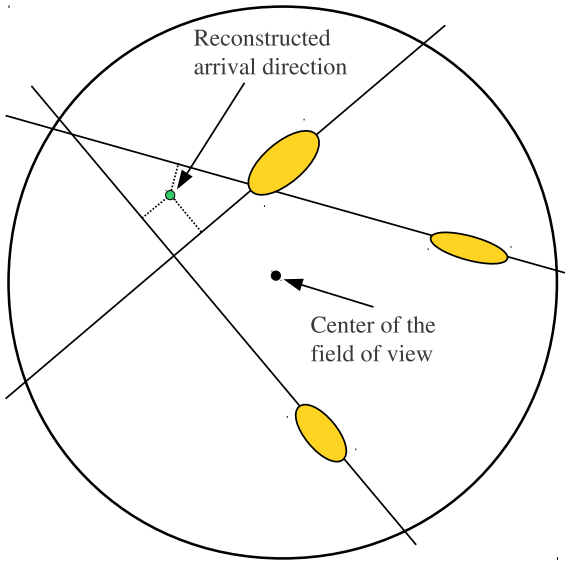

Figure 2.15: Schematic showing the reconstructed direction of a shower image on the camera plane. The point that minimizes the total distance from each major axis gives the direction. The distances form each major axis are weighted by the *size* of their respective shower image. The image is not to scale.

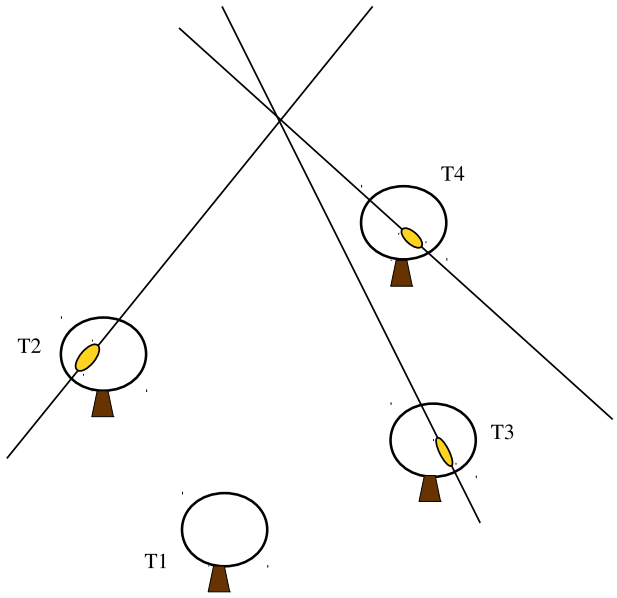

Figure 2.16: Core location reconstruction of an air shower on the ground. Major axes from each shower image are extended along the telescope mirror planes and their intersection is found. The distance between the core location and a telescope is the respective impact distance.

the gamma-ray sources to be able to address many scientific questions. The primary energy associated with an air shower event is inferred from multi-dimensional lookup tables that are prepared using Monte Carlo simulations [Maier and others, 2007]. The dimensions for energy lookup tables include zenith, azimuth, pedvar, *size*, telescope ID, impact distance, and absolute offset. Absolute offset refers to the angular distance between the reconstructed direction and the center of the field of view on the camera plane.

2.4.4 Background Rejection and Signal Extraction

Once the air shower events have been reconstructed, the final step in the analysis is to figure out whether or not there is a gamma-ray signal originating from the position of interest. For this purpose, exclusion of known gamma-ray sources from the field of view, identification of CR-initiated events, accurate modeling of the camera acceptance and rejection of CR background are necessary.

2.4.4.1 Gamma-Hadron Separation

It is important to note that from the analysis point of view, there are two types of events: gamma-like and CR-like. CR-like events are all CR-initiated air showers. On the other hand, gamma-like events can be either real gamma-initiated air showers or CR-initiated ones that look like they are gamma-initiated. One useful fact to address this degeneracy is that CR-initiated EAS are isotropically distributed in the sky, and consequently any significant excess of gamma-like events from a particular direction would indicate a source of gamma rays. Therefore, the background rejection is carried out in two steps: first, "selection cuts" are applied to the data. This is referred to as "gamma-hadron separation" and it eliminates more than 95% of the CR-initiated events, but cannot distinguish the gamma-like CR events from real gamma events. Second, the source region is compared with background regions that are free of known gamma-ray sources, to see if there is a significant excess in the source region. This second and final step is referred to as "signal extraction"(2.4.4.3). Note that the first step is indispensable since, as mentioned in Chapter 1, CR air showers are about 100 to 1000 times more abundant than gamma air showers in the energy band of interest, so a simple search for excess would not be of any use without the gamma-hadron separation step.

Selection cuts are based on two essential features of CR-initiated air showers. The first feature is that their distribution in the sky is isotropic. Since the isotropic background of real gamma rays is practically zero, one does not expect to detect any gamma rays outside the target position or known gamma-ray sources within the 3.5° field of view. Therefore, an angular cut around the target location is applied to the data, and the signal is searched for only within the cut region. This is called the θ^2 cut, where θ is the angular distance between the putative source position and the reconstructed direction. The θ^2 cut depends on the angular resolution of the instrument: as the angular resolution improves with hardware and software upgrades, the expected source location becomes better constrained and the θ^2 cut shrinks. Figure 2.17 shows the θ^2 square plot of the galactic center (Sagittarius A*) data(see Appendix A). In this analysis, an a priori optimized θ^2 cut of 0.02 was applied to the data set.

The second feature of the CR-initiated air showers that is useful for selection cuts is the fact that

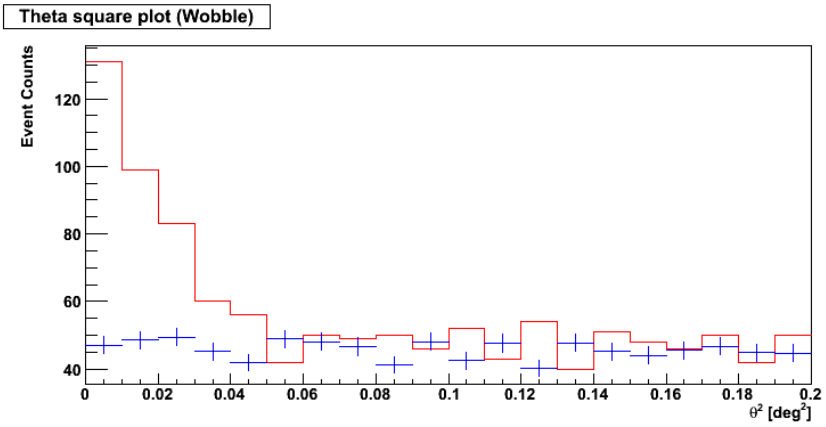

Figure 2.17: θ^2 distribution for the galactic center (Sagittarius A*) analysis presented in Appendix A. An a priori optimized θ^2 cut of 0.02 deg^2 was applied to the data set.

hadronic interactions involve more particles with transverse momenta, resulting in a larger lateral development of the particle cascade compared to a gamma-initiated air shower (see Chapter 1). This fact is manifested in the shape of the shower image on the camera plane. By applying specific cuts on the *width* and *length* parameters, it is possible to successfully identify a significant amount of CR air showers. The actual quantities that are used in the gamma-hadron discrimination algorithm are not *width* and *length*, but *mean scaled width (MSW)* and *mean scaled length (MSL)*. *MSW* is defined as follows:

$$MSW = \frac{1}{N_{tel}} \sum_{i=1}^{i=N_{tel}} \frac{w_i}{w_{av}}, \tag{2.2}$$

where w_i is the *witdh* parameter for the telescope i, and w_{av} is the mean of the *width* parameter for simulated events of a given *size*, at a given impact distance, and zenith angle. The same formula where *width* is replaced by *length* gives the *MSL* parameter. In Eventdisplay, slightly different parameters are used for gamma-hadron separation, called *reduced mean scaled width/length (MSCW, MSCL)* and calculated as follows:

$$MSCW = \frac{1}{N_{tel}} \sum_{i=1}^{i=N_{tel}} \frac{w_i - w_{med}}{\sigma_{90}}, \tag{2.3}$$

where w_{med} is the median value and σ_{90} is the width of the *width* distribution for 90% of the events [Daniel and others, 2007]. Figure 2.18 shows the distribution of the *MSCW* parameter.

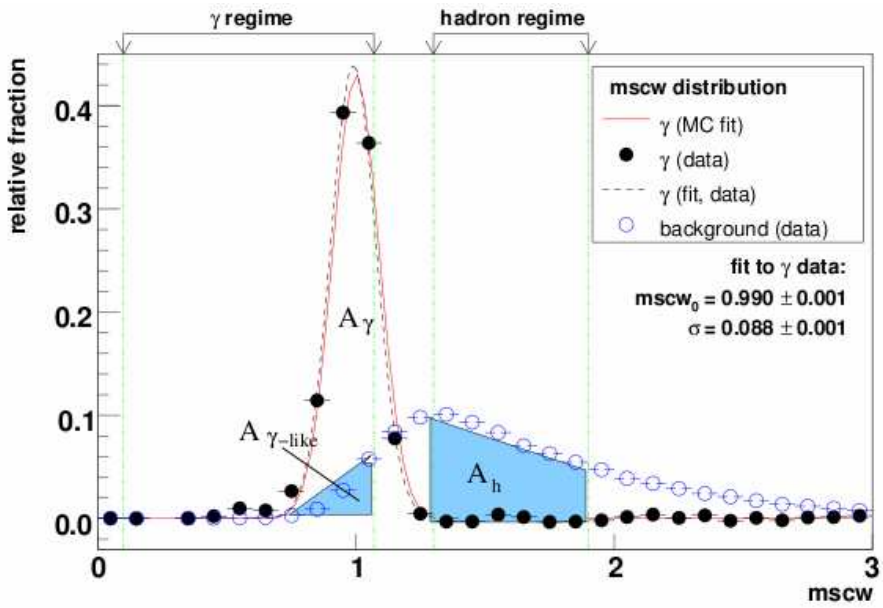

Figure 2.18: Normalized *MSW* distribution of gamma and CR events. Gamma and CR (hadron) regimes are clearly separated, and a significant fraction of the CR events ($A_{\rm h}$) can be identified and excluded through cuts applied on the relevant parameters such as, e.g., *MSW*. However there is a non-negligible overlap where gamma-like CR events ($A_{\gamma-{\rm like}}$) contaminate the real gamma events (A_{γ}). These are taken into account in the next step of the analysis (2.4.4.3). Figure from [Beilicke, 2008].

Gamma and hadron regimes are clearly distinct; however there is a non-negligible hadron contamination in the gamma regime. These are the gamma-like CR events that are to be estimated and subtracted in the next step of the analysis, as decribed in Section 2.4.4.3.

2.4.4.2 Camera Acceptance

In order to achieve an accurate background rejection, it is essential to characterize the camera acceptance for gamma-like CR events (see 2.4.4.1). Acceptance is defined as number of detected events per solid angle. Now although it is true that CR events are isotropically distributed, as a result of the cuts that are applied in the analysis, and the fact that the camera is a detector of limited size with non-negligible border effects, the acceptance turns out to have a dramatic dependence on the radius. Figure 2.19 shows how the acceptance drops with increasing distance from the camera center.

When there are known gamma-ray sources in the field of view, it is important to prevent the

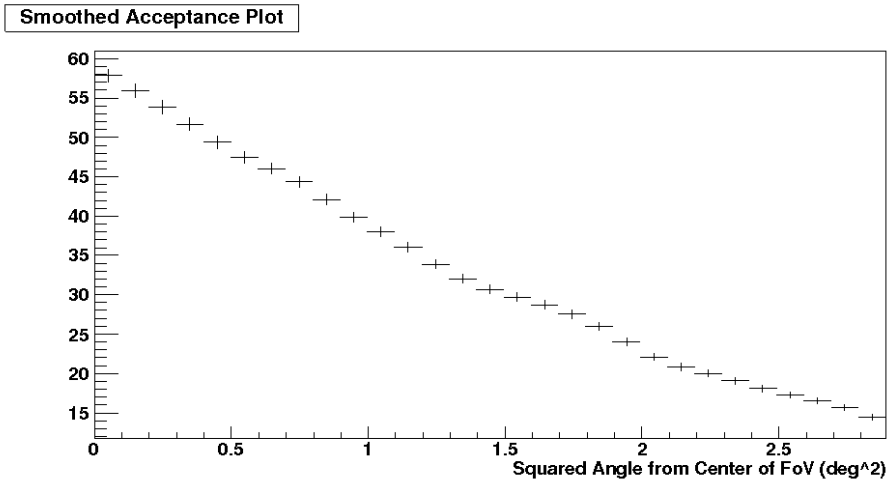

Figure 2.19: Acceptance plot for the data analysis on the blazar RBS 0413 presented in Chapter 4. The acceptance is inversely related to the distance from the camera center.

bias that would be introduced in the acceptance calculation from those regions. This is done by first exluding the source region, then making a partial correction using an exposure map based on the exclusion time. Finally, to fill in the regions where the acceptance map is completely blank, an interpolation is carried out. The acceptance modeling is done using real data only, and the calculation is performed on the data set that is to be analyzed. If there are too many strong gamma-ray sources in the field of view that would complicate the acceptance calculation, another data set can be used as long as the observations are made under similar conditions and the same set of cuts are applied to the data.

2.4.4.3 Signal Extraction

Now that a significant amount of CR-initiated air showers have been excluded by applying selection cuts, it is time to estimate and subtract the amount of gamma-like CR events that are still present in the data, isotropically distributed in the field of view. This is achieved by identifying OFF regions in the data, where no known gamma-ray sources exist, and using these regions to estimate the background from gamma-like CR events. VEGAS uses two separate methods for this step: reflected regions (or wobble) method and Ring Background Method (RBM).

Reflected Regions Method

As mentioned in Section 2.3.1, VERITAS data is taken in wobble mode, where the pointing of the telescopes are 0.5° offset from the target coordinates. The reason for this is to be able to take simultaneous OFF region data, that have the same shape and size as the signal (or ON) region and located at the same distance to the camera center. This is shown schematically in Figure 2.20 where the orange circles in are the OFF regions that would be used for the source region represented by the yellow circle. The practicality of this method is that all of the ON and OFF regions are at the same distance to the camera center, so their acceptance is the same, assuming that the camera is azimuthally symmetric. Therefore one does not need to correct for camera acceptance in the analysis. The number of excess counts $N_{\rm ex}$ is calculated as follows:

$$N_{\rm ex} = N_{\rm ON} - \alpha\ N_{\rm OFF}, \tag{2.4}$$

where N_{ON} and N_{OFF} correspond to the total number of events in ON and OFF regions respectively, and the normalization coefficient α equals $1/n$, n being the number of background regions, which is equal to five in the example shown in Figure 2.20. The reflected regions background model is used for signal search, light curve, and energy spectrum calculations.

Ring Background Method (RBM)

In this method, the OFF region is a ring shaped area surrounding the signal region (see the black area in Figure 2.20). In this case the α parameter in Equation 2.5 also includes the respective acceptances of the ON and OFF regions, since they are different:

$$\alpha = \frac{A_{\rm ON}}{A_{\rm OFF}} \times \frac{Acc_{\rm ON}}{Acc_{\rm OFF}}, \tag{2.5}$$

where $A_{\rm ON}$ and $A_{\rm OFF}$ are the areas, and $Acc_{\rm ON}$ and $Acc_{\rm OFF}$ are the average camera acceptances of gamma-like CR events for the ON and OFF regions, respectively. RBM is used for signal search and making skymaps, since it can be applied to any point in the field of view. Due to the energy dependency of the camera appectance, it is not a practical method for spectral analysis. Figure 2.21 left shows an RBM excess counts map of the galactic center data analysis presented in Appendix A.

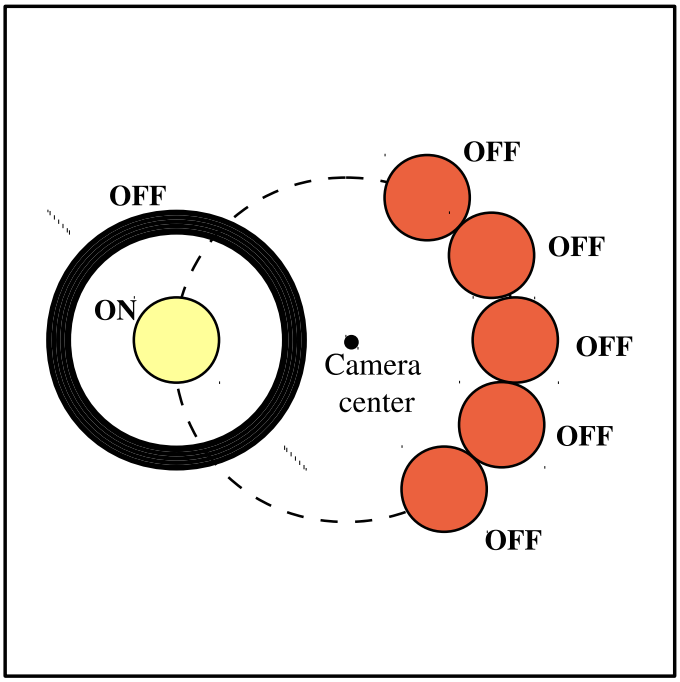

Figure 2.20: ON and OFF regions used in background rejection after the selection cuts have been aplied to the data. The yellow circle on the left is the signal (ON) region. The orange regions aligned along the dashed line are the reflected background OFF regions. They are located at the same distance from the camera center as the ON region, and therefore have the same acceptance. The black ring around the signal region is the ring background OFF region, with a different acceptance than the ON region, that should be taken into account in the excess counts calculation.

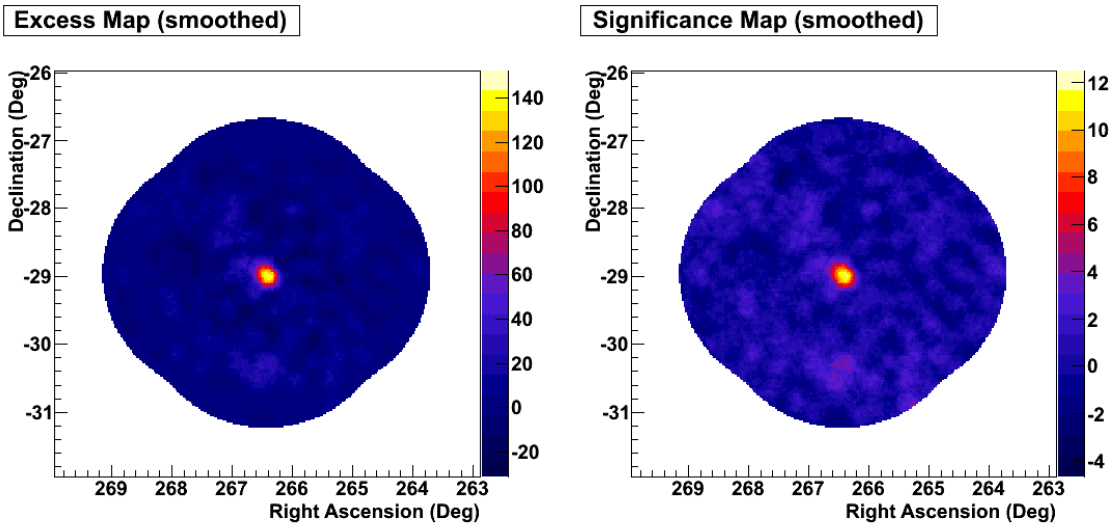

Figure 2.21: Skymaps for the galactic center analysis presented in Appendix A. Left: an excess counts map where the number of excess counts at every position in the field of view is calculated with the RBM technique. Right: a significance map where the significance at every point in the field of view is calculated using Equation 2.6.

Significance Calculation

Now that the number of counts in the ON and OFF regions have been calculated, the significance S of the excess counts can be determined by using the equation (17) from [Li and Ma, 1983], given below. This formula gives the statistical significance of the excess, in terms of standard deviations σ. In VERITAS, a detection is claimed if the significance is greater than or equal to $5\,\sigma$.

$$S = 2^{1/2}\left\{N_{\mathrm{ON}}\ ln\left[\frac{1+\alpha}{\alpha}\left(\frac{N_{\mathrm{ON}}}{N_{\mathrm{ON}}+N_{\mathrm{OFF}}}\right)\right] + N_{\mathrm{OFF}}\ ln\left[(1+\alpha)\left(\frac{N_{\mathrm{OFF}}}{N_{\mathrm{ON}}+N_{\mathrm{OFF}}}\right)\right]\right\}^{1/2} \tag{2.6}$$

The data analysis methods described above were used for the analysis of the blazar RBS 0413 discovered by VERITAS in VHE gamma rays. Chapter 4 presents the analysis results for RBS 0413. We start by first introducing active galactic nuclei and blazars in Chapter 3.

Part II

Blazars

Chapter 3

Active Galactic Nuclei and Blazars

Active Galactic Nucleus (AGN) is a term that designates a galaxy core which is unusually bright, to the extent that by order of magnitude, its luminosity equals or exceeds the radiation emitted by its host galaxy, which in turn is referred to as an "active galaxy". In addition to their thermal emission, Active Galactic Nuclei (AGNs) radiate non-thermal continuum extending from radio band to X-rays or gamma rays that suggests underlying emission mechanisms where relativistic particles are involved. Strong emission lines represent another typical feature of AGN spectra. The currently accepted paradigm that explains the origin of the AGN power is the flow of matter into a centrally located supermassive black hole through an accretion disk. Historically, AGNs were discovered with instruments operating in different bands and sensitivity ranges. As a result, selection effects played a big role in early classification schemes and nomenclature, that can be confusing at times. With increased understanding and unification schemes that developed over time, it turned out that a convenient way of studying these objects was to separate them according to their radio to optical flux ratio, that demarcated two main sub-groups: radio-quiet and radio-loud AGNs. These two groups are usually separated based on their specific flux at a given radio frequency or on the ratio of their radio specific flux to the optical one (see, e.g., [Kellermann and others, 1989]). Radio-quiet AGNs constitute $\sim$ 90% of the whole population [Wilson and Colbert, 1995]. On the other hand, radio-loud AGNs exhibit the most extreme properties and are characterized by the presence of strongly beamed plasma jets. They constitute the parent population of blazars, the main

focus of this work, and have been subject to comprehensive studies since their discovery, leading to classification and unification schemes based on multiwavelength observations and polarization measurements [Urry and Padovani, 1995].

3.1 Active Galaxies

Active galaxies exhibit features that are indicative of "activity" within them. Observations indicate that the unusually high luminosity emitted from the center of an active galaxy is generated within a very compact volume. Active galaxies are found over a large range of redshifts (z), from the nearby Seyfert galaxies ($z \sim 0.03$), where the host galaxy is resolved, to the distant quasars ($z > 6$) that appear as point sources. Due to their large redshift distribution, AGNs are important probes in cosmological studies.

3.1.1 AGN Continuum and Variability

Perhaps the most remarkable property of active galaxies is their extremely high energy output. Typically, the luminosity of an active galaxy is in the range of $\sim 10^{44} - 10^{46}$ergs s^{-1}. This is comparable to the host galaxy emission in low luminosity AGNs, and 100 times as luminous as the host in high luminosity ones.

The AGN continuum spans the electromagnetic band from radio waves to X- or γ rays. The broad-band spectral energy distribution (SED) of AGNs cannot be modeled by single- or multi-temperature blackbody radiation. To first order, power-law functions of the form

$$F_\nu = C\nu^{-\alpha}, \tag{3.1}$$

requiring non-thermally distributed emitting particles, provide plausible fits to the observed SEDs. In the above formula F_ν, the specific flux at the frequency ν, is a negative power of the frequency, with the power-law index α. However, a simple power-law description remains insufficient to describe many complex features that are observed over the whole broad band. In addition, the spectral index α varies from one emission band to another in a given SED. Thus it is reasonable to

consider that the AGN continuum comprises both thermal and non-thermal radiation, originating from different regions within the compact emission region.

In the radio band, AGNs that are relatively nearby (and thus can be resolved) show a central compact source accompanied by an extended component, with a size varying from kiloparsecs up to megaparsecs. The extended emission is manifested as pairs of lobes and jets, more or less symmetrically located around the central compact radio source. The radio part of the SED is well described by a power law that can be generated by synchrotron emission from electrons with initial energy distribution of the form of a power law. The radio band provides the smallest contribution to the bolometric luminosity in all AGNs, and its non-thermal origin is well-established. On the other hand, the infrared (IR) emission is mostly thought to be of thermal nature, and models involving radiative transfer in a dusty torus surrounding the AGN are commonly invoked. The IR band constitutes the portion of the AGN SED that is most substantially contaminated by the host galaxy: separating the intrinsic AGN emission from the host galaxy contribution is important in IR AGN studies [Mullaney and others, 2011]. In the optical/ultraviolet (UV) band, a typical AGN SED feature is a strong broad emission referred to as the 'big blue bump'. Thermal emission of temperature $\sim 10^{5\pm1}$ K [Peterson, 1997] from a thin accretion disk surrounding the central black hole is thought to make a significant contribution to the big blue bump, plausibly supplemented by a power-law continuum in the infrared (IR) to X-ray region (eq. 3.1), with a spectral index of ~ 1 [Peterson, 1997]. AGNs are very luminous in X-rays and more than a thousand radio-loud AGNs have been detected in gamma rays above 100 MeV. Figure 3.1 shows the SED of the well-studied radio-loud quasar 3C 273 taken from [Soldi and others, 2008]. The non-thermal continuum extends from radio waves to GeV gamma rays. The low-energy component of the SED covers the radio to UV part, with a falling tail reaching to soft X-rays, whereas the high-energy one covers the X-ray to gamma-ray region. The big blue bump can be seen in the optical/UV band ($\sim 10^{15}$ Hz). The data plotted on this SED is averaged over 4 to 44 years depending on the observation band, and the grey area represents the observed range of variations.

AGNs exhibit irregular variability in all wavelengths: no periodicity is detected. Variability studies are important in understanding and constraining morphologic and radiative properties of

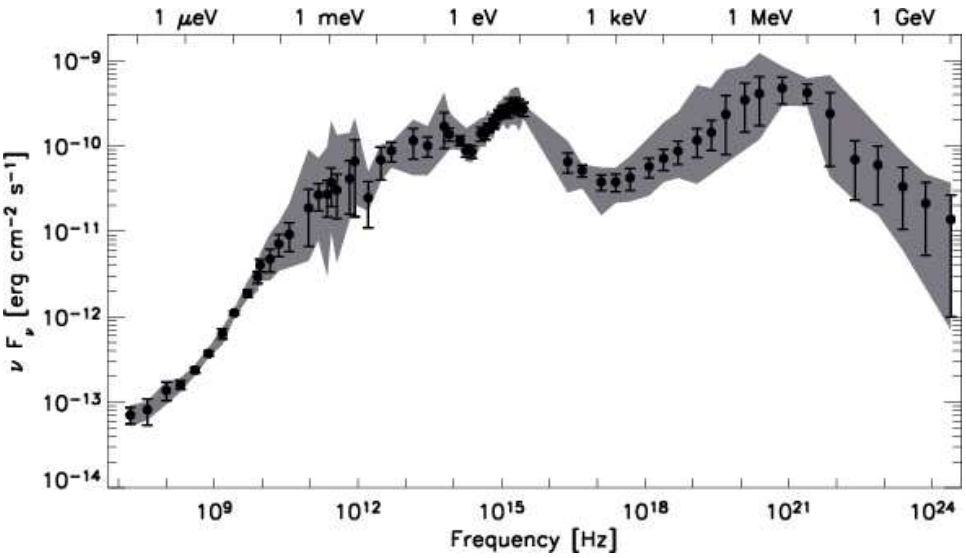

Figure 3.1: Average broad band (from radio waves to HE gamma rays) SED of the radio-loud quasar 3C 273, averaged over 4 to 44 years depending on the wavelength ([Soldi and others, 2008]). The big blue bump in the optical/UV range, interpreted as a contribution from the accretion disk, is seen ($\sim 10^{15}$ Hz). The grey area represents the observed range of variations.

AGNs. The simplest case is to use the minimum variability time scale $\Delta t_{\rm min}$ in a given band to constrain the size r of the emitting region for that band. Light-travel time arguments yield an upper limit of the following form: $r \leq \Delta t_{\rm min} c$, where c is the speed of light. On the other hand, variability correlations are also important. Optical and UV variabilities have been observed to be simultaneous, with X-ray variability being highly contemporaneous, up to within a few days. As for the IR variability, it has been observed to exhibit delayed variability after UV/optical, which indicates that the IR emission could most likely be originating from the re-processing of the UV/optical by a dusty region [Peterson, 1997]. In addition, some optical activity enhancements have been observed to be succeeded by TeV gamma-ray flares, leading to the discovery of several blazars in the TeV gamma-ray band (see section 3.3.1). Another interesting observation is that the broad line emission (section 3.1.2) variability has been found to be following the continuum one with a delay, which is interpreted as the continuum emission being the driving force behind the observed broad emission lines.

3.1.2 Emission lines

An important prominent observation that suggests activity and that is a very common feature found in most AGNs is strong emission lines, that appear as sharp peaks in AGN optical spectra. Since AGNs are found up to large distances where redshifting of the radiation becomes significant, the line emissions in a typical AGN SED appear displaced towards lower frequencies, i.e. redshifted in comparison to their rest frame positions. Line emission is a result of atomic de-excitation in an ionized gas. It is well understood and the resulting spectral lines can be accurately identified. The missing part of the puzzle is what happens before: which process is responsible of ionizing the gas? It is thought that the continuum AGN radiation is the driving force behind the line emission, that is also supported by observations of highly correlated variability between the two phenomena [Peterson, 1997].

Another important feature that is observed in AGN emission lines is that they appear broadened. This phenomenon is known as Doppler broadening, and indicates that the source that emit the lines is rotating at high velocities (500 to 4000 km s^{-1} in this case), creating a difference in the relative velocity between different emitting points and the observer's line of sight. It follows that faster rotating regions will show broader emission lines and vice versa. The broadening is more enhanced for some lines and less so for others, hence as a simplest interpretation, one can conclude that there are at least two distinct emission regions: a broad line region, compact and central; surrounded by a narrow line region, larger in size and rotating with relatively smaller velocity. It should be noted that here the term "narrow" signifies only a relative narrowness, and the narrow emission lines, being about a few hundred km s^{-1} wide, are still significantly wider compared to typical stellar emission lines.

3.1.3 Active Galaxy Types

AGNs are typically classified according to their radio loudness and the absence or presence of broad emission lines in their optical spectra. In the following section we will see that this classification model will lead to a unification scheme. Some representative AGN types are described in the following paragraphs but it should be noted that this is not a complete AGN list.

Seyfert galaxies, with their remarkably bright nuclei and strong spectral emission lines, were the first AGNs to be detected. It turns out that now they constitute the low-luminosity tail of the whole AGN population. They are radio quiet and relatively nearby with a redshift distribution peaking around $z \sim 0.03$ [Tueller and others, 2010], so the host galaxy is resolved in optical images. The first observations of Seyfert galaxies brought up a classification based on the presence (type 1) or lack (type 2) of broad lines in their optical spectrum. Later on, this original classification was replaced with one based on the relative strengths of narrow and broad emission lines, where the "Seyfert type" is represented by a fractional number between 1 and 2. For instance, a type 1.5 has comparable broad and narrow lines, and a type 1.9 exhibits only an H_α broad line.

Radio galaxies are active galaxies radiating at a radio power of at least 10^{33} W, and having a compact or extended morphology. As the name suggests, they are radio-loud and, like Seyfert Galaxies, they may or may not exhibit broad emission lines in addition to their narrow emission lines, with subgroups Broad Line Radio Galaxies (BLRGs) and Narrow Line Radio Galaxies (NLRGs), respectively. Indeed, Seyferts can be considered radio-quiet versions of radio galaxies. Extended radio galaxies sometimes have symmetric non-thermal radio lobes, that may outshine the galaxy's radio luminosity. Most radio galaxies have one- or two-sided radio jets that are believed to transfer charged particles from the nucleus into the lobes, that could explain the non-thermal emission originating from the lobes as synchrotron radiation.

BL Lacertae Objects are radio-loud AGN with relativistically beamed jets outflowing along the accretion disk axis, and they exhibit little or no emission lines at all. The lack of spectral emission lines in BL Lacs poses problems in redshift measurements: about one third of these objects do not have a secure redshift measurement. BL Lacs exhibit strong, rapid and erratic flux variability in all wavelengths, and are often observed to have strong and variable polarization in the optical band. The line of sight in case of BL Lacs is very close to the jet axis with typical Doppler factors of ~ 20, which introduces anisotropy into the radiation and renders the luminosity boosted along the line of sight.

Quasars constitute another major class of objects that appear to have strong activity, with broad emission lines and can either be radio-quiet or -loud. They are found over a large range of redshifts

(from 0.06 to larger than 6 [Willott and others, 2010]), exhibit not only emission but absorption lines as well, and emit non-thermal continuum. Absorption lines are indicative of a continuum emission from the source and the presence of an absorbing medium, that could in principle be located anywhere between the emitting region and the observer. Being located at a large range of cosmological distances, quasars play an important role in probing the large-scale structure and history of the universe. Since they appear as point-like objects, they were originally unidentified and called radio-stars or quasi-stellar objects. While most quasars do not show significant polarization, there is a subclass that is observed to be relatively polarized. The spectra that belong to this subclass are flat in radio band and steep in optical (hence their name, flat spectrum radio quasars or FSRQs), with rapid and strong flux variability. With properties such as polarization and strong variability, FSRQs resemble BL Lac objects and together they constitute the type of AGN that is referred to as "blazar".

3.1.4 AGN Structure and Unification

Currently accepted AGN paradigm (see Figure 3.2) consists of a central super massive black hole of mass around $\sim 10^7 M_\odot$, corresponding to a Schwarzschild radius of $\sim 10^{13}$cm, surrounded by an accretion disk that extends up to $\sim 10^{15}$cm. Outside the accretion disk, a broad line region is located, of size $\sim 10^{16}$cm. The broad line region (BLR) is not resolved and its geometry is not well-known, however it is thought to be not homogenous but of clumpy structure. The estimated electron density for the BLR is $n_e \approx 10^{11}\text{cm}^{-3}$. The narrow line region (NLR) lies outside the BLR ($>\sim 10^{17}$cm), again of clumpy nature but much more massive and of lesser density ($n_e \approx 10^3\text{cm}^{-3}$). The typical NLR temperature is estimated to be around $\sim 10^4$K [Peterson, 1997]. The NLR is resolved in some AGNs and shows an axially symmetric (coincident with radio-lobe symmetry axis), wedge-shaped geometry, indicating anisotropic emission from the central regions of the AGN. Other evidence that indicates anisotropy through obscuration includes the indirect observation of broad lines in some Type 2 Seyferts in polarized light. To account for anisotropic emission, the AGN picture is complemented by the presence of an obscuring dusty torus surrounding the BLR, coaxially oriented with NLR wedges and coplanar with the accretion disk (see Figure 3.2).

Anisotropy caused by obscuration successfully explains the lack of broad emission lines in some AGNs through orientation arguments: If the symmetry axis makes a small angle with the observer's line of sight, the broad emission lines as well as narrow lines are visible. As the angle increases, the BLR emission will become gradually obscured and at large angles only narrow lines will be observable [Urry and Padovani, 1995]. This unification theory is also supported by the fact that some AGNs have been observed to transform from Type 1.5 to 2 over a time scale of a few years, which could be explained by a cloud moving over the BLR and obscuring the broad line emission. On the other hand, the question why AGNs show significant disparity in radio flux has not been answered yet. Radio-loud AGNs are also referred to as jet-dominated and the radio-quiet ones as disk-dominated. It has been suggested that the existence of a powerful jet that results in radio-loudness can be related to the host galaxy type or black hole spin [Urry and Padovani, 1995].

3.2 Blazars

BL Lacertae objects and FSRQs, with their jet axis oriented close to the observer's line of sight, constitute the 'blazar' subclass of radio-loud AGNs. This particular orientation allows relativistic beaming to give rise to distinctive observational features in blazars, such as anisotropic radiation, superluminal motion, high polarization and rapid variability that, from the light travel time arguments, may be indicative of a compact origin for the observed emission. In addition, AGNs detected in gamma rays are mostly blazars: 57% of GeV gamma-ray sources in the *Fermi* second catalog are blazars, while only 1% are non-blazar AGN [Nolan and others, 2012]. Based on observational facts, FSRQs are characterized by a BLR, depicted with strong lines in their optical spectra, that are not present in BL Lacs. Recent work studying FSRQ and BL Lac spectra in the framework of physical quantities such as high-energy (HE; $E > 100\,\mathrm{MeV}$) γ-ray spectral index and luminosity can be found in e.g., [Ghisellini and others, 2009]. Instrumental selection effects brought up two distinct classes for BL Lacs as radio-selected (RBL) and X-ray-selected (XBL) objects. This instrumental classification was later replaced with a more physical one based on radio to optical and optical to X-ray spectral indices, introducing the terminology of high- and low-frequency-*cutoff* BL

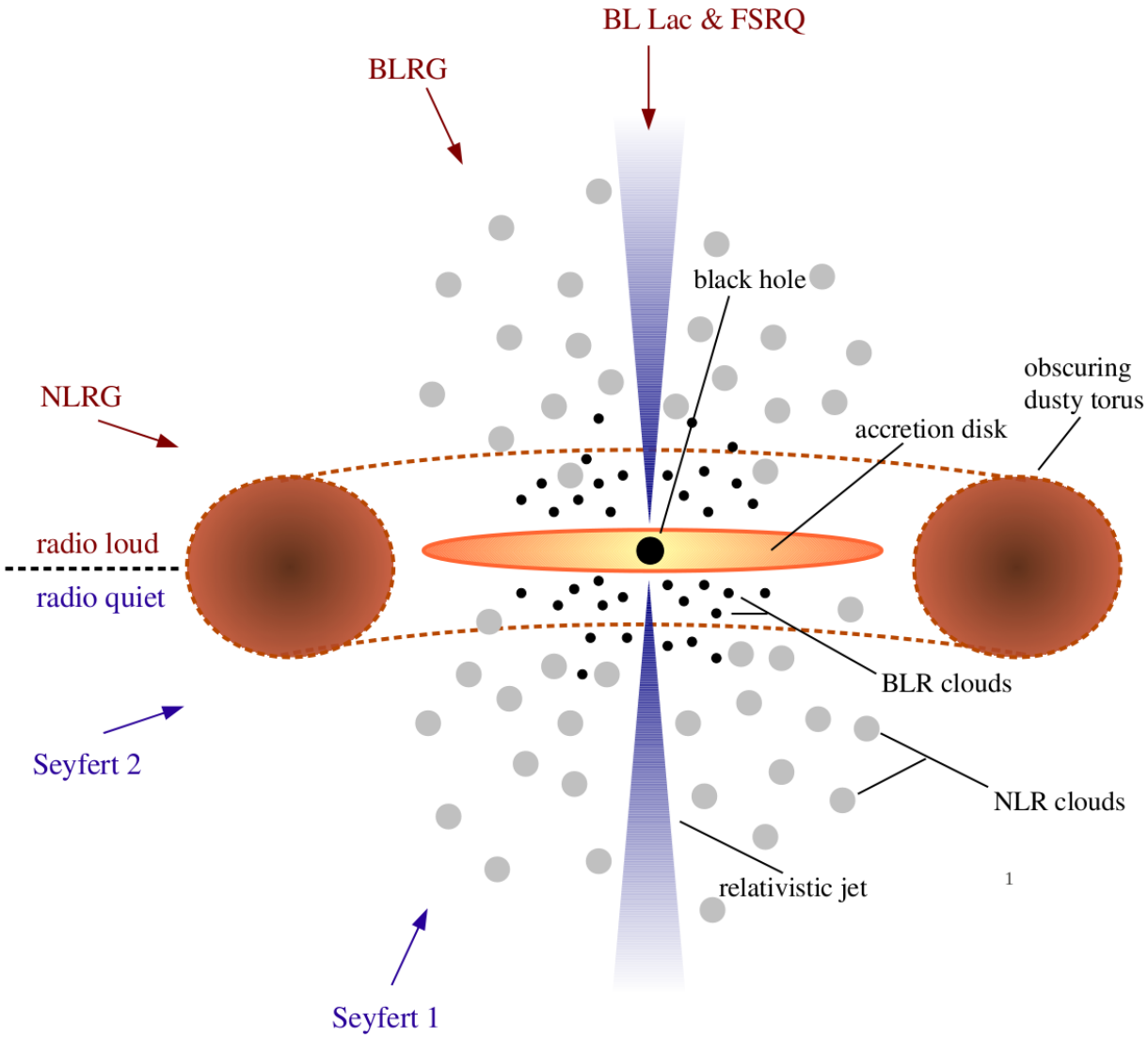

Figure 3.2: AGN scheme as described in Urry and Padovani 1995. BLR clouds (near the accretion disk) are eclipsed by the dusty torus for an observer looking from the side (Seyfert 2 and NLRGs), but they are visible to an observer looking within the cone opening angle of the NLR clouds (Seyfert 1, BLRGs, and quasars). BL Lac objects and FSRQs are seen within a small angle from the relativistic jet. Radio-loud AGNs (red) are shown above the dashed line and radio-quiet ones (blue) below. The relativistic jet is a feature of radio-loud AGNs only, but the obscuration of BLR emission by the dusty torus through orientation effects apply to radio-quiet AGNs as well.

Lac objects (HBLs and LBLs, respectively) [Padovani and Giommi, 1995]. Sometimes, the peak frequency of the synchrotron component of the SED is also used to define HBLs and LBLs as high- and low-frequency-*peaked* BL Lacs, respectively. Subsequent detection of objects with intermediate properties (intermediate-frequency-peaked BL Lacs or IBLs) between these two observationally distinct groups has made it more plausible that BL Lac objects constitute a continuum rather than a discrete sequence [Nieppola and others, 2008]. In the following subsections we summarize some observational properties (variability, superluminal motion, relativistic beaming and polarization) that are common to AGN in general, but more emphasized in blazars, since in that case we look deeper into the jet due to the small viewing angles.

3.2.1 Superluminal Motion

Evidence of relativistic beaming can be found in the observation of superluminal motion in some blazars, where a region of the relativistic jet appears to be moving with a speed faster than that of light (see Figure 3.3). Objects moving at relativistic speeds and very small angles with respect to the observer's line of sight can indeed appear to be moving faster than light in a tranverse direction. Figure 3.4 illustrates how superluminal motion can arise. Imagine that a relativistic point source with velocity β moves from point A to C during the time interval Δt, thus $AC = \beta\Delta t$. On the other hand, the observer sees the blob moving in the transverse direction along the path BC, so that $BC = \beta\Delta t sin\theta$. We assume that the paths taken after points B and C are of the same length. Then the time difference between the arrival of "photon A" and "photon B" to the observer can be simply expressed as

$$\Delta t' = AC/\beta - AB/1 = \beta\Delta t/\beta - \beta\Delta t\cos\theta/1 = \Delta t(1 - \beta\cos\theta) \tag{3.2}$$

where the speed of light is given as 1. Then the apparent transverse velocity $\beta'_{\perp}$ will be the following:

$$\beta'_{\perp} = BC/\delta t' = \beta\Delta t sin\theta/\Delta t(1 - \beta\cos\theta) = \beta\sin\theta/(1 - \beta\cos\theta) \tag{3.3}$$

It can be shown that for $\beta > 1/\sqrt{2}$, $\beta'_\perp$ can be larger than 1, depending on the angle θ. Note that eq. 3.3 can also be expressed as

$$\beta'_\perp = \beta_\perp/(1 - \beta\cos\theta) \tag{3.4}$$

where $1/(1 - \beta\cos\theta)$ is the non-relativistic Doppler factor.

3.2.2 Relativistic Beaming

Radiation emitted by a source moving at a relativistic speed will appear distorted to the observer; this phenomenon is known as beaming. Relativistic beaming is manifested in several observed quantities: arrival time, direction, and energy of the emitted photons. To see how this works, let's see what happens if we generalize the relativistically moving point source in the above section to an object with spatial dimensions. Consider Figure 3.4 with a rod moving along the path AC, with a length l. In a similar reasoning, it can be shown that the projected length $l'_\perp$ of the rod measured by the observer is

$$l'_\perp = l_\perp/\Gamma(1 - \beta\cos\theta) \tag{3.5}$$

where $\Gamma = 1/\sqrt{1 - \beta^2}$ is the bulk Lorentz factor, accounting for length contraction along the direction of motion. The term $1/\Gamma(1 - \beta\cos\theta)$ is the relativistic Doppler factor (δ), which is a key quantity for relativistic beaming. With similar geometric arguments and time dilation, the time interval between two photons measured in the observer frame will be related to the proper one as follows:

$$\Delta t' = \Delta t/\delta \tag{3.6}$$

This means that for small θ and relativistic β, the observer will measure the time interval shorter than the proper one, since δ will be larger than 1. Another salient outcome of relativistic motion is light aberration: Forward half of the emitted light will be bunched into a cone with opening angle $\sin^{-1}(1/\Gamma)$. It follows that relativistic beaming results in a time contraction and luminosity boosting in the observer's frame, which will be significantly manifested in flux and time variability measurements. In other words, the higher the Doppler factor is, the larger the apparent

luminosity will be measured compared to the intrinsic one and faster the apparent time variability. Consequently, large Doppler factors can account for excessive luminosity and rapid variability that are commonly observed in blazars. AGN Doppler factors typically vary in the range 0.1-40 [Hovatta and others, 2009].

The apparent transverse velocity $\beta'_{\perp}$ and the relativistic Doppler factor δ are two observable quantities that are related to the viewing angle θ and the bulk Lorentz factor Γ, that are in turn intrinsic properties. Accordingly, one can in principle measure $\beta'_{\perp}$ and δ, to infer θ and Γ. The Doppler factor can be measured in several methods: using radio variability, brightness temperature or synchrotron self-Compton (SSC) parameters [Veres and others, 2010]. AGN unification paradigms based on viewing angle have predictions on distributions of Γ and θ: blazars are expected to have smaller viewing angles compared to the rest of the AGNs, and BL Lac objects may differ from quasars in their distribution of Γ, as they are believed to belong to different parent populations
[Hovatta and others, 2009].

3.2.3 Spectral Properties and Radiation Mechanisms

The spectral energy distribution (SED) of blazar non-thermal continuum from radio to γ-ray energies exhibits a double-humped structure, when represented in an energy density (νF_ν) vs. frequency (ν) graph (see Figure 3.1 or 4.5). Figure 3.1 shows the broadband SED of the FSRQ 3C 273 in νF_ν representation, as of 2008. The low-energy hump peaks around infrared (IR) to ultraviolet (UV) band and the high-energy one around X-ray to γ-ray energies. The frequencies at which the peaks occur have been found to be correlated [Fossati and others, 1998]. The low-energy component is well-studied, with deep observations that accumulated good amount of data extending over several decades. The underlying radiation mechanism responsible for this part of the SED is now widely believed to be synchrotron emission from relativistic electrons in the blazar
[Kembhavi and Narlikar, 1999]. On the other hand, the high-energy radiation from blazars is not well-understood yet. Studies so far suggest that the non-thermal broadband emission originates from relativistic blobs in the outflowing plasma jets with high doppler factors (typically $\delta \sim 20$),

where the radiation is anisotropic and beamed along the jet axis, rendering the apparent luminosity much more enhanced compared to the intrinsic one [Dermer and Menon, 2009]. The jet power is believed to originate mainly from the accretion of the central black hole. According to the most plausible scenario, relativistic particle populations that have been created by diffusive shock acceleration in plasma jets, with energy spectra following power-law distributions, are injected into the jet blob. Several mechanisms could be responsible for the cooling of these particles; such as the synchrotron process, Compton scattering and proton-photon interactions. In the following paragraphs we summarize the most commonly invoked non-thermal radiation mechanisms that are though to take place in relativistic blazar jets.

Synchrotron Radiation

The low-energy peak of non-thermal blazar SEDs, spanning the electromagnetic spectrum from radio frequencies to optical, UV or X-rays, is generally accepted to be due to synchrotron radiation, which requires relativistically moving charged particles under a magnetic field. The particles, assumed to be in a uniform angular distribution in the co-moving frame of the emission region, will accelerate under the magnetic field and as a result emit synchrotron radiation. As to the nature of these charged particles, due to high energy losses, electrons are harder to accelerate compared to protons, but once accelerated, they radiate more efficiently, since the radiated power is inversely proportional to the square of the mass of the emitting particle [Böttcher and others, 2012]. Hence synchrotron radiation from relativistic electrons is currently accepted as the most plausible explanation for the low-energy component of the blazar SEDs, also referred to as the synchrotron component. On the other hand, it should be noted that the mechanism that accelerates these electrons to relativistic speeds with an energy distribution that follows a power law has not been fully understood yet, though it is commonly thought to be Fermi shock acceleration.

The radio range of the synchrotron component is marked by a down-turn towards lower frequencies. The reason is that photons may be absorbed by a non-thermal distribution of relativistic electrons in a magnetic field, with an absorption coefficent inversely proportional to the photon frequency. This results in the source being opaque to its own radiation under a critical frequency, that typically occurs at low radio frequencies. This phenomenon is known as synchrotron self-

absorption.

Leptonic Models

The high frequency bump of the blazar SED, that starts from the falling tail of the synchrotron component and reaches X-ray or γ-ray frequencies, is commonly called the inverse Compton (IC) component, for the following reason: the inverse Compton process is the simplest way to explain the non-thermal radiation emitted in this range. According to this scenario, the synchrotron photons that have originally been emitted by accelerated relativistic electrons are up-scattered to high energies by the same electrons[Maraschi and others, 1992]. This is called the synchrotron self-Compton (SSC) model.

In some cases where the blazar synchrotron peak is located at relatively low frequencies, an additional soft target photon field with the SSC model may improve the fit between models and high-energy data (see, e.g., [Acciari and others, 2009b]). This mechanism is referred to as external-Compton (EC). Thermal radiation from the accretion disk or a dust torus around the central compact region; or synchrotron emission from other regions of the relativistic jet are among possible sources of seed photons for the EC model [Böttcher, 2010].

Lepto-hadronic Models

Another approach that aims to explain the high-energy bump of the blazar SEDs is to consider proton-initiated radiation mechanisms and hadronic interactions. Again, it is commonly assumed that diffusive shock acceleration creates a non-thermal distribution of relativistic protons. Note that shock acceleration in this case is more efficient compared to the case of electrons, since electrons have a relatively shorter cooling time scale and consequently experience a larger energy loss while being accelerated. Shock acceleration is followed by $\mathrm{p}\,\gamma$ or $\mathrm{p}\,\mathrm{p}$ collisions that will lead to generation of a variety of meson populations [Mannheim and Biermann, 1989]. Pions (neutral as well as charged), having the smallest mass, will dominate the generated meson population and contribute to hard X-ray and γ-ray emission via production of high-energy photons (π^0 decay):

$$\pi^0 \;\rightarrow\; 2\,\gamma \tag{3.7}$$

and high energy leptons ($\pi^{\pm}$ decay) and subsequent electromagnetic cascades:

$$\begin{aligned} \pi^{\pm} &\rightarrow \mu^{\pm} + \bar{\nu}_{\mu} \\ \mu^{\pm} &\rightarrow \mathrm{e}^{\pm} + \overline{\nu}_{\mathrm{e}} + \nu_{\mu} \\ \mathrm{e}^{\pm} &\rightarrow \mathrm{e}^{\pm} + \gamma \end{aligned} \tag{3.8}$$

.

On the other hand, several studies have shown that pion decay may not be efficient enough to reproduce the TeV emission in some blazars, while the consideration of synchrotron radiation by (1) charged muons originating from pion decay and (2) primary protons, with resulting synchrotron-pair cascades can succesfully describe the observed TeV luminosity [Mücke and Protheroe, 2001]. This is also consistent with relatively high magnetic fields (∼tens of gauss) required to accelerate protons to the threshold energies needed for photomeson production. In order to have a self-consistent radiation picture it should also be accounted that electromagnetic cascades originating from various proton-initiated interactions might contribute to the low-energy hump of the SED [Böttcher, 2010].

3.2.4 Blazar Sequence

A unifying scheme combining both HBL and LBL objects as well as FSRQs was introduced by using bolometric luminosity as the main unification parameter [Fossati and others, 1998]. This unification scheme, commonly known as the "blazar sequence", is based on the following observational properties of the blazar SEDs: the luminosity of the low-energy hump (or the synchrotron component) L_{syn} is inversely correlated with the synchrotron peak frequency ν_{syn} and with the ratio of the high-energy hump luminosity to the low-energy hump luminosity, in other words $L_{\mathrm{IC}}/L_{\mathrm{syn}}$. Moreover, it is proposed that there exists a correlation between ν_{syn} and ν_{IC}. Originally the blazar sequence suggested three blazar types making up a continuous class: FSRQs, LBLs and HBLs, in order of increasing ν_{syn}. Figure 3.5 [Fossati and others, 1998] shows the luminosity - synchrotron peak relation from a blazar sequence perspective. An inverse relation between the synchrotron peak frequency and luminosities derived from polynomial fits to the SEDs is clearly seen. Subsequent detection of objects with intermediate properties between LBLs and HLBs introduced a new group

to complete the picture: intermediate-frequency-peaked BL Lacs (IBLs).

Study of objects that do not agree with this systematic classification have brought up the question whether the blazar sequence was influenced by selection effects [Antón and Browne, 2005]. In addition, more recent studies have set forth that when Doppler factors are taken into account and the observational quantities $L_{\rm syn}$ and $\nu_{\rm syn}$ are Doppler-corrected, they are found to be positively correlated, in opposition to what blazar sequence proposes [Nieppola and others, 2008]. Despite all the studies showing that the blazar sequence may not be based on intrinsic properties, but on selection effects and Doppler boosting, the LBL/IBL/HBL nomenclature is still commonly used to classify BL Lac objets according to their SEDs. Typically, blazars with $\nu_{\rm syn} < 10^{14}$ Hz are considered as LBLs, with 10^{14} Hz $< \nu_{\rm syn} < 10^{15}$ Hz as IBLs and with $\nu_{\rm syn} > 10^{15}$ Hz as HBLs.

3.3 TeV Blazars

To date, only a small fraction of known blazars have been detected in TeV energies. Despite the balanced distribution between FSRQs and BL Lac objects (as well as between LBLs and HBLs) in other energy bands, more than half of the TeV blazars are HBLs. This is expected since the HBL SEDs typically extend to higher frequencies and they are more likely to reach the TeV band. Another typical property of TeV blazars is that their redshift distribution does not exceed ~ 0.5, since the universe is practically opaque to TeV γ rays beyond that distance, due to $\gamma - \gamma$ pair production of TeV γ rays with extragalactic background light (EBL) photons. This makes TeV blazars important probes in EBL studies [Orr and others, 2011]. In the TeV band, some TeV blazars have been observed to undergo strong flares, with a flux increase of several tens of their baseline emission and rapid variabilities as fast as subhour timescales (see 5.1).

3.3.1 Correlations Between TeV Emission and Other Bands

The question of whether/how the TeV emission is correlated with the rest of the continuum has been under investigation and is crucial in understanding the complete picture of blazar radiation

mechanisms. A good way of looking for correlations is to study simultaneous multiwavelength data taken during TeV flares. For instance if we consider a TeV HBL, the IC component typically spans HE to VHE γ rays. In parallel to this, the falling edge of the synchrotron component, that corresponds to synchrotron radiation emmitted by the highest energy electrons, coincides with the X-ray band. Consequently, X-ray data reflects the part of the electron population with shortest cooling time scales and exhibits rapid flares of the order of day scales [Tanihata and others, 2003].

Assuming a one-zone SSC model, where the non-thermal emission is supposed to originate from a single region in the relativistic jet, one would expect an X-ray flare to be accompanied by a TeV flare of an HBL [Katarzyński, 2011]. There have been indeed several detections of simultaneous X-ray and TeV flares, but with higher degrees of correlation as opposed to linear [Fossati and others, 2008]. TeV flares that were not accompanied by any X-ray flare have been observed as well [Krawczynski and others, 2004].

On the other hand, quite a few TeV blazars have been discovered and TeV flares of known sources have been detected in response to optical triggers [Albert and others, 2006]. Simultaneous activity in optical and TeV bands could be expected particularly in non-HBL blazars, where the synchrotron peak is not far from the optical band. Similar to the case of X-rays, several examples of coinciding optical and γ-ray activities have been observed but counter-examples exist as well, suggesting the possibility of multi-zone emission [Reinthal and others, 2012].

3.3.2 Indirect Studies Involving TeV Blazar Emission

TeV emission from blazars has implications that are used in many studies, such as extragalactic background light (EBL) measurement, extragalactic magnetic fields (EGMF) measurement, and investigation of Lorentz invariance violation (LIV).

EBL photons pair produce with TeV photons ($\gamma\,\gamma \;\rightarrow\; e^+ + e^-$), whereby causing a redshift-dependent attenuation of the TeV emission from blazars. Hence, studying the TeV spectrum of blazars at various redshifts can be used to constrain the EBL emission (see, e.g., [Orr and others, 2011; Georganopoulos and others, 2010]). EBL models predict that no TeV emission would be detected from blazars at distances larger than a redshift of ~ 0.5. The newly established lower limit of 0.6035

for the redshift of the HBL object PKS 1424+240 [Furniss and others, 2013] is a recent example of how TeV blazar studies contribute to the measurement of the EBL spectrum.

EGMF studies focus on the cascade emission from TeV blazars. VHE gamma rays emitted by blazars initiate electromagnetic cascades in the intergalactic medium, generating emission in the HE gamma ray band. The cascade electrons and positrons are deflected by the EGMF and their emission is detected with characteristic angular and temporal distributions correlated with the EGMF. A lower limit on the EGMF strength can be calculated by requiring that the cascade flux that originates from the VHE emission does not exceed the measured HE flux or the corresponding upper limit [Huan and others, 2011].

Some quantum gravity models predict variations in the speed of light, which would mean a violation of Lorentz invariance. According to some of these models, this speed variation depends on the photon energy. Therefore, one way to test the LIV is to look for an energy-dependent dispersion in photon arrival times in TeV flares. Ideally the flare should be rapid, extending over a large range of energies and coming from a cosmological distance, that would correspond to a large travel time. TeV blazar flares have been studied to probe this quantum gravity effect, and to place constraints on the energy dependent correction factors for the speed of light in the absence of such dispersion (see, e.g., [Albert and others, 2008a]).

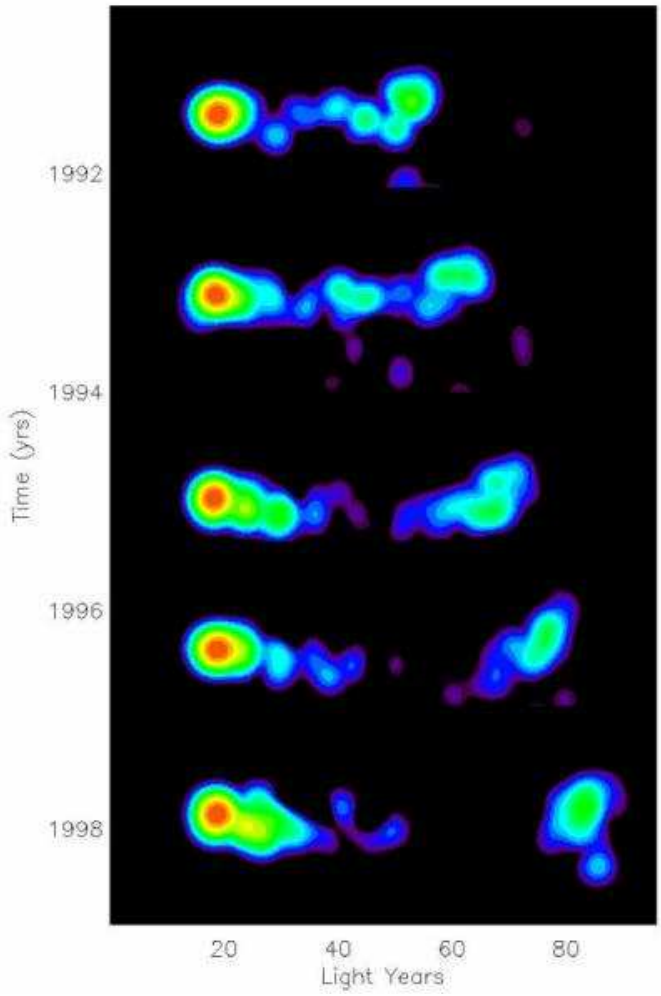

Figure 3.3: Superluminal motion observed in K-band (22 GHz) radio images of the quasar 3C 279. The blue-green blob on the right displaced by a distance of 25 lightyears from 1991 to 1998, thus appearing to move faster than light. This measured speed is due to light-travel-time effects, as a result of the relativistic speed of the blob along a direction almost aligned (within 2°) with our line of sight. See text for details. Image courtesy of NRAO/AUI.

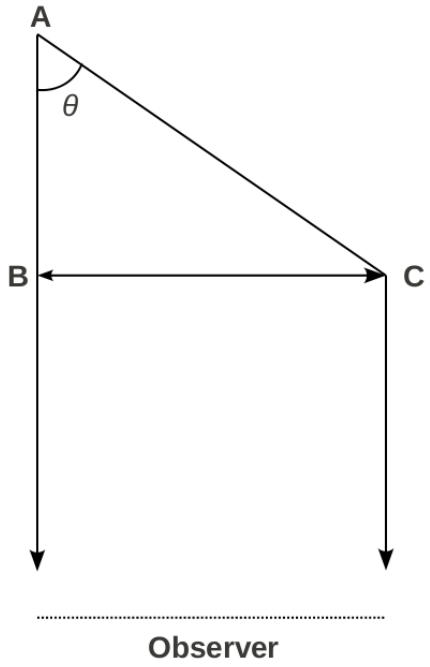

Figure 3.4: Schematic diagram illustrating the motion of a blob in an AGN exhibiting superluminal motion.

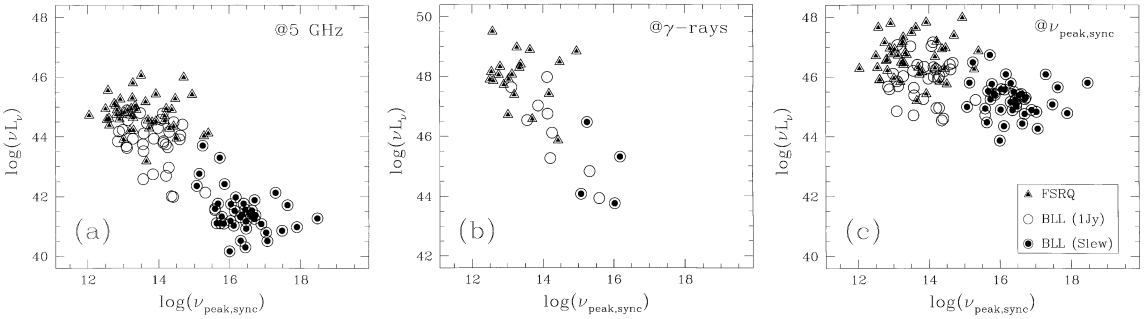

Figure 3.5: Plots illustrating blazar sequence trends, see the text for details. Radio (5 GHz), γ ray (100 MeV) and synchrotron peak luminosities versus peak frequency of the synchrotron component $\nu_{\rm syn}$ calculated from polynomial fits to the SEDs. BLL (1Jy) represent the radio selected blazars and BLL (Slew) X-ray selected ones, that correspond to LBLs and HBLs, respectively. In all plots, all three groups of objects appear to be more or less separated in the parameter space but they also clearly form a continuum together. Figure from [Fossati and others, 1998].

Part III

Results

Chapter 4

The TeV Discovery of the BL Lac Object RBS 0413

VERITAS observed the HBL object RBS 0413 starting in 2008 and detected VHE gamma-ray emission from the object in October 2009. This is an interesting dicovery since VERITAS observations in the fall of 2009 were triggered by extrapolation studies of the HE flux reported by *Fermi*-LAT into the VHE range, that eventually led to the detection of a signal above the energy of 250 GeV. In this chapter we describe the VERITAS data analysis and present the results, including a spectral energy distribution and modeling of the simultaneous HE γ-ray (*Fermi*-LAT), and quasi-simultaneous X-ray (*Swift*-XRT), ultraviolet (*Swift*-UVOT) and *R*-band optical (MDM) data. This chapter is based on the article [Aliu and others, 2012a], that was led by the author and from which Figures 4.3, 4.4, 4.5, and Tables 4.1 and 4.2 were taken.

4.1 Historical Background

RBS 0413 was discovered in the X-ray band, identified and named 1E 0317.0+1834, during the Einstein Medium Sensitivity Survey and was optically identified as a BL Lac [Gioia and others, 1984]. The object was also detected as a radio emitter with the Very Large Array of the National Radio Astronomy Observatory [Stocke and others, 1990]. It exhibits sig-

nificant and variable optical polarization [Stocke and others, 1985]. Having a featureless optical spectrum [Stocke and others, 1989], as is typical of BL Lac objetcs, and an estimated synchrotron peak frequency $\log(\nu_{\rm peak}/{\rm Hz}) = 16.99$ [Nieppola and others, 2006], RBS 0413 is classified as an HBL. It is located at the redshift of 0.190
[Stocke and others, 1985].

The MAGIC Collaboration observed RBS 0413 from December 2004 to February 2005 for a livetime of 6.9 hr and reported a VHE flux upper limit of 4.2×10^{-12} erg cm^{-2} s^{-1}, at 200 GeV, assuming a power-law spectrum with a photon index of 3.0
[Albert and others, 2008b]. VERITAS observed the source in the 2008–2009 season and obtained a marginal statistical significance of $\sim$ 3 standard deviations (σ). In 2009, *Fermi*-Large Area Telescope (LAT) detected HE emission from the direction of RBS 0413
[Abdo and others, 2010a], triggering new VERITAS observations by private communication. These new observations, combined with the previous data, resulted in the discovery of RBS 0413 as a VHE γ-ray emitter in October 2009.

4.2 VERITAS Observations and Results

VERITAS observed RBS 0413 for 48 hours in total, using wobble mode, with north, south, east and west wobble positions. After discarding observing runs compromised by bad weather, and a small number affected by hardware problems, 26 hours remained for analysis. One third of these data were obtained with the old array layout (Sep 2008 - Feb 2009, MJD 54732–54883) and the rest with the new array (Sep 2009 - Jan 2010, MJD 55092–55485) (see Chapter 2). Approximately 3 hours of data with the old array were taken under weak moonlight, which leads to a higher energy threshold for those observations. The source elevation in the data set ranges from 57° to 79°, with an average of $\sim$ 70°. For signal extraction, a θ^2 cut of 0.0169, optimized for a point source of 1% strength of the Crab Nebula, was used. In this study VERITAS standard data analysis was used, as described in Section 2.4.

RBS 0413 is a weak source in the VHE regime. Using a reflected-region background estimation,

an excess of 180 events and a significance of 5.5σ were obtained, for the source location at RA = $03^{\rm h}19^{\rm m}47^{\rm s} \pm 4^{\rm s}_{\rm stat} \pm 7^{\rm s}_{\rm syst}$ and decl. = $18°45'.7 \pm 1'.0_{\rm stat} \pm 1'.8_{\rm syst}$ (J2000 coordinates). The VERITAS signal is consistent with a point source, and the object was named VER J0319+187. Figure 4.1 shows the excess counts map and the significance map for the detected source. The cumulative significance (significance as a function of time) and the θ^2 distribution plot of the signal are shown in Figure 4.2. The energy distribution of γ-ray events extends from $\sim$ 250 GeV to $\sim$ 1.0 TeV (see Table 4.1 for a list of spectral data points) and is well described by a power-law function, $dN/dE = F_0 E^{-\Gamma}$. The best fit is obtained with photon index $\Gamma = 3.18 \pm 0.68_{\rm stat} \pm 0.30_{\rm syst}$ and flux normalization $F_0 = (1.38 \pm 0.52_{\rm stat} \pm 0.60_{\rm syst}) \times 10^{-7}$ TeV^{-1} m^{-2} s^{-1} at 0.3 TeV, with a value of χ^2 per degree of freedom (χ^2/dof) of 0.14/2 (see Figure 4.3).

The integral flux above 250 GeV is $(1.5 \pm 0.6_{\rm stat} \pm 0.7_{\rm syst}) \times 10^{-8}$ m^{-2} s^{-1}, corresponding to a flux level of approximately 1% the flux of the Crab Nebula. No significant flux variability is detected (see Figure 4.4 caption for details of the light-curve analysis). An upper limit (99% confidence level) on the fractional variability amplitude ($F_{\rm var}$, [Vaughan and others, 2003]) yields $F_{\rm var} < 3.2$.

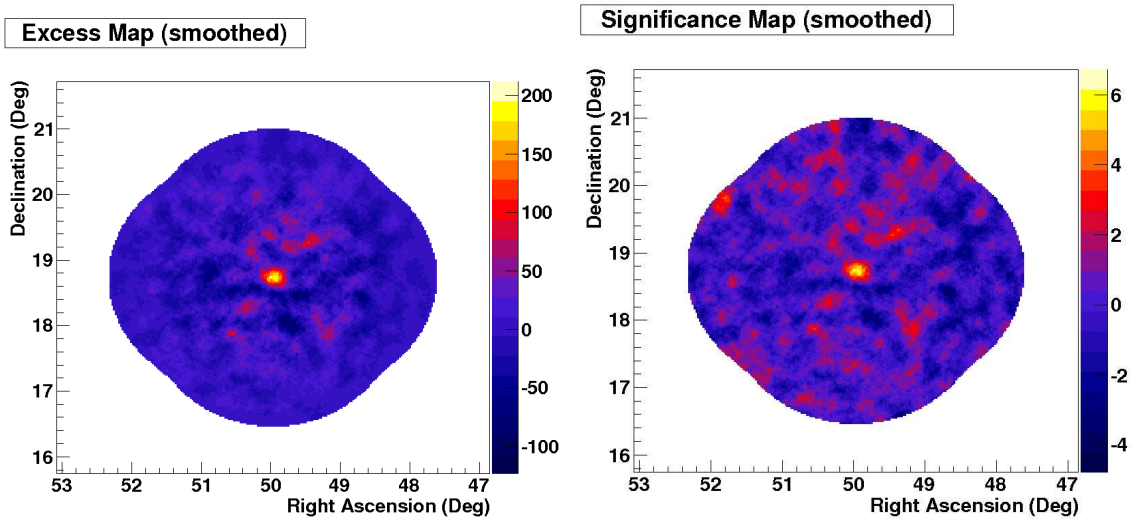

Figure 4.1: Excess counts map (left) and significance map (right) for the RBS 0413 analysis. Color bars show the excess counts (left) and the significance(right).

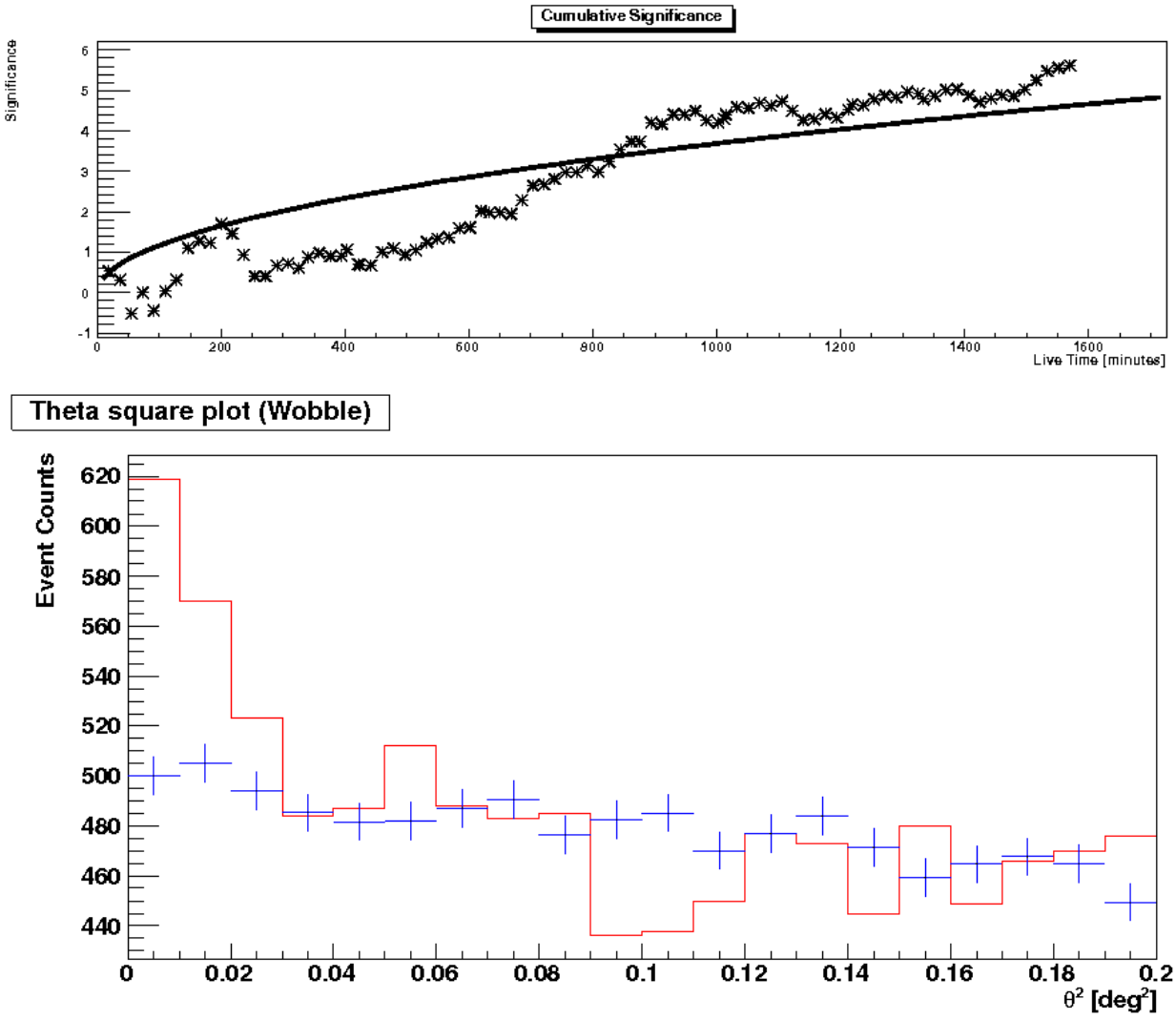

Figure 4.2: Top: Significance of the signal as a function of time. Bottom: θ^2 distribution of the signal.

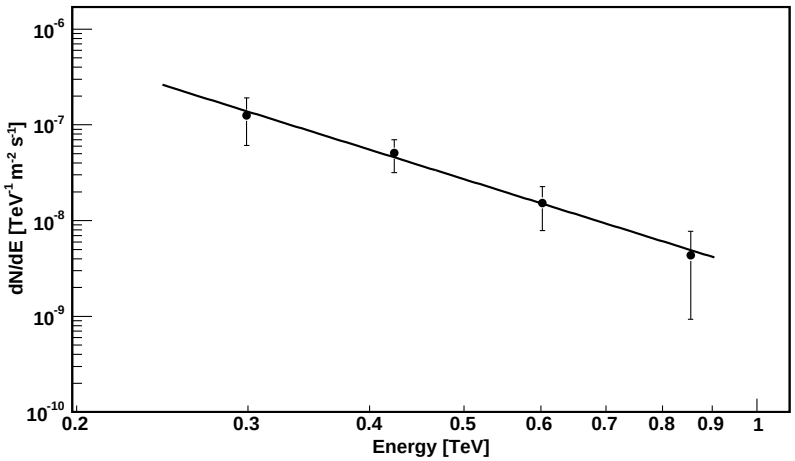

Figure 4.3: VERITAS measured photon spectrum of RBS 0413. See the text for the parameters of the power-law fit shown.

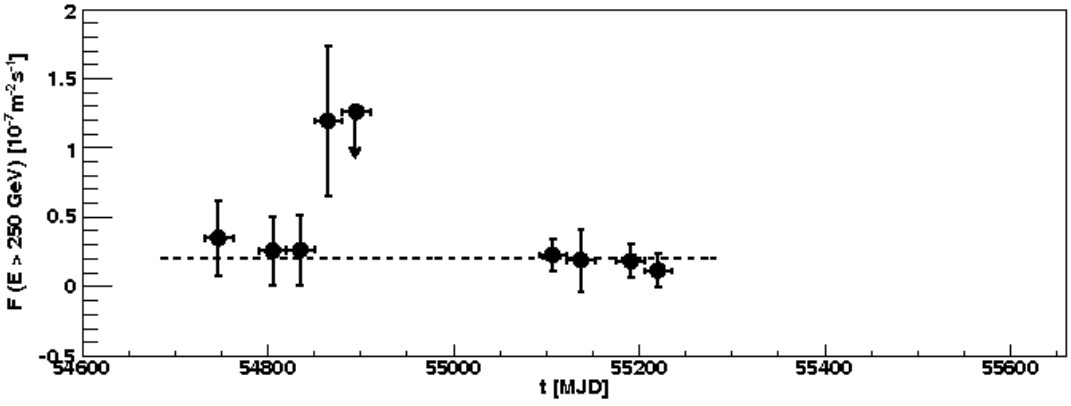

Figure 4.4: 30-day light curve for the VERITAS data. A fit with a constant function gives a χ^2/dof value of 14/8, corresponding to a fit probability of 8%, consistent with the hypothesis of a constant flux. The negative flux point corresponding to the upper limit point in the light curve was included in the fit.

4.3 Contemporaneous Multiwavelength Data

In order to understand the emission mechanism in the blazar, contemporaneous data were assembled and the SED was modeled with three different approaches. Figure 4.5 shows the broadband SED of RBS 0413. *Fermi*-LAT observations were performed in survey mode, covering the entire VERITAS exposure. On the other hand, optical, UV and X-ray data are not strictly simultaneous with VERITAS, but were all taken within the VERITAS observation window quoted above.

The R-band optical data were taken with the 1.3 m McGraw-Hill telescope at the MDM observatory on Kitt Peak, Arizona, between 2009 December 10 and 13 . The flux shows variations of up to $\sim 30\%$ from day to day, with an average of $(2.47 \pm 0.02) \times 10^{-12}$ erg cm^{-2} s^{-1}. In the case of RBS 0413, the host galaxy is expected to make a substantial contribution to the observed R-band flux. We have taken this into account in our SED modeling by adding a phenomenological host galaxy SED to our model.

The VERITAS detection triggered a *Swift* [Gehrels and others, 2004] target-of-opportunity observation of RBS 0413 in X-ray and UV bands, on 2009 November 11, for a total exposure of 2.4 ks. An absorbed power-law model, including the *phabs*[1] model for photoelectric absorption, was fitted to the X-ray photon spectrum. Over the energy range 0.3–10 keV, the best-fit photon index is $\Gamma = 2.22 \pm 0.07$, and the normalization at 1 keV is (33.1 ± 2.2) keV^{-1} m^{-2} s^{-1}. The unabsorbed integral flux is $F(0.3\text{-}10\,\mathrm{keV}) = (1.69 \pm 0.12) \times 10^{-11}$ erg cm^{-2} s^{-1} in the range 0.3–10 keV. The absorbed integral flux in the range 2–10 keV is $F(2\text{-}10\,\mathrm{keV}) = (5.81 \pm 0.55) \times 10^{-12}$ erg cm^{-2} s^{-1}. No flux variability is evident over the 2.4 ks exposure.

[1]The *phabs* tool applies absorption using photoelectric cross-sections.

Energy (TeV)	Flux (m^{-2} s^{-1} TeV^{-1})	Significance (σ)
0.30	$(1.3 \pm 0.7) \times 10^{-7}$	2.1
0.42	$(5.1 \pm 1.9) \times 10^{-8}$	3.0
0.60	$(1.5 \pm 0.7) \times 10^{-8}$	2.3
0.85	$(4.3 \pm 3.4) \times 10^{-9}$	1.2

Table 4.1: Differential flux measurements of RBS 0413 above 250 GeV with VERITAS. The first column shows the mean energies, weighted by the spectral index. The errors are statistical only.

UV observations were taken in the photometric band *UVM2* (2246 Å) [Willott and others, 2008]. The measured flux is $(2.75 \pm 0.11) \times 10^{-12}$ erg cm^{-2} s^{-1}.

GeV observations carried out by *Fermi*-LAT cover the period from 4 August 2008 to 4 January 2011. A point source positionally consistent with RBS 0413 was detected with a significance of more than 9σ (test statistic, TS=89; see [Mattox and others, 1996]). The photon energy spectrum between 300 MeV and 300 GeV is best described by a power-law function. The time-averaged integral flux is $(1.64 \pm 0.43_{\rm stat}{}^{+0.31}_{-0.22_{\rm sys}}) \times 10^{-5}$ m^{-2} s^{-1}, and the spectral index is $1.57 \pm 0.12_{\rm stat}{}^{+0.11}_{-0.12_{\rm sys}}$. No evidence for variability was found.

4.4 Modeling of Spectral Energy Distribution

The non-thermal continuum of RBS 0413 shown in Figure 4.5 exhibits a double-peaked shape, as is typical for blazars. In this study, we applied three different time-independent models (including leptonic as well as hadronic) to the observed SED. For all of the models, the emission region was assumed to be a spherical blob of size $R_{\rm b}$, moving within the jet with a bulk Lorentz factor Γ. $R_{\rm b}$ was constrained using the optical minimum variability timescale $\log(\Delta t_{\rm min}) = 3.75$ [Xiang and Dai, 2007], where $\Delta t_{\rm min}$ is in units of seconds. The angle between the line of sight of the observer and the jet axis, represented by $\theta_{\rm obs}$, was chosen to be equal to $1/\Gamma$. This is referred to as the critical or superluminal angle, for which the Doppler factor equals Γ. The synchrotron emission was assumed to originate from relativistic electrons with Lorentz factors distributed between $\gamma_{\rm min}$ and $\gamma_{\rm max}$, following a power law with a spectral index $q_{\rm e}$, under the influence of a magnetic field B. The particle-escape timescale is represented by $t_{\rm esc} = \eta_{\rm esc} R_{\rm b}/c$, where $\eta_{\rm esc}$ is the particle-escape parameter. For each model, the parameters were adjusted to describe the data and achieve an equilibrium between the acceleration of the injected particles, the radiative cooling and the particle escape [Böttcher, 2010]. The output parameters were used to calculate the relative partition between the magnetic field energy density and the kinetic luminosity of relativistic particles ($\epsilon_{\rm Be,p} \equiv L_{\rm B}/L_{\rm e,p}$) for each model. All model spectra were corrected for extragalactic background light (EBL) absorption using the model from [Finke and others, 2010a]. For the optical

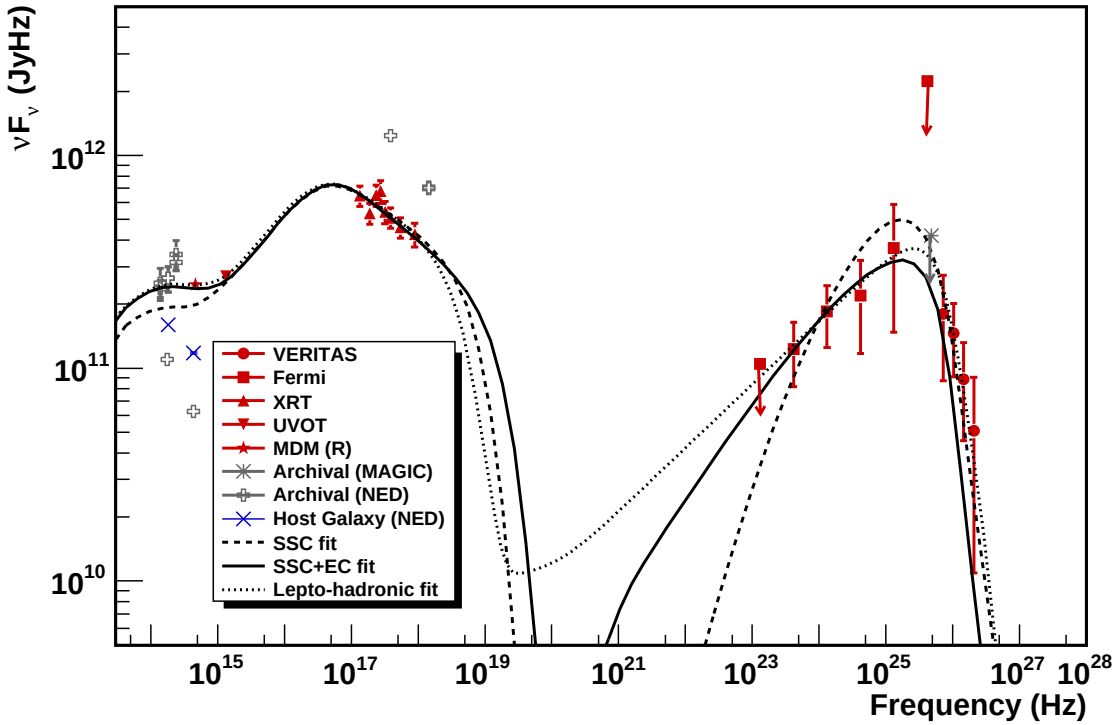

Figure 4.5: RBS 0413 spectral energy distribution [Aliu and others, 2012a]. VERITAS data were corrected for the EBL absorption using the EBL model from [Finke and others, 2010a]. See the text for details on the emission models that were tested on the data.

band, a phenomenological SED reproducing the archival host galaxy spectral points was added to the model.

The first model we applied assumed a homogenous one-zone SSC scenario. The magnetic field energy density required in this model is only 6% of the value corresponding to equipartition with the relativistic electron distribution ($\epsilon_{\rm Be} = 0.06$). The model spectrum is too hard in the *Fermi* band (strongly curved, with $\Gamma \sim 1.5$ around 10^{23} Hz) and too soft in the VERITAS band ($\Gamma = 4.0$), albeit within the errors in both cases. On the other hand, while the X-ray measurements are well reproduced, the optical (R-band) spectrum is not.

Next, we tested a combined SSC+EC model. The external source of photons was assumed to be an isotropic thermal blackbody (BB) radiation field, which may be due to a torus of warm dust with temperature $T_{\rm ext} = 1.5 \times 10^3$ K. The assumed BB infrared (IR) radiation field corresponds

to a νF_ν flux of $\sim 5 \times 10^8 \times R^2{}_{pc}$ JyHz, where R_{pc} is the characteristic size of the IR emitter in units of parsecs. It should be noted that this quantity is far below the measured IR flux, thus consistent with our observations. The addition of an EC component improves the modeling for the optical and *Fermi* data compared with the pure SSC model and leads to values for the model parameters which are very close to equipartition ($\epsilon_{Be} = 1.20$). However, the model tends to have too sharp a cutoff in the VHE band and therefore underpredicts the VERITAS flux measurements. This could be remedied by choosing a much weaker magnetic field and higher electron energies, but the resulting system would then be very far from equipartition, with ϵ_{Be} reduced by at least two orders of magnitude.

The last model we tested is a combined lepto-hadronic jet model as described in [Böttcher, 2010]. In this case, the HE component of the non-thermal emission is dominated by a combination of synchrotron radiation from ultrarelativistic protons ($E_{max} >\sim 10^{19}$ eV) and photons from the decay of neutral pions. Secondary electrons that are produced in various electromagnetic cascades are the origin of the low-energy synchrotron emission. The kinetic energy of the relativistic proton population was assumed to have a single power-law distribution in the energy range $1.0 \times 10^3\,\mathrm{GeV} < E_p < 1.6 \times 10^{10}\,\mathrm{GeV}$, with a spectral index $q_p = 2.4$. The model is a good description of the overall SED, and the system is close to equipartition between the magnetic field and the total relativistic particle content dominated by protons ($\epsilon_{Bp} = 0.95$). As is typical for lepto-hadronic models, the acceleration of protons to ultrarelativistic energies ($\sim 10^{10}$GeV) requires a high magnetic field, 30 G in this case. Although the lepto-hadronic model provides the best description for the data, it has two more free parameters than the SSC+EC model and is therefore less constraining. The parameters that best represent the data for all three models are summarized in Table 4.2.

4.5 Discussion

Based on our calculations, all three models are good at describing the observed data. It appears that if the criterion of equipartition is taken as a reasonable measure of successful blazar emission

Parameter	Symbol	SSC	SSC+EC	Lepto-hadronic
Electron low-energy cutoff*	$\gamma_{\rm min}$	7.0×10^4	5.0×10^4	4.5×10^3
Electron high-energy cutoff*	$\gamma_{\rm max}$	1.0×10^6	1.0×10^6	5.0×10^4
Injection electron spectral index*	q_e	2.4	2.5	2.4
Escape-time parameter ($t_{\rm esc} = \eta_{\rm esc} R_{\rm b}/c$)*	$\eta_{\rm esc}$	10	300	100
Magnetic field (gauss)*	B	0.1	0.22	30.0
Bulk Lorentz factor*	Γ	20	20	15
Doppler factor	D	20	20	15
Blob radius ($\times 10^{16}$cm)*	$R_{\rm b}$	1.1	1.6	0.5
Observing angle	$\theta_{\rm obs}$	2°.87	2°.87	3°.82
External radiation field E density (erg cm^{-3})*	$u_{\rm ext}$	...	6×10^{-7}	...
External radiation field BB temperature*	$T_{\rm ext}$	...	1.5×10^3 K	...
Proton spectrum low-energy cutoff (GeV)*	$E_{\rm p,min}$	...	...	1.0×10^3
Proton spectrum high-energy cutoff (GeV)*	$E_{\rm p,max}$	...	...	1.6×10^{10}
Spectral index of proton distribution*	$q_{\rm p}$	...	...	2.4
Kinetic luminosity in protons (erg s^{-1})*	$L_{\rm p}$	...	...	2.0×10^{46}
Kinetic luminosity in electrons (erg s^{-1})*	$L_{\rm e}$(jet)	2.97×10^{43}	1.55×10^{43}	6.26×10^{40}
Magnetic field energy density (erg s^{-1})	$L_{\rm B}$(jet)	1.82×10^{42}	1.86×10^{43}	1.90×10^{46}
Equipartition parameter	ϵ	$\epsilon_{\rm Be} = 0.06$	$\epsilon_{\rm Be} = 1.20$	$\epsilon_{\rm Bp} = 0.95$
Redshift	z	0.19	0.19	0.19

Table 4.2: Output parameters for the SED of RBS 0413 for the SSC, SSC+EC, and lepto-hadronic models. The parameters that were left free are marked with an asterisk. $\theta_{\rm obs}$ is the superluminal angle (see Section 4.4).

models, SSC+EC is preferred over SSC for this HBL, which seems to be in contrast with some previous blazar studies. See [Ghisellini and others, 1998] for arguments relating the presence of an EC component with the blazar sequence and

[Abdo and others, 2010b] for a discussion of issues encountered in explaining blazar SEDs with a simple one-zone homogeneous SSC model. On the other hand, we cannot discriminate between leptonic and lepto-hadronic mechanisms, since the SSC+EC and lepto-hadronic models provide equally reasonable descriptions for the observed non-thermal continuum, and we did not detect variability in the HE and VHE regimes given the limited statistics. Since the synchrotron cooling timescales for electrons and protons are different, the detection of intraday variability would be harder to explain with a lepto-hadronic scenario and would accordingly favor a purely leptonic scenario. Therefore, any future observation of rapid variability would be helpful in distinguishing between the SSC+EC and lepto-hadronic models.

Chapter 5

GeV-TeV Properties of TeV Blazars

In this chapter we present the results from our study of a sample of TeV-detected blazars. We compiled the TeV spectra from literature and analyzed 27 months of *Fermi*-LAT data to obtain a GeV spectrum for each of our TeV data sets. We combined the GeV and TeV spectra using a flux-based data selection method and studied the combined spectral properties such as IC peak frequency, variability, spectral features, and TeV spectral hardness. This chapter is based on the article [Senturk and others, 2013], from which all the figures and tables were taken.

5.1 Data Sample

Our blazar sample contains all blazars with a published VHE spectrum before February 2011, including a total of 26 sources (see Table 5.1): 19 HBLs, 3 IBLs, 2 LBLs and 2 FSRQs. TeV spectral index distributions of the whole sample are shown in Figure 5.1. Three of these blazars have insecure redshifts either because the spectroscopic measurements were inconclusive, or the calculations were made indirectly based on EBL absorption studies. References for the adopted redshift values in these three cases are given in Table 5.1. Seven of our targets were detected with EGRET [Thompson and others, 1993], the predecessor of *Fermi*, and 23 of them are in the 2FGL catalog [Nolan and others, 2012]. The ones that are missing in the *Fermi* data (1ES 0229+200, 1ES 0347-121, PKS 0548-322) are very hard spectrum sources that would be weak in the *Fermi*

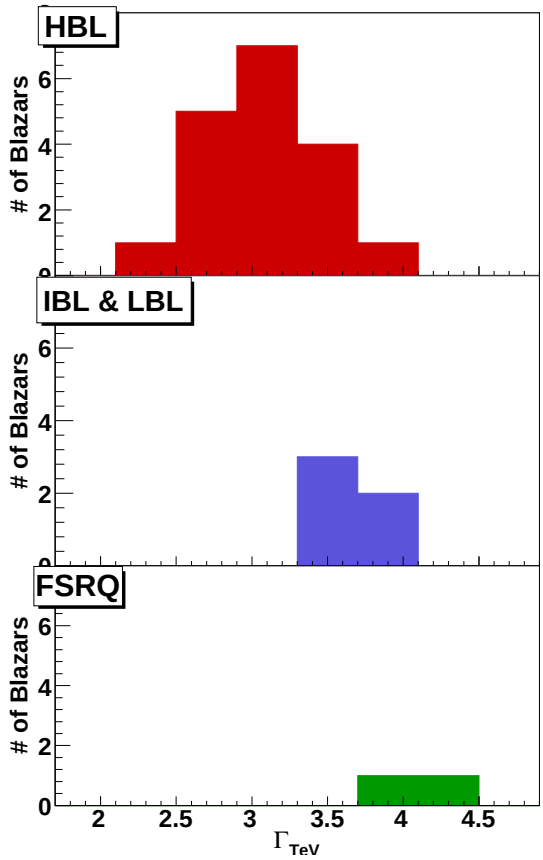

Figure 5.1: TeV photon index distribution for our sample (see Table 5.1). For blazars that have multiple published results in Table 5.1, the most recent one was used. Top, middle and bottom panels show HBLs, IBLs+LBLs, and FSRQs, respectively. HBLs tend to have harder spectra than the rest of the sample. FSRQs have the softest spectra. Note that the TeV indices are not EBL-corrected.

band. More than half of the sample have been detected multiple times in the VHE band. These multiple detections extending over several years and obtained mostly with different instruments suggest that spectral variability in the VHE band is a common property for VHE blazars. Even though no general pattern has been established for VHE variability, several sources have been observed to have a flux increase up to a few times their baseline emission [Acciari and others, 2009b; Albert and others, 2007e; Aharonian and others, 2007c], occasionally accompanied by a change in spectral index
[Albert and others, 2007e] and minute-scale flux doubling times [Albert and others, 2007e; Aharonian and others, 2

The first 27-month *Fermi* data and archival VHE spectra published before February 2011 were used to construct combined GeV-TeV SEDs in this study. Only in six cases (RGB J0710+591, 1ES 1218+304, PKS 1424+240, PKS 2155-304 and two different measurements for 3C 66A) were the VHE data found to overlap with the *Fermi* era. The remainder of the VHE data were taken before the *Fermi* mission.

All VHE spectra were corrected for the EBL absorption using the model by
[Domínguez and others, 2011]. Other background models are also available
(e.g., [Finke and others, 2010b]). However, with a different EBL model, we do not expect any significant differences in our results up to a few TeV, given the redshift and energy range of our sample. See section 5.3.2 for a more detailed discussion on the EBL correction effects on our study.

5.2 *Fermi* Analysis

The fact that most of the GeV and TeV data are not contemporaneous makes it hard to interpret the combined spectra of blazars. Moreover, *Fermi* data represent an average state over relatively long periods, whereas the VHE spectra consist of "snapshots", mostly taken during flares. To account for blazar variability and the non-contemporaneous nature of the data set, for bright enough sources, the Fermi data were split into "low" and "high" flux states as described below. Thus, non-contemporaneous GeV and TeV measurements were matched in a more realistic way than directly using all the time-averaged *Fermi* data. Table 5.1 summarizes the *Fermi* flux states

	(1)	(2)	(3)	(4)	(5)	(6)	(7)	(8)	(9)
RGB J0152+017	HBL	0.080	–	–	average	$2.95 \pm 0.36_{\rm stat} \pm 0.20_{\rm syst}$	2%	300	[Aharonian and others, 2008a]
3C 66A*	IBL	0.444[a]	15.63	171	MAGIC	$3.64 \pm 0.39_{\rm stat} \pm 0.25_{\rm syst}$	6%	200	[Aleksić and others, 2011b]
					VERITAS	$4.1 \pm 0.4_{\rm stat} \pm 0.6_{\rm syst}$	8%	100	[Acciari and others, 2009c]
1ES 0229+200	HBL	0.140	19.45	–	average	$2.50 \pm 0.19_{\rm stat} \pm 0.10_{\rm syst}$	2%	580	[Aharonian and others, 2007d]
1ES 0347-121	HBL	0.188	17.94	–	average	$3.10 \pm 0.23_{\rm stat} \pm 0.10_{\rm syst}$	2%	250	[Aharonian and others, 2007b]
PKS 0548-322	HBL	0.069	16.84	–	average	$2.86 \pm 0.34_{\rm stat} \pm 0.10_{\rm syst}$	1%	200	[Aharonian and others, 2010]
RGB J0710+591	HBL	0.125	21.05	6	VERITAS	$2.69 \pm 0.26_{\rm stat} \pm 0.20_{\rm syst}$	3%	300	[Acciari and others, 2010a]
S5 0716+714	LBL	0.300	14.46	266	high	$3.45 \pm 0.54_{\rm stat} \pm 0.2_{\rm syst}$	9%	400	[Anderhub and others, 2009a]
1ES 0806+524	HBL	0.138	16.56	20	average	$3.6 \pm 1.0_{\rm stat} \pm 0.3_{\rm syst}$	2%	300	[Acciari and others, 2009a]
1ES 1011+496	HBL	0.212	16.74	16	high	$4.0 \pm 0.5_{\rm stat} \pm 0.2_{\rm syst}$	6%	200	[Albert and others, 2007a]
1ES 1101-232	HBL	0.186	16.88	1	average	$2.94 \pm 0.20_{\rm stat}$	3%	225	[Aharonian and others, 2007a]
Markarian 421*	HBL	0.031	18.49	44	medium	$2.20 \pm 0.08_{\rm stat} \pm 0.2_{\rm syst}$	50–200%	200	[Albert and others, 2007d]
Markarian 180	HBL	0.046	18.61	10	average	$3.3 \pm 0.7_{\rm stat} \pm 0.2_{\rm syst}$	11%	200	[Albert and others, 2006]
1ES 1218+304*	HBL	0.182	19.14	15	average	$3.08 \pm 0.34_{\rm stat} \pm 0.2_{\rm syst}$	7%	200	[Acciari and others, 2009d]
					VERITAS	$3.07 \pm 0.09_{\rm stat}$	6%	200	[Acciari and others, 2010b]
W Comae*	IBL	0.102	14.84	47	high	$3.81 \pm 0.35_{\rm stat} \pm 0.34_{\rm syst}$	9%	200	[Acciari and others, 2008]
PKS 1222+21	FSRQ	0.432	13.27	101	MAGIC	$3.75 \pm 0.27_{\rm stat} \pm 0.2_{\rm syst}$	100%	100	[Aleksić and others, 2011a]
3C 279	FSRQ	0.536	12.67	898	high	$4.1 \pm 0.7_{\rm stat} \pm 0.2_{\rm syst}$	15%	200	[Albert and others, 2008c]
PKS 1424+240	IBL	0.260[b]	15.7	26	VERITAS	$3.80 \pm 0.5_{\rm stat} \pm 0.3_{\rm syst}$	3%	140	[Acciari and others, 2010c]
H 1426+428	HBL	0.129	18.55	7	average	–	3%	1000	[Horns and others, 2004]
PG 1553+113	HBL	0.4[c]	16.49	44	high	$3.4 \pm 0.1_{\rm stat} \pm 0.2_{\rm syst}$	8%	200	[Aleksić and others, 2010]
Markarian 501*	HBL	0.034	16.84	46	low	$2.79 \pm 0.12_{\rm stat}$	20%	200	[Anderhub and others, 2009b]
1ES 1959+650*	HBL	0.048	18.03	16	low	$2.58 \pm 0.18_{\rm stat}$	10%	200	[Tagliaferri and others, 2008]
PKS 2005-489*	HBL	0.071	–	9	average	$3.20 \pm 0.16_{\rm stat} \pm 0.10_{\rm syst}$	3%	400	[Acero and others, 2010]
PKS 2155-304*	HBL	0.117	15.7	63	HESS	$3.34 \pm 0.05_{\rm stat} \pm 0.1_{\rm syst}$	14%	400	[Aharonian and others, 2009]
					low	$3.53 \pm 0.06_{\rm stat} \pm 0.10_{\rm syst}$	15%	200	[Abramowski and others, 2010b]
BL Lacertae	LBL	0.069	14.28	35	high	$3.64 \pm 0.54_{\rm stat} \pm 0.2_{\rm syst}$	3%	200	[Albert and others, 2007b]
1ES 2344+514*	HBL	0.044	16.4	10	average	$2.95 \pm 0.12_{\rm stat} \pm 0.2_{\rm syst}$	11%	200	[Albert and others, 2007c]
H 2356-309	HBL	0.165	17.24	8	average	$3.06 \pm 0.15_{\rm stat} \pm 0.10_{\rm syst}$	2%	240	[Abramowski and others, 2010a]

[a] [Miller and others, 1978; Lanzetta and others, 1993]
[b] [Prandini and others, 2011]
[c] [Mazin and F., 2007]
* Blazars that are reported as variable in the TeV band, according to TeVCat (http://tevcat.uchicago.edu/).

Table 5.1: GeV-TeV properties of the VHE blazar sample taken from the literature. Columns (1), (2) and (3) show the spectral energy distribution (SED) type, redshift, and synchrotron peak frequency ($\nu_{\rm syn}$), respectively. *Fermi* variability indices (4) were taken from the 1FGL catalog [Abdo and others, 2010a]. *Fermi* states (5) are identified in this work using 27 month *Fermi* light curves as described in Section 5.2. In cases where *Fermi* data are contemporaneous with TeV observations, the corresponding TeV instruments are listed in Column (5). TeV spectral indices (6) were taken from the references listed (9). TeV integral fluxes (7) are above the listed energy threshold (8) and in units of Crab Nebula flux. For the Crab Nebula unit conversions, spectral measurements above 350 GeV from [Çelik, 2008] are used.

and VHE spectra used for each source.

For VHE data that were taken during the *Fermi* era, time periods of a few months that cover the corresponding VHE observations were selected for the *Fermi* spectral analysis. For blazars that have VHE spectra measured before the *Fermi* era, the first 27-month of *Fermi* data was analyzed (from 4 August 2008 to 4 November 2010). In all the analysis steps, an energy selection from 300 MeV to 100 GeV was applied to the data.

The *Fermi* data were analyzed in the following way. First, a 27-month light curve analysis was performed for each source using an aperture photometry technique. *Diffuse class* events from a region of 1° radius from the target location were selected and counts were plotted as a function of time, each time bin containing 49 counts, corresponding to a signal to noise ratio of 7. For sources with high statistics, low- and high- flux states were identified and separated using the average count rate as a threshold. Figure 5.2 shows the resulting light curves for all sources, with fluxes normalized to arbitrary units. It should be noted that in this analysis, no background subtraction was performed and therefore the resulting light curves merely give an estimate of high- and low-state time slices.

Next, a spectral analysis was done for each data set. *Diffuse class* events from a region of interest of 8° radius were selected and analyzed with Fermi Science Tools v9r18p6[1], using instrument response functions P3_V6_DIFFUSE. Sources from the first *Fermi*-LAT (1FGL) catalog [Abdo and others, 2010a], bright spots with test statistics > 25 and standard galactic and isotropic diffuse emission background components[2] within the region of interest were included in the source model files. Unbinned maximum-likelihood analysis as described in [Cash, 1979; Mattox and others, 1996] was applied to each data set, assuming a power-law (PL) spectrum as given in eq. 5.1.

$$\mathrm{d}N/\mathrm{d}E = N_0(E/E_0)^{-\Gamma} \tag{5.1}$$

Additionally, to look for possible spectral features in the data, spectral points were calculated and fitted with different power-law functions, and the results were compared. See Section 5.3.4 for more

[1] http://fermi.gsfc.nasa.gov/ssc/data/analysis/scitools/overview.html

[2] http://fermi.gsfc.nasa.gov/ssc/data/access/lat/BackgroundModels.html

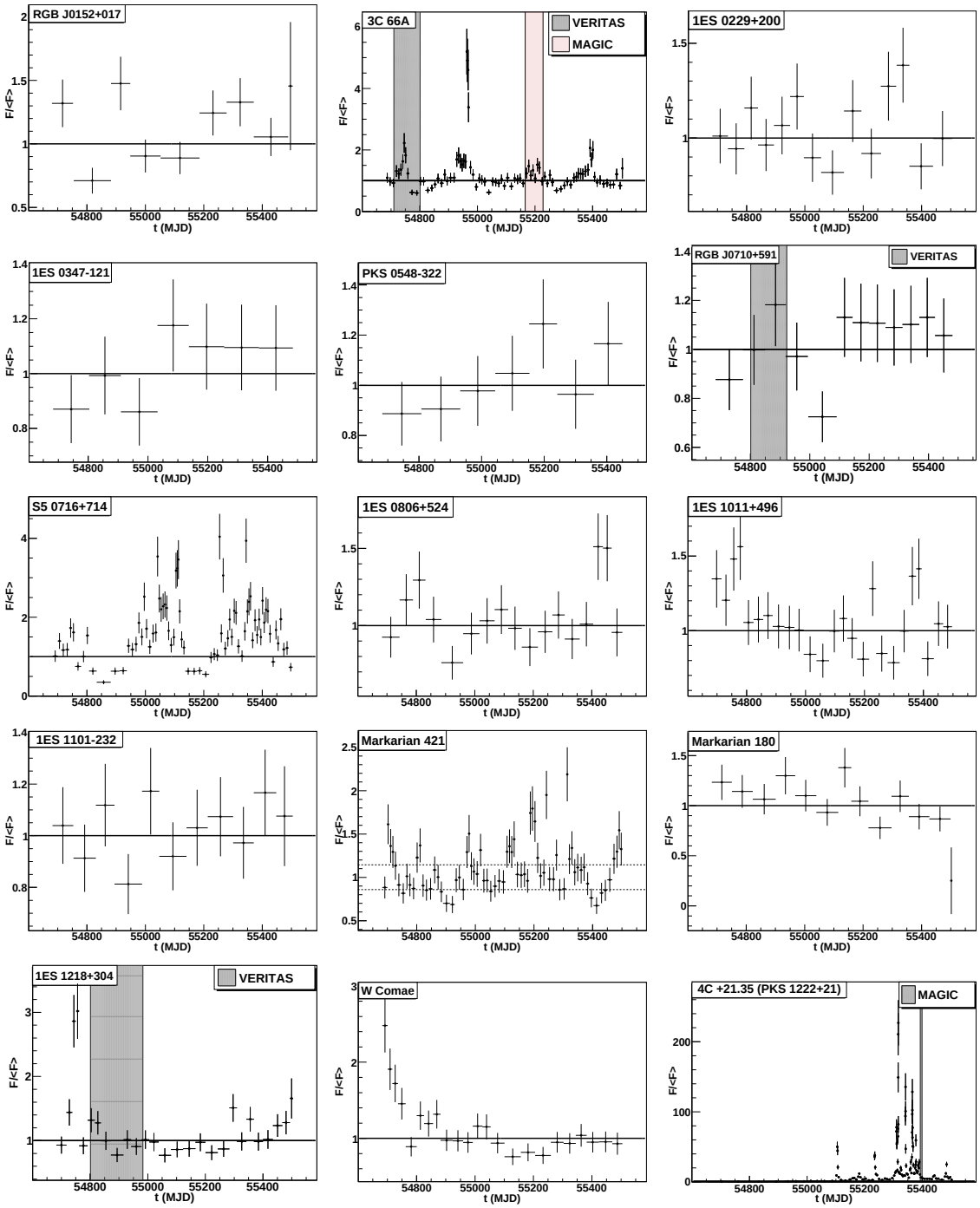
RGB J0152+017
3C 66A
VERITAS
MAGIC
1ES 0229+200
1ES 0347-121
PKS 0548-322
RGB J0710+591
VERITAS
S5 0716+714
1ES 0806+524
1ES 1011+496
1ES 1101-232
Markarian 421
Markarian 180
1ES 1218+304
VERITAS
W Comae
4C +21.35 (PKS 1222+21)
MAGIC
F/<F>
t (MJD)

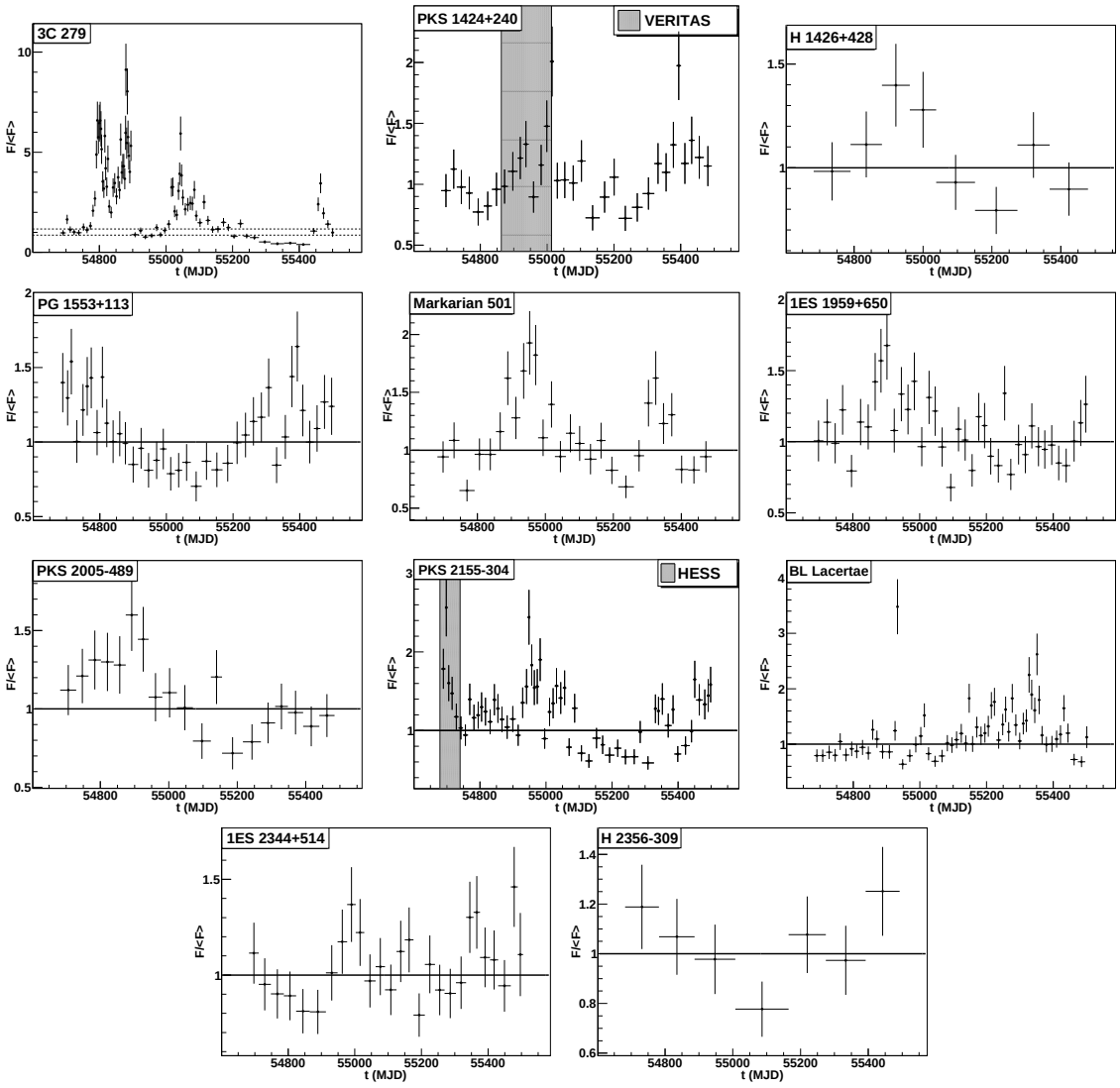

Figure 5.2: *Fermi*-LAT aperture photometry light curves with no background subtraction, normalized to arbitrary units. The solid lines, representing the average counts per area per time, separate "low" and "high" flux states, that are later on used to produce "low" and "high" state spectra. In the case of Markarian 421 and 3C 279 light curves, the dashed lines represent 1 σ deviation from the average, dividing the data set into three separate flux states ("low", "medium", and "high"). The shaded areas show the contemporaneous time windows with the corresponding TeV instruments.

details.

Finally, combined GeV-TeV SED data sets were constructed using archival TeV spectra and the corresponding flux state information from references shown in Table 5.1. With each TeV spectrum, the most suitable *Fermi* data subset (average, low- or high- state) was used for further study.

5.3 Results and Discussion

Twelve out of 26 blazars did not have enough statistics for a temporal separation of the *Fermi* data set into different flux states. Therefore for this subsample, an average spectrum was calculated using the entire data set. Data from another subsample with 12 blazars were split into high and low-flux states as described in Section 5.2. Data from the two brightest blazars (Markarian 421 and 3C 279) were split into 3 subsets, with low, medium and high-flux states. See Table 5.3 for a summary of our *Fermi* data analysis results.

Our analysis results are consistent with the 2FGL catalog [Nolan and others, 2012]. We used the combined GeV-TeV SEDs (see Figure 5.3) to estimate the IC peak frequency band of each blazar (see Section 5.3.1). Our sample contains a handful of candidate "TeV-peaked" blazars that we discuss in Section 5.3.2. In addition, considering the fact that *Fermi* spectral indices do not vary significantly between low- and high-states, we studied the change in spectral index from GeV to TeV as a function of the redshift, thus confirming the EBL effect on TeV spectra with a model-independent approach (see Section 5.3.3). On the other hand, interesting spectral features in the GeV band are observed. To probe these features, the data were fitted with three different functions and the corresponding fit improvements were calculated (see Section 5.3.4). Finally, in Section 5.3.5, we extended this study to contemporaneous combined SEDs.

5.3.1 IC Peak Frequency

The peak frequency of the IC component is a salient parameter for describing blazar non-thermal continua and studying population trends. Systematic studies for measuring the IC peak frequency mostly suffer from the lack of statistics and simultaneous data. A similar work was carried out

Name	SED type (1)	z (2)	$F_{\rm var}$ (3)	*Fermi* state (4)	$\Gamma_{\rm GeV}$ (5)	$F_{1-100}(\rm cm^{-2}s^{-1})$ (6)	TS (7)	Live time (day) (8)
RGB J0152+017	HBL	0.080	0.19	average	2.09 ± 0.14	$(7.70 \pm 1.26) \times 10^{-10}$	106	822
3C 66A*	IBL	0.444[a]	0.59	MAGIC	2.09 ± 0.06	$(2.41 \pm 0.19) \times 10^{-8}$	953	62
				VERITAS	1.91 ± 0.05	$(2.50 \pm 0.16) \times 10^{-8}$	1485	91
1ES 0229+200	HBL	0.140	0.07	average	2.23 ± 0.34	$(2.96 \pm 1.07) \times 10^{-10}$	21	822
1ES 0347-121	HBL	0.188	< 0.12	average	0.85 ± 0.54	$(5.33 \pm 3.90) \times 10^{-11}$	16	822
PKS 0548-322	HBL	0.069	< 0.14	average	1.65 ± 0.25	$(2.93 \pm 1.00) \times 10^{-10}$	40	822
RGB J0710+591	HBL	0.125	< 0.11	VERITAS	1.44 ± 0.33	$(9.94 \pm 4.09) \times 10^{-10}$	33	121
S5 0716+714	LBL	0.300	0.44	high	2.13 ± 0.04	$(2.01 \pm 0.09) \times 10^{-8}$	3644	342
1ES 0806+524	HBL	0.138	0.13	average	1.77 ± 0.07	$(1.45 \pm 0.14) \times 10^{-9}$	400	822
1ES 1011+496	HBL	0.212	0.15	high	1.97 ± 0.04	$(7.82 \pm 0.47) \times 10^{-9}$	1705	332
1ES 1101-232	HBL	0.186	< 0.10	average	1.88 ± 0.26	$(4.59 \pm 1.27) \times 10^{-10}$	47	822
Markarian 421*	HBL	0.031	0.22	medium	1.78 ± 0.02	$(2.64 \pm 0.08) \times 10^{-8}$	7943	350
Markarian 180	HBL	0.046	0.22	average	1.87 ± 0.08	$1.22 \pm 0.12 \times 10^{-9}$	356	822
1ES 1218+304	HBL	0.182	0.44	average	1.69 ± 0.06	$(2.80 \pm 0.23) \times 10^{-9}$	708	822
				VERITAS	1.84 ± 0.11	$(3.30 \pm 0.49) \times 10^{-9}$	187	182
W Comae*	IBL	0.102	0.32	high	2.07 ± 0.06	$(8.34 \pm 0.59) \times 10^{-9}$	1101	222
PKS 1222+21	FSRQ	0.432	1.42	simultaneous	2.17 ± 0.04	$(7.24 \pm 0.47) \times 10^{-6}$	4267	6
3C 279	FSRQ	0.536	0.65	high	2.37 ± 0.02	$(5.25 \pm 0.15) \times 10^{-8}$	13558	218
PKS 1424+240	IBL	0.260[b]	0.22	VERITAS	1.85 ± 0.05	$(1.21 \pm 0.09) \times 10^{-8}$	1116	150
H 1426+428	HBL	0.129	0.07	average	1.12 ± 0.16	$(4.05 \pm 0.86) \times 10^{-10}$	197	822
PG 1553+113	HBL	0.4[c]	0.16	high	1.74 ± 0.03	$(1.66 \pm 0.07) \times 10^{-8}$	3339	344
Markarian 501*	HBL	0.034	0.25	low	1.84 ± 0.05	$(5.78 \pm 0.36) \times 10^{-9}$	1280	458
1ES 1959+650*	HBL	0.048	0.14	low	2.04 ± 0.06	$(4.45 \pm 0.30) \times 10^{-9}$	834	443
PKS 2005-489	HBL	0.071	0.15	average	1.82 ± 0.05	$(3.37 \pm 0.23) \times 10^{-9}$	834	822
PKS 2155-304*	HBL	0.117	0.29	HESS	1.89 ± 0.05	$(3.20 \pm 0.24) \times 10^{-8}$	1308	61
				low	1.95 ± 0.03	$(1.55 \pm 0.06) \times 10^{-8}$	4118	420
BL Lacertae	LBL	0.069	0.37	high	2.34 ± 0.04	$(1.52 \pm 0.07) \times 10^{-8}$	2517	283
1ES 2344+514*	HBL	0.044	0.09	average	1.97 ± 0.07	$(2.09 \pm 0.19) \times 10^{-9}$	407	822
H 2356-309	HBL	0.165	0.04	average	2.40 ± 0.18	$(5.63 \pm 0.81) \times 10^{-10}$	108	822

[a] [Miller and others, 1978; Lanzetta and others, 1993]
[b] [Prandini and others, 2011]
[c] [Mazin and F., 2007]
* Blazars that are reported as variable in the TeV band, according to TeVCat (http://tevcat.uchicago.edu/).

Table 5.2: *Fermi* analysis results for the sample. Columns (1) and (2) are the same as in Table 5.1. $F_{\rm var}$ (3) is the calculated flux variability amplitude (See 5.3.3) for the 27-month period. *Fermi* states (4) are as described in Section 5.2. $\Gamma_{\rm GeV}$ (5) represents the photon index and F_{1-100} (6) the integral flux for 1–100 GeV. Test statistics (TS) and live time corresponding to the listed flux state are given in colunms (7) and (8) respectively.

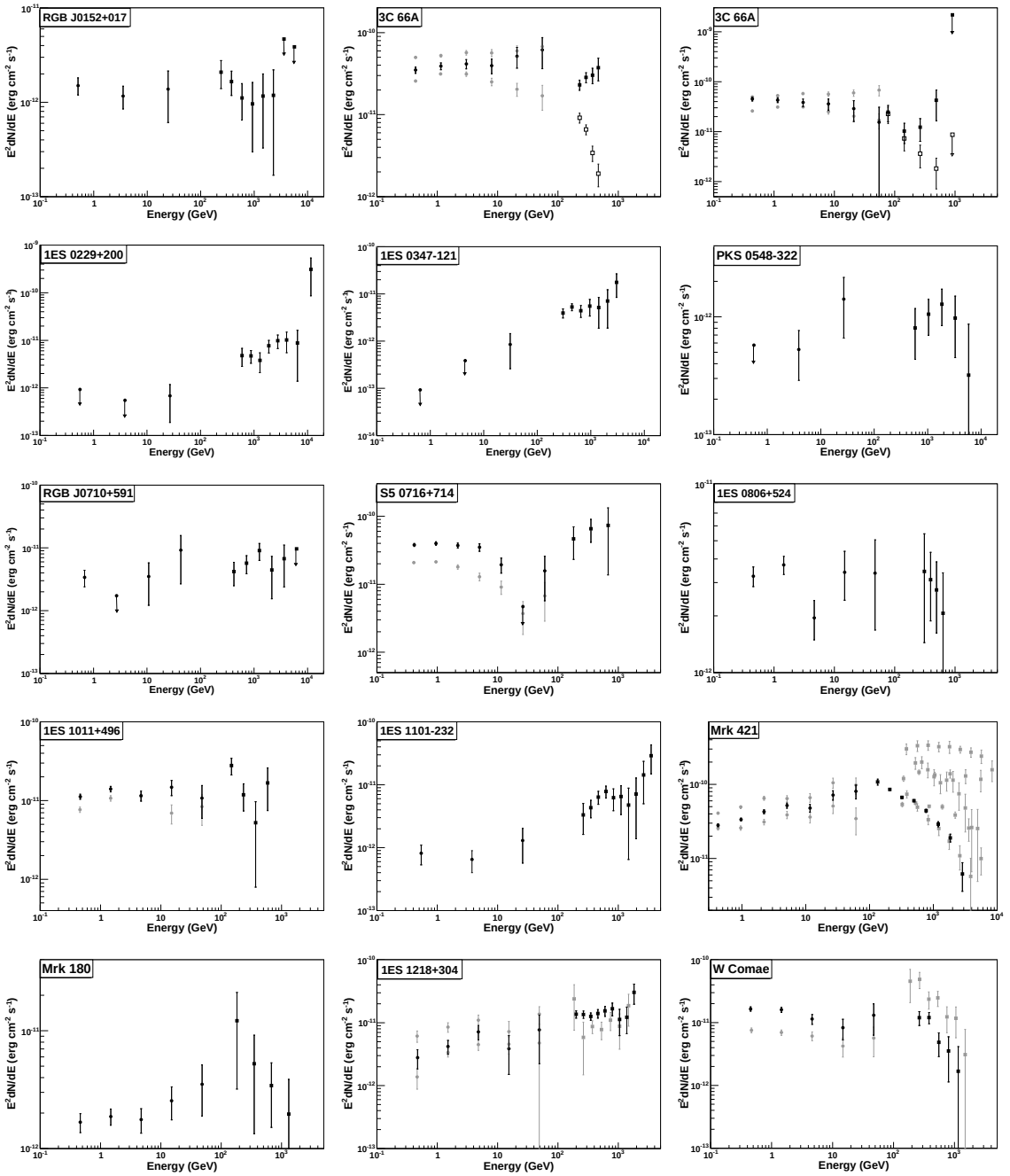
RGB J0152+017
3C 66A
3C 66A
1ES 0229+200
1ES 0347-121
PKS 0548-322
RGB J0710+591
S5 0716+714
1ES 0806+524
1ES 1011+496
1ES 1101-232
Mrk 421
Mrk 180
1ES 1218+304
W Comae
E²dN/dE (erg cm⁻² s⁻¹)
Energy (GeV)

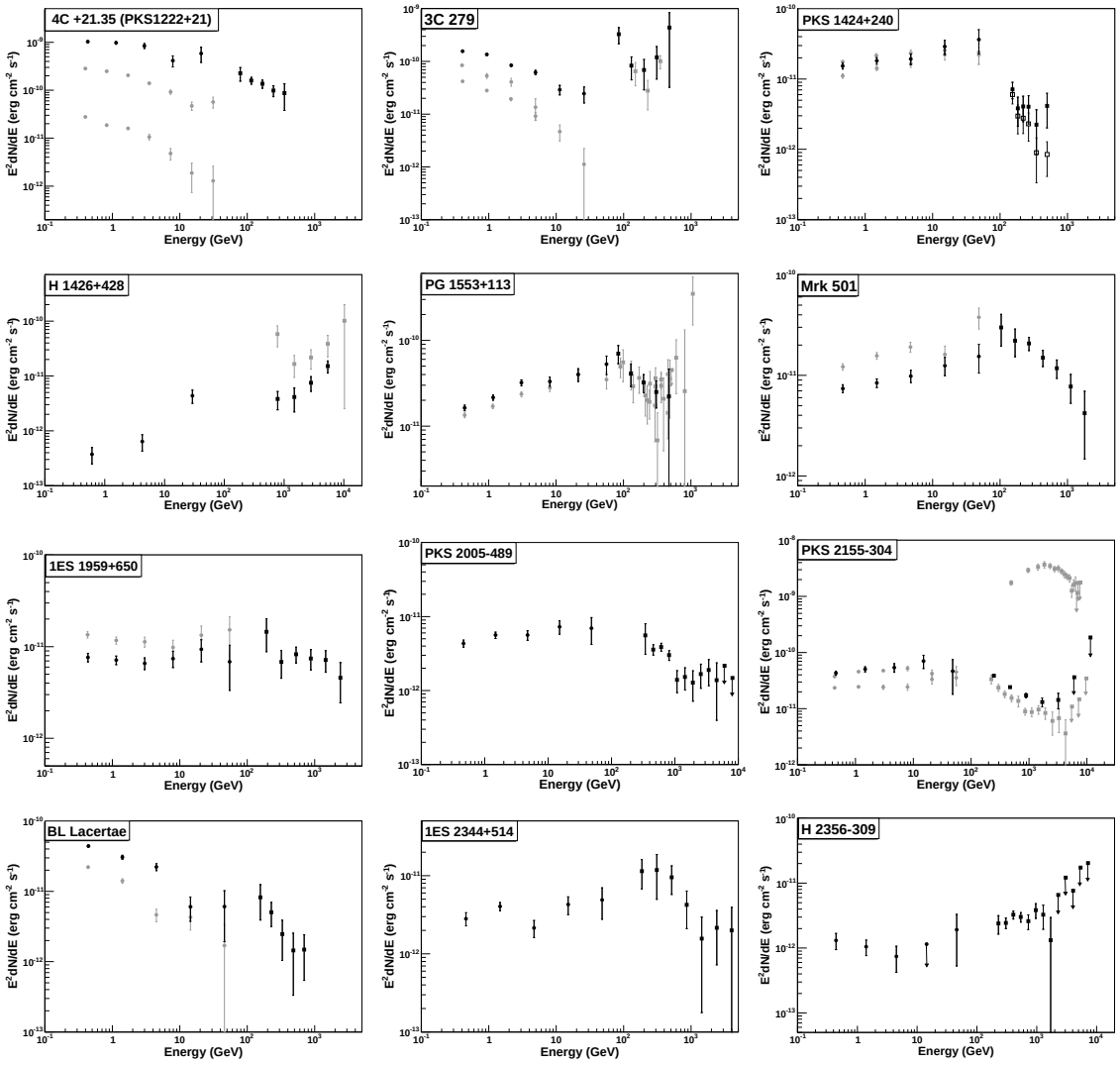

Figure 5.3: GeV-TeV spectra for the sample of blazars in this study. Filled circles represent the *Fermi* spectra and the filled squares the TeV spectra. Considering the TeV flux state information given in the TeV papers, the best matching GeV and TeV spectral points are used for the combined analysis (shown in black). When available, spectral points belonging to other flux states (in both bands) are plotted in gray. 3C66A (VERITAS and MAGIC respectively), RGB J0710+591, 1ES 1218+304, PKS 1222+21 (4C +21.35), PKS 1424+240, and PKS 2155-304 spectra are quasi-simultaneous.

in [Zhang and others, 2012], where archival multiwavelength data were used to model TeV blazar SEDs and determine the IC peak frequency ($\nu_{\rm IC}$). A positive correlation between $\nu_{\rm syn}$ and $\nu_{\rm IC}$ was reported. In this work, we focus on finding the IC "peak frequency band" rather than the "peak frequency", using a model independent approach. For each blazar SED shown in Figure 5.3, we identify the energy decade in which the largest amount of power is emitted. Note that the spectral points used in the VHE spectra are EBL-corrected. Figure 5.4 shows the distribution of the IC peak bands for different blazar types. We observe that the FSRQs, LBLs and IBLs have the maximum of their emission mostly below 1 GeV. On the other hand, HBLs tend to peak in the TeV range. This positive correlation between the synchrotron ($\nu_{\rm syn}$) and the IC peak frequencies ($\nu_{\rm IC}$), is in accordance with simple SSC models that predict a positive correlation between $\nu_{\rm syn}$ and $\nu_{\rm IC}$ [Abdo and others, 2010b]. The dashed lines represent the same distributions with the bright AGN sample from the first three months of *Fermi* data [Abdo and others, 2010b]. Our results tend to span the high frequency sides of all distributions and one clearly sees a shift to higher frequencies in the case of HBLs. This is expected since our sample consists of TeV-selected objects, that mostly correspond to relatively weak sources in the GeV data, and are therefore less likely to appear in a bright AGN sample. It should also be noted that we use a model independent method using only *Fermi* and VHE data, whereas [Abdo and others, 2010b] uses multiwavelength data and some modeling in cases where the soft X-ray band is dominated by the synchrotron component, a typical feature for our blazar sample.

5.3.2 Hard TeV BL Lac Objects

The combined GeV-TeV spectra of some blazars in our sample (1ES 0229+200, 1ES 0347-121, 1ES 1101-232, 1ES 1218+304, H 1426+428) suggest a $\nu_{\rm IC}$ beyond $\sim$ 1 TeV. These blazars are mostly weak or non-detected in the *Fermi* range, with a hard spectral index in both GeV and TeV bands. It follows that they may belong to the so-called ultra-high-frequency-peaked BL Lac sub-class (UHBLs, see, e.g., [Costamante and others, 2011]) that would constitute the extreme end of the population, and is expected to dominate the TeV luminosity of the universe. Several mechanisms have been set forth to explain the formation of these hard γ-ray spectra [Lefa and others, 2011].

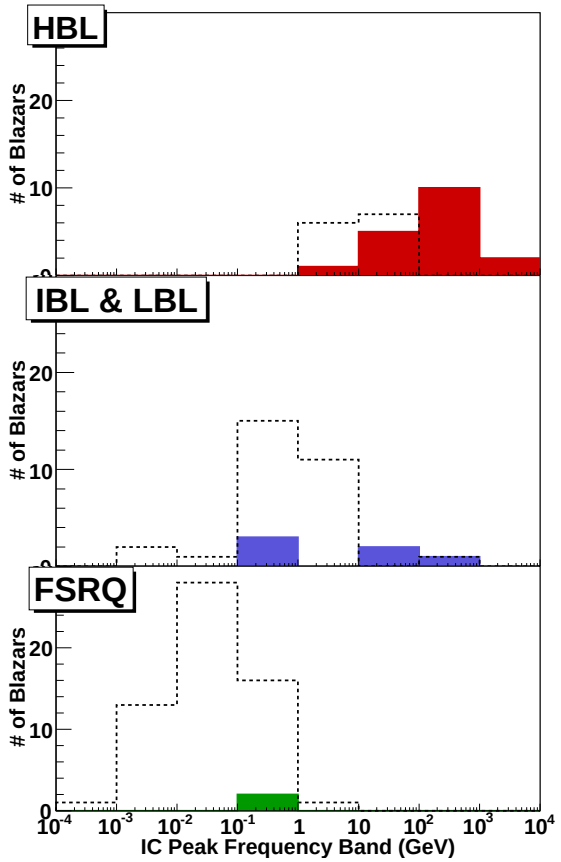

Figure 5.4: Distribution of the IC peak bands, defined as the energy decade in which the largest amount of power is emitted, in combined GeV-TeV spectra. Top, middle and bottom panels show HBLs, IBLs+LBLs, and FSRQs respectively. HBLs tend to peak at higher frequencies, in accordance with their respective synchrotron peak frequencies $\nu_{\rm syn}$ (see Table 5.1), and a decreasing trend in IC peak bands from top to bottom panel is seen. The dashed lines represent the same distribution for the blazar sample from [Abdo and others, 2010b].

Extensive spectral analysis of these objects would be valuable for EBL and intergalactic magnetic field measurements. It should be noted that at energies of a few TeV and beyond, our spectra become EBL-model-dependent. For this reason, we have compared our adopted EBL model with two other models from recent studies [Finke and others, 2010b; Franceschini and others, 2008]. We have found that for the data samples mentioned above, if we used either of the other two EBL models, the dispersion in highest energy flux points would be less than 20%, and consequently the observed spectral upturns would not be affected significantly.

With additional data, a deeper variability study carried on these blazars would relate to arguments that support the cosmic ray production as the origin of TeV blazar emission, since in that scenario no short time-scale variability would be expected to be observed [Murase and others, 2012]. Among the UHBL candidates, the ones that are present in the 1FGL catalog (1ES 1101-232, 1ES 1218+304, H 1426+428) have relatively small *Fermi* variability indices (see Table 5.1). In addition to that, our calculations of F_{var} for all 5 blazars using 27-month of *Fermi* data do not indicate a significant hint of variability either (see Table 5.3).

5.3.3 Spectral Variability

VHE emission from blazars is highly variable. This variability, manifested in irregular flares, is one of the most typical and promising blazar behaviors for studying the nature of underlying emission mechanisms. The observed flux change during a VHE flare can be as rapid as minute scales [Albert and others, 2007e] and as large as 40 times the baseline emission [Arlen and others, 2013]. Blazars that have been reported to have a variable flux are marked with an asterisk in Table 5.1. On the other hand, *Fermi* data does not exhibit flux variability as extreme as in the VHE band. In fact, having a smaller effective area than the ground-based VHE telescopes and operating mostly in survey mode rather than pointing, *Fermi*-LAT does not have the sensitivity to probe sub-hour time scale variability in blazars. Still, a possible correlation between GeV and TeV emission remains viable [Abdo and others, 2011; Aleksić and others, 2011a] and an enhanced activity in the high-energy tail of the *Fermi* band could therefore indicate a TeV flare. In this regard, monitoring GeV flares to trigger TeV observations is important [Errando and others, 2011], and potentially

could help in probing fast variability. To examine variability within the *Fermi* data, we compared high- and low-state *Fermi* spectra from 14 blazars (see Table 5.3). Half of these blazars have their integral flux in 1-100 GeV (F_{1-100}) increased by at least 90% in the high state. The largest flux increase is seen in the case of the two FSRQs 3C 279 and PKS 1222+21. As depicted by their respective light curves in Figure 5.2, these two objects have undergone dramatic GeV flares. Such a large scale flux increase does not hold for the remainder of the blazars. However, one should keep in mind that for most of the TeV blazars, the *Fermi* band is a relatively stable region of the SED, since it samples the low energy part of the parent electrons, that have a longer cooling time. Table 5.3 gives a summary of the results of the spectral variations seen in the *Fermi* data. We also calculated the variability amplitude ($F_{\rm var}$) within 27-month of *Fermi* data for each blazar, using the method described in [Vaughan and others, 2003]. $F_{\rm var}$ is a measure of the intrinsic source variance, calculated based on excess variance. For blazars with negative excess variance, 95% confidence level upper limits are given. The blazars 3C 66A, PKS 1222+21 and 3C 279 are the most variable ones according to this calculation ($F_{\rm var} > 0.5$). Our results are in agreement with the 1FGL catalog (see Table 5.1). Comparing these results with the TeV variability flags, we do not find any obvious relation between GeV and TeV variabilities (see Table 5.3).

Within the *Fermi* energy range, blazars in our sample do not exhibit dramatic changes in their spectral index between different flux states (see Table 5.3). Consequently, this makes the photon index a reasonable parameter to use for studying the non-contemporaneous combined SEDs. Figure 5.5 shows a scatter plot of observed $\Gamma_{\rm TeV} - \Gamma_{\rm GeV}$ versus redshift. A constant function does not provide a good description for the data, with $\chi^2/{\rm dof} = 204/27$, which could be interpreted as a model-independent indication for the EBL absorption. The difference between TeV and GeV photon indices increases with redshift. This is expected since the VHE γ-ray photons pair produce with the EBL photons [Franceschini and others, 2008] and this effect becomes more enhanced at larger redshifts, making the universe opaque to TeV γ rays at distances larger than $z \sim 0.5$. HE spectra are not affected by the EBL, whereas VHE spectra become softer with increasing redshift. A similar observation was reported by [Abdo and others, 2009], in a study carried out on a sample of TeV-selected AGN detected with *Fermi*.

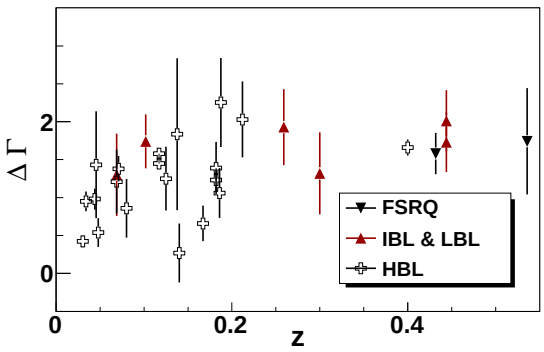

Figure 5.5: $\Delta\Gamma$ ($\Gamma_{\rm TeV} - \Gamma_{\rm GeV}$) vs. redshift. Empty crosses, triangles and inverse triangles represent HBLs, IBLs+LBLs, and FSRQs, respectively. The fact that a constant function does not provide a good description for the data could be interpreted as a model independent indication for the EBL absorption.

Figure 5.6 shows the relation between the spectral index $\Gamma_{\rm GeV}$ and the flux normalization F_{1-100} obtained from power-law fits. FSRQs and two subgroups of BL Lacs are clearly separated in the parameter space. This is in accordance with the aforementioned positive correlation trend between $\nu_{\rm syn}$ and $\nu_{\rm IC}$, since 1 GeV typically corresponds to the rising edge of the IC component in an HBL SED, sampling a relatively low flux with hard spectral index. On the other hand for an FSRQ, 1 GeV will correspond to the peak or the falling edge of the IC component. The fact that FSRQs have relatively more luminous IC emission explains the softening trend with a larger normalization factor. However, the pattern that we observe between different flux states of a given blazar is the opposite. In most cases, a slight spectral hardening accompanies high flux states, indicating a change in the spectral shape and enhanced flux increase at high-energy tail of the spectrum.

5.3.4 Spectral Features

In most of the blazars in our sample, we observe interesting spectral features in the *Fermi* band, that appear as dips in the 1–100 GeV energy range. In an attempt to find a quantitative description for these features, we fit the *Fermi* spectral points with a simple power law (PL, eq. 5.1) and a broken power law (BPL, eq. 5.2), and then compare the results.

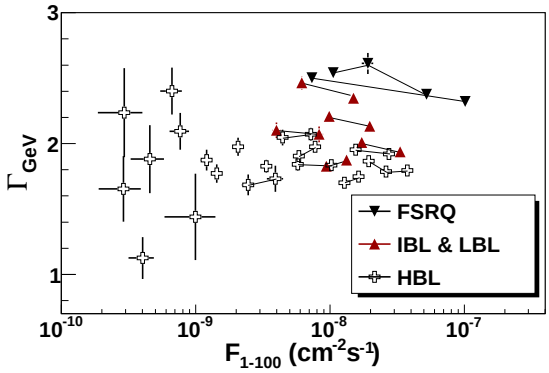

Figure 5.6: $\Gamma_{\rm GeV}$ vs. flux in the energy band 1-100 GeV from the analysis of 27-month *Fermi* data with a power law fit (see Table 5.3). Empty crosses, triangles and inverse triangles represent HBLs, IBLs+LBLs, and FSRQs, respectively. Solid lines connect different states of the same blazar.

Name	SED type (1)	Increase in F_{1-100} (%) (2)	$\Gamma_{\rm low}$ (3)	$\Gamma_{\rm high}$ (4)
3C66A	IBL	95	2.00 ± 0.02	1.93 ± 0.02
S5 0716+714	LBL	100	2.20 ± 0.03	2.13 ± 0.04
1ES 1011+496	HBL	30	1.90 ± 0.04	1.97 ± 0.04
Mrk 421	HBL	90	1.86 ± 0.03	1.79 ± 0.02
1ES 1218+304	HBL	60	1.68 ± 0.08	1.73 ± 0.10
W Comae	IBL	110	2.10 ± 0.06	2.07 ± 0.06
PKS 1222+21	FSRQ	1290	2.50 ± 0.04	2.32 ± 0.02
3C 279	FSRQ	395	2.54 ± 0.03	2.37 ± 0.02
PKS 1424+240	IBL	45	1.82 ± 0.04	1.87 ± 0.03
PG 1553+113	HBL	30	1.70 ± 0.03	1.74 ± 0.03
Mrk 501	HBL	80	1.84 ± 0.05	1.83 ± 0.04
1ES 1959+650	HBL	60	2.04 ± 0.06	2.07 ± 0.05
PKS 2155-304	HBL	80	1.95 ± 0.03	1.92 ± 0.02
BL Lacertae	LBL	140	2.46 ± 0.05	2.34 ± 0.04

Table 5.3: Spectral variations in *Fermi* data for blazars where at least two different *Fermi* flux states are available. Column (1) shows the spectral energy distribution (SED) type. F_{1-100} is the integral flux for 1–100 GeV. Column (2) shows the % increase in F_{1-100} from low to high *Fermi* state. FSRQs and LBLs seem to show the most important flux variability in this energy range. Columns (3) and (4) list the GeV photon indices in low and high *Fermi* states respectively. No significant change in photon index is seen, except for the two FSRQs where the index shows a slight hardening from low to high flux states.

$$dN/dE = N_0 \times \begin{cases} (E/E_b)^{-\Gamma_1}, & E < E_b \\ (E/E_b)^{-\Gamma_2}, & \text{otherwise} \end{cases} \tag{5.2}$$

In the PL fit, the normalization N_0 and the spectral index Γ are free parameters, and the energy E_0 is fixed at 1 GeV. In the BPL fit, the break energy E_b and the indices Γ_1 and Γ_2, along with the normalization N_0 are free. In Table 5.4, we list the best-fit parameters from both functions and the likelihood ratio test results of BPL over PL. In 9 out of 33 cases, BPL yields a better fit over PL with more than 2σ significance.

There are several possible mechanisms that may cause the observed features in the SEDs. One possibility is a break in the electron spectrum caused by the synchrotron cooling effects, generally yielding a change in spectral index by 0.5 [Chiang and Böttcher, 2002], which is in agreement with our results (see Table 5.4). Another mechanism that could explain the observed breaks is the absorption by an external photon field [Poutanen and Stern, 2010]. For those 9 data sets where the BPL gives a better fit than the PL, the break energy ranges from $\sim$ 2 GeV to $\sim$ 8 GeV. In addition, 7 of these data sets belong to non-HBL blazars, that are usually characterized by broad emission lines, thought to be originating from a region of molecular gas (broad line region; BLR) that is highly ionized by the optically thin accretion disk. This seems in accordance with the idea of relating the *Fermi* spectral features to absorption of GeV photons on radiation from H I (13.6 eV) and He II (54.4 eV) recombination continua in the BLR, that are expected to cause jumps in γ-ray opacity around $\sim$ 19.2 and $\sim$ 4.8 GeV, respectively [Poutanen and Stern, 2010]. We tested a general absorbed power-law (APL) function of the following form on the *Fermi* data:

$$dN/dE = N_0(E/E_0)^{-\Gamma} e^{-\tau_{\gamma\gamma}(E,z,E_\mathrm{abs})} \tag{5.3}$$

where the free parameters are the normalization N_0 at $E_0 = 1$GeV, photon index Γ, and absorption line energy E_abs. $\tau_{\gamma\gamma}$ is the optical depth for the γ-γ pair annihilation of photons with energies E and E_abs at a redshift of z. Within the *Fermi* energy band, BPL and APL functions fit the data equally well. Upturns at high-energy tails of *Fermi* spectra are observed (see, e.g.,

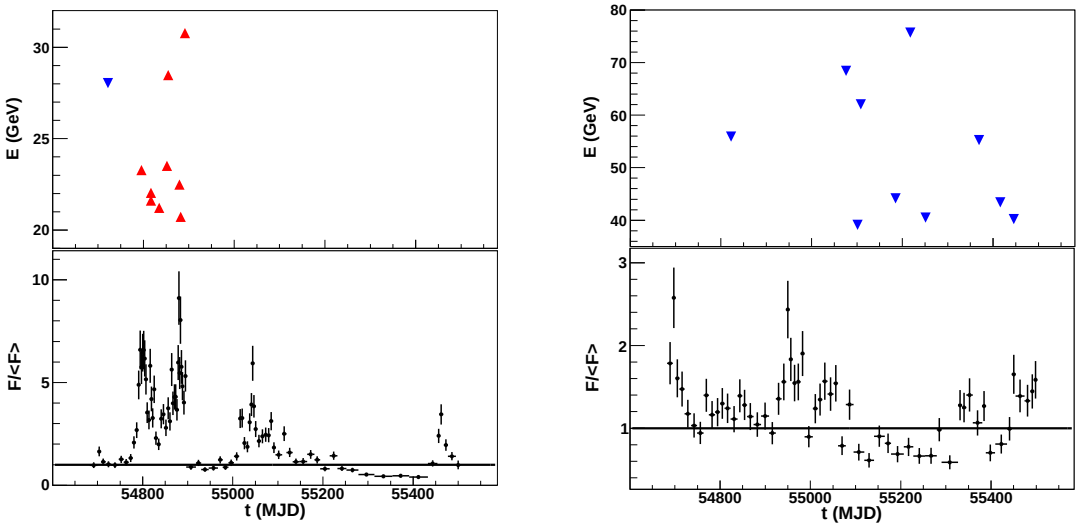

Figure 5.7: Arrival times of the photons in the highest energy bin (top panels) and aperture light curves with arbitrary flux units (bottom panels) for the blazars 3C 279 (*left*) and PKS 2155-304 (*right*). Blue upside-down triangles represent the low-state photons and red triangles the high-state ones. In both cases, the highest energy photons do not show any obvious clustering within their respective data sets. As described in Section 5.2, low- and high-states are distinguished based on the flux averages (solid lines) in light curves.

W Comae in Figure 5.3), but they are not statistically significant enough to favor an absorption scenario over a BPL fit. Therefore, it appears that one cannot statistically distinguish between the BPL and APL fits, but possible absorption scenarios are worth investigating further. To address this issue, we make use of contemporaneous GeV-TeV spectra to test and compare BPL and four different APL scenarios (see Section 5.3.5). This permits us to test the APL over a larger energy range and investigate the apparent *Fermi* spectral absorption-like features with higher statistics.

Another caveat related to these spectral features is that the upturn seen at the highest *Fermi* energy bin might be coming from a group of photons clustered in time. In that case the dip would be an artifact of a flaring event, thus not representative of the time-averaged spectrum. To make sure this is not the case, we checked the arrival times of the highest-energy photons and did not find any obvious clustering (see Figure 5.7). Note that the arrival time distributions should be considered within a given flux state. For instance, in the left panel of the figure, the red triangles represent the high energy photons from the high flux state and are evenly distributed in a time window that belongs to the high state. Therefore, one concludes that no clustering is found.

Name	Power Law		Broken Power Law				
	$N(\times 10^{-11})$	Γ	$F_{1\mathrm{GeV}}(\times 10^{-12})$	Γ_1	Γ_2	E_{break} (GeV)	σ_{BPL}
	(1)	(2)	(3)	(4)	(5)	(6)	(7)
3C66A (low)	2.78 ± 0.07	2.01 ± 0.02	9.30 ± 4.94	1.81 ± 0.06	2.22 ± 0.07	1.92 ± 0.51	4.12
S5 0716+714 (low)	1.85 ± 0.06	2.23 ± 0.03	5.18 ± 2.07	2.14 ± 0.04	2.74 ± 0.23	5.43 ± 1.01	3.07
S5 0716+714 (high)	3.68 ± 0.13	2.10 ± 0.03	2.29 ± 1.78	2.00 ± 0.06	2.57 ± 0.30	4.10 ± 1.47	2.29
1ES 1011+496 (low)	0.88 ± 0.04	1.94 ± 0.04	1.70 ± 1.34	1.70 ± 0.10	2.28 ± 0.20	2.76 ± 1.15	2.76
PKS 1222+21 (low)	1.72 ± 0.06	2.53 ± 0.04	0.99 ± 0.70	2.41 ± 0.06	3.11 ± 0.28	3.36 ± 0.87	2.84
3C 279 (low)	2.55 ± 0.08	2.59 ± 0.03	0.15 ± 0.28	2.53 ± 0.04	3.72 ± 1.54	7.70 ± 5.57	2.51
3C 279 (high)	1.16 ± 0.02	2.39 ± 0.02	8.14 ± 10.72	2.31 ± 0.03	2.74 ± 0.26	3.21 ± 1.79	3.11
PKS 2155-304 (low)	4.19 ± 0.10	1.92 ± 0.02	1.75 ± 1.98	1.86 ± 0.03	2.13 ± 0.14	5.54 ± 3.23	2.08
BL Lacertae (high)	3.26 ± 0.11	2.39 ± 0.04	1.08 ± 0.09	2.30 ± 0.04	3.00 ± 0.30	4.49 ± 0.03	2.50

Table 5.4: Fit results for power law (PL) and broken power law (BPL), where BPL yields a better fit over PL with more than 2σ significance (9 out of 33 cases). Columns (1) and (2) show the PL parameters, flux normalization at 1 GeV and the photon index respectively. $F_{1\mathrm{GeV}}$ (3) is the flux normalization at 1 GeV for BPL. N and $F_{1\mathrm{GeV}}$ are in erg cm^{-2} s^{-1}. Columns (4) and (5) show the photon indices for BPL, as given in eq. 5.2. The break energy for BPL is listed in column (6). σ_{BPL} (7) is the likelihood ratio test results of BPL over PL. For these 9 cases, the break energy E_{break} ranges from ~ 2 GeV to ~ 8 GeV. In addition, 7 of these data sets belong to non-HBL blazars.

5.3.5 Quasi-simultaneous GeV-TeV Spectra

Seven of the TeV spectra in our sample are contemporaneous with *Fermi* observations and therefore merit a deeper analysis. We extended the work described in section 5.3.4 to this subsample. This time, in addition to PL and BPL fits, we tested four different scenarios of absorption due to photons emitted from the broad line region (BLR): H I line (13.6 eV), He II line (54.4 eV), H I & He II combined, and full BLR spectrum taken from [Poutanen and Stern, 2010].

For single- and double-line absorption scenarios, H I and He II recombination continua are the most plausible cases given that they are the most dominant ones in the BLR spectrum, and that the breaks we see in the *Fermi* spectra are located around a few GeV. As for the full BLR spectrum, it was modeled assuming a photoionized gas with the ionization parameter and the cloud density changing with the distance to the central ionizing source. See [Poutanen and Stern, 2010] for a detailed discussion on the γ-ray absorption within the BLR in the *Fermi* spectra. No general trend can be seen in the contemporaneous data sample. BPL and full BLR absorption scenarios seem to fit well the combined spectra of the blazars PKS 1424+240 and PKS 2155-304. A BPL (full BLR absorption) function is preferred over the PL for the blazars PKS 1424+240 and PKS 2155-304 with a significance of $\sim 5\sigma$ ($\sim 4.8\sigma$) and $\sim 12\sigma$ ($\sim 8.5\sigma$), respectively (see Figure 5.8). The χ^2/dof values of PL, BPL and APL fits are 32/9, 3.5/7, 5.3/7 for PKS 1424+240 and 148/8, 5.8/6, 71/6 for PKS 2155-304, respectively. BPL fits yield $\Delta\Gamma = 1.4$ (PKS 1424+240) and $\Delta\Gamma = 0.7$ (PKS 2155-304), both larger than what electron cooling would predict, which might indicate that an additional mechanism is at work. Both BPL and full BLR absorption scenarios provide a slight improvement in the MAGIC and VERITAS spectra of 3C 66A, albeit not significant. Similarly, for PKS 1222+21, BPL, H I single line and H I + He II double line absorptions slightly improve the fit over PL. In the case of RGB J0710+091 and 1ES 1218+304, we don't observe any preference over the power-law fit.

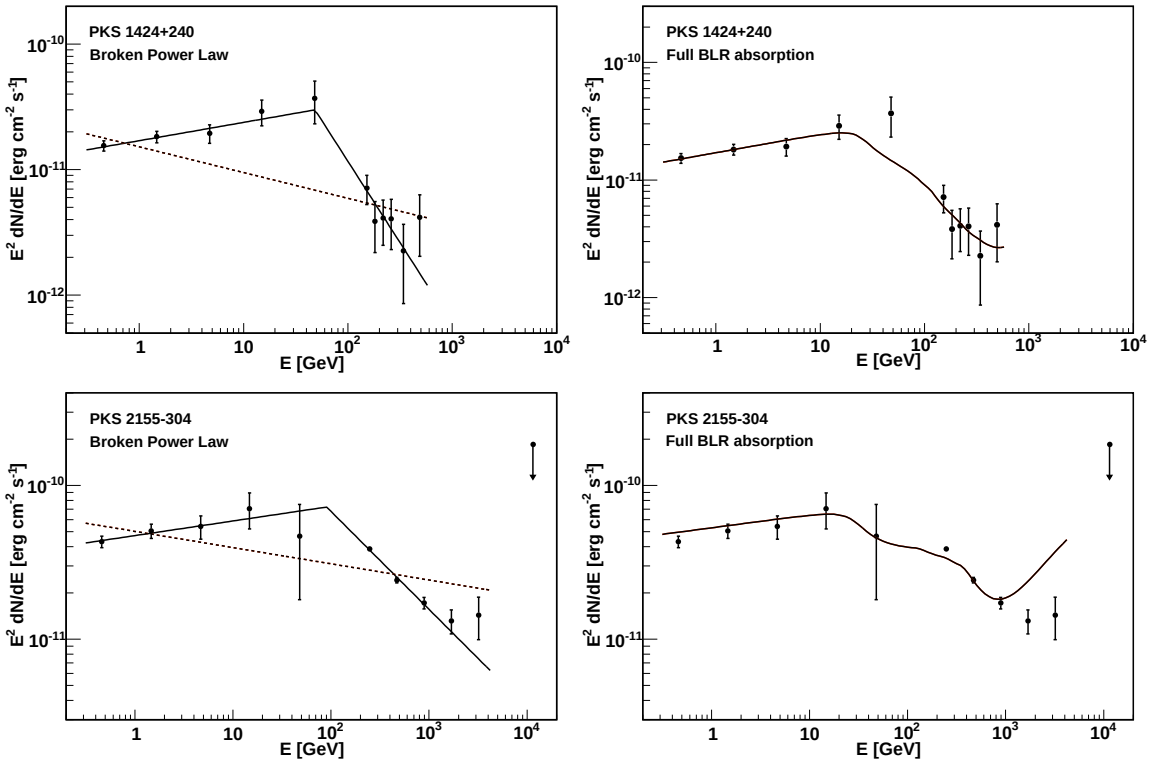

Figure 5.8: Contemporaneous GeV-TeV spectra with power-law (dashed lines), broken power-law (solid lines) and power-law with full-BLR-absorption fits. BPL and full BLR absorption scenarios seem to fit well the combined spectra of the blazars PKS 1424+240 and PKS 2155-304. A BPL (full BLR absorption) function is preferred over the PL for the blazars PKS 1424+240 and PKS 2155-304 with a significance of $\sim 5\sigma$ ($\sim 4.8\sigma$) and $\sim 12\sigma$ ($\sim 8.5\sigma$), respectively.

Part IV

Discussion and Conclusion

Several studies presented in this thesis have all the common goal of investigating and characterizing high-energy properties of VHE gamma-ray blazars. We discovered VHE gamma-ray emission from the HBL blazar RBS 0413 with the VERITAS instrument, for which we carried out a detailed spectral and temporal study. The integral flux for energies above 250 GeV is about 1% of the Crab Nebula flux, and the emission extending from 250 GeV to 1 TeV is well-described by a power law with a photon index $\Gamma = 3.18 \pm 0.68_{\rm stat} \pm 0.30_{\rm syst}$. We also tested three different emission models on the broad-band SED of this object using contemporaneous multi-wavelength data. All three models (SSC, SSC+EC, lepto-hadronic) describe the data successfully. For the SSC model, the relative partition between the magnetic field energy density and the kinetic luminosity of the relativistic particles is off from unity by about two orders of magnitude. On the other hand, an equality in relative partition is achieved in the case of the other two models, making them more favourable from an equipartition perspective. Based on the fact that the proton cooling time scale is too long to successfully explain a flare of intra-day scale, any future detection of such rapid variability would favor a purely leptonic scenario. On the other hand, any future finding favoring a lepto-hadronic mechanism would have implications for the origin of cosmic rays.

We studied blazar spectral properties with a focus on the GeV-TeV energy range for a sample of VHE blazars. In order to obtain a set of joint GeV-TeV blazar spectra, we analyzed the first 27 months of *Fermi* data for 26 VHE blazars and combined our results with archival VHE data. In cases where the *Fermi* data set does not overlap in time with the TeV observations but has enough statistics, we split the data into high and low flux states and assembled the best-matching subset with the corresponding TeV spectrum. We found that the peak frequency band of the inverse Compton component increases following the order FSRQ $\rightarrow$ LBL & IBL $\rightarrow$ HBL for different blazar subgroups. Thus, our results confirm the positive correlation between $\nu_{\rm syn}$ and $\nu_{\rm IC}$, the peak frequencies of the synchrotron and the inverse-Compton components of the broad-band SED, respectively. We note that *Fermi* spectra from different flux states for a given TeV blazar do not undergo a significant change in photon index. The variability amplitudes within our *Fermi* data set do not show an immediate correlation with the reported TeV variabilities for individual blazars. We find that in many cases a power law is insufficient to describe the GeV-TeV spectra

and a broken power law improves the fits, especially for non-HBL blazars, where the BLR emission may have an effect on the observed spectral shape. In some blazars we observe absorption-like spectral features. We presented seven quasi-simultaneous joint spectra, on which we tested possible absorption scenarios from the BLR. Even though the absorption seemed to describe well some of the observed spectra, no general pattern could be identified.

In addition to the studies mentioned above, the *Disp* reconstruction method was developed and implemented in the VERITAS data analysis package. The *Disp* method was not part of the studies presented in this work, but it was employed in observations of the galactic center, gamma-ray bursts, and the Nova V407 Cygni, a galactic GeV transient [Aliu and others, 2012b]. In addition, the *Disp* method was used in LZA blazar observations. Allowing for a much larger effective area and naturally raising the energy threshold, the *Disp* method helps improving the highest energy part of blazar spectral studies. Improved energy resolution in the high-energy tail of the blazar spectra would contribute to EBL measurements. Moreover, expanding the energy range of blazar spectra would allow for more constraining upper limits for LIV studies.

Part V

Bibliography

Bibliography

[Abdo and others, 2009] A. A. Abdo et al. Fermi observations of tev-selected active galactic nuclei. *The Astrophysical Journal*, 707(2):1310–1333, December 2009.

[Abdo and others, 2010a] A. A. Abdo et al. The first catalog of active galactic nuclei detected by the fermi large area telescope. *The Astrophysical Journal*, 715(1):429–457, May 2010.

[Abdo and others, 2010b] A. A. Abdo et al. The spectral energy distribution of fermi bright blazars. *The Astrophysical Journal*, 716(1):30–70, June 2010.

[Abdo and others, 2011] A. A. Abdo et al. Multi-wavelength observations of the flaring gamma-ray blazar 3c 66a in 2008 october. *The Astrophysical Journal*, 726(1):14, January 2011.

[Abramowski and others, 2010a] A. Abramowski et al. Multi-wavelength observations of h 2356-309. *Astronomy and Astrophysics*, 516:A56, June 2010.

[Abramowski and others, 2010b] A. Abramowski et al. Vhe gamma-ray emission of pks 2155-304: Spectral and temporal variability. *Astronomy and Astrophysics*, 520:16, September 2010.

[Acciari and others, 2008] V. A. Acciari et al. Veritas discovery of > 200 gev gamma-ray emission from the intermediate-frequency-peaked bl lacertae object w comae. *The Astrophysical Journal Letters*, 684(2):L73–L77, September 2008.

[Acciari and others, 2009a] V. A. Acciari et al. Discovery of very high energy gamma-ray radiation from the bl lac 1es 0806+524. *The Astrophysical Journal Letters*, 690(2):L126–L129, January 2009.

[Acciari and others, 2009b] V. A. Acciari et al. Multiwavelength observations of a tev-flare from w comae. *The Astrophysical Journal*, 707(1):612–620, December 2009.

[Acciari and others, 2009c] V. A. Acciari et al. Veritas observations of a very high energy gamma-ray flare from the blazar 3c 66a. *The Astrophysical Journal Letters*, 693(2):L104–L108, March 2009.

[Acciari and others, 2009d] V. A. Acciari et al. Veritas observations of the bl lac object 1es 1218+304. *The Astrophysical Journal*, 695(2):1370–1375, April 2009.

[Acciari and others, 2010a] V. A. Acciari et al. The discovery of gamma ray emission from the blazar rgb j0710+591. *The Astrophysical Journal Letters*, 715(1):L49–L55, May 2010.

[Acciari and others, 2010b] V. A. Acciari et al. Discovery of variability in the very high energy gamma-ray emission of 1es 1218+304 with veritas. *The Astrophysical Journal Letters*, 709(2):L163–L167, February 2010.

[Acciari and others, 2010c] V. A. Acciari et al. Discovery of very-high-energy gamma rays from pks 1424+240 and multiwavelength constraints on its redshift. *The Astrophysical Journal Letters*, 708(2):L100–L106, January 2010.

[Acero and others, 2010] F. Acero et al. Pks 2005-489 at vhe: Four years of monitoring with hess and simultaneous multi-wavelength observations. *Astronomy and Astrophysics*, 511:13, February 2010.

[Actis and others, 2011] M. Actis et al. Design concepts for the cherenkov telescope array cta: an advanced facility for ground-based high-energy gamma-ray astronomy. *Experimental Astronomy*, 32(3):193–316, December 2011.

[Aharonian and others, 2007a] F. Aharonian et al. Detection of vhe gamma-ray emission from the distant blazar 1es1101-232 with hess and broadband characterisation. *Astronomy and Astrophysics*, 470(2):475–489, August 2007.

[Aharonian and others, 2007b] F. Aharonian et al. Discovery of vhe gamma rays from the distant bl lacertae 1es 0347-121. *Astronomy and Astrophysics*, 473(3):L25–L28, October 2007.

[Aharonian and others, 2007c] F. Aharonian et al. An exceptional very high energy gamma-ray flare of pks 2155-304. *The Astrophysical Journal Letters*, 664(2):L71–L74, August 2007.

[Aharonian and others, 2007d] F. Aharonian et al. New constraints on the mid-ir ebl from the hess discovery of vhe gamma rays from 1es 0229+200. *Astronomy and Astrophysics*, 475(2):L9–L13, November 2007.

[Aharonian and others, 2008a] F. Aharonian et al. Discovery of vhe gamma rays from the high-frequency-peaked bl lacertae object rgb j0152+017. *Astronomy and Astrophysics*, 481(3):L103–L107, April 2008.

[Aharonian and others, 2008b] F. Aharonian et al. High energy astrophysics with ground-based gamma ray detectors. *Reports on Progress in Physics*, 71(9):096901, September 2008.

[Aharonian and others, 2009] F. Aharonian et al. Simultaneous observations of pks 2155-304 with hess, fermi, rxte, and atom: Spectral energy distributions and variability in a low state. *The Astrophysical Journal Letters*, 696(2):L150–L155, May 2009.

[Aharonian and others, 2010] F. Aharonian et al. Discovery of vhe gamma rays from the bl lacertae object pks 0548-322. *Astronomy and Astrophysics*, 521:6, October 2010.

[Aiso and others, 1997] S. Aiso et al. The telescope array project. In *Proceedings of the 25th International Cosmic Ray Conference, Durban, South Africa*, 1997.

[Albert and others, 2006] J. Albert et al. Discovery of very high energy -rays from markarian 180 triggered by an optical outburst. *The Astrophysical Journal*, 648(2):L105–L108, September 2006.

[Albert and others, 2007a] J. Albert et al. Discovery of very high energy gamm rays from 1es 1011+496 at z = 0.212. *The Astrophysical Journal Letters*, 667(1):L21–L24, September 2007.

[Albert and others, 2007b] J. Albert et al. Discovery of very high energy gamma-ray emission from the low-frequency-peaked bl lacertae object bl lacertae. *The Astrophysical Journal Letters*, 666(1):L17–L20, September 2007.

[Albert and others, 2007c] J. Albert et al. Observation of very high energy gamma rays from the agn 1es 2344+514 in a low emission state with the magic telescope. *The Astrophysical Journal*, 662(2):892–899, June 2007.

[Albert and others, 2007d] J. Albert et al. Observations of markarian 421 with the magic telescope. *The Astrophysical Journal*, 663(1):125–138, July 2007.

[Albert and others, 2007e] J. Albert et al. Variable very high energy gamma-ray emission from markarian 501. *The Astrophysical Journal*, 669(2):862–883, November 2007.

[Albert and others, 2008a] J. Albert et al. Probing quantum gravity using photons from a flare of the active galactic nucleus markarian 501 observed by the magic telescope. *Physics Letters B*, 668(4):253–257, October 2008.

[Albert and others, 2008b] J. Albert et al. Systematic search for vhe gamma-ray emission from x-ray-bright high-frequency bl lac objects. *The Astrophysical Journal*, 681(2):944–953, July 2008.

[Albert and others, 2008c] J. Albert et al. Very-high-energy gamma rays from a distant quasar: How transparent is the universe? *Science*, 320(5884):1752, June 2008.

[Aleksić and others, 2010] J. Aleksić et al. Simultaneous multi-frequency observation of the unknown redshift blazar pg 1553+113 in march-april 2008. *Astronomy and Astrophysics*, 515:5, June 2010.

[Aleksić and others, 2011a] J. Aleksić et al. Magic discovery of very high energy emission from the fsrq pks 1222+21. *The Astrophysical Journal Letters*, 730(1):6, March 2011.

[Aleksić and others, 2011b] J. Aleksić et al. Observations of the blazar 3c 66a with the magic telescopes in stereoscopic mode. *The Astrophysical Journal*, 726(2):5, January 2011.

[Aliu and others, 2012a] E. Aliu et al. Discovery of high-energy and very high energy gamma-ray emission from the blazar rbs 0413. *The Astrophysical Journal*, 750(2):94, May 2012.

[Aliu and others, 2012b] E. Aliu et al. Veritas observations of the nova in v407 cygni. *The Astrophysical Journal*, 754(1):id.77, July 2012.

[Anderhub and others, 2009a] H. Anderhub et al. Discovery of very high energy gamma rays from the blazar s5 0716+714. *The Astrophysical Journal Letters*, 704(2):L129–L133, October 2009.

[Anderhub and others, 2009b] H. Anderhub et al. Simultaneous multiwavelength observation of mkn 501 in a low state in 2006. *The Astrophysical Journal*, 705(2):1624–1631, November 2009.

[Antón and Browne, 2005] S. Antón and I. W. A. Browne. The recognition of blazars and the blazar spectral sequence. *Monthly Notices of the Royal Astronomical Society*, 356(1):225–231, January 2005.

[Arlen and others, 2013] T. Arlen et al. Rapid tev gamma-ray flaring of bl lacertae. *The Astrophysical Journal*, 762(2):13, January 2013.

[Armstrong and others, 1999] P. Armstrong et al. The university of durham mark 6 gamma ray telescope. *Experimental Astronomy*, 9(2):51–80, June 1999.

[Atkins and others, 2004] R. Atkins et al. Tev gamma-ray survey of the northern hemisphere sky using the milagro observatory. *The Astrophysical Journal*, 608(2):680–685, June 2004.

[Atwood and others, 2009] W. B. Atwood et al. The large area telescope on the fermi gamma-ray space telescope mission. *The Astrophysical Journal*, 697(2):1071–1102, June 2009.

[Beilicke and others, 2012] M. Beilicke et al. The galactic center region imaged by veritas from 2010-2012. *5th International Meeting on High Energy Gamma-Ray Astronomy. AIP Conference Proceedings*, 1505:462–465, December 2012.

[Beilicke, 2008] M. Beilicke. Camera acceptance and background estimation. 2008.

[Beilicke, 2010] M. Beilicke. Shower reconstruction at large zenith angles (lza). 2010.

[Böttcher and others, 2012] M. Böttcher et al. *Relativistic Jets from Active Galactic Nuclei*. Wiley-VCH, 2012.

[Böttcher, 2010] M. Böttcher. Models for the spectral energy distributions and variability of blazars. *Invited Review at "Fermi Meets Jansky", Bonn, Germany, June 21 - 23, 2010; In "Fermi Meets Jansky - AGN at Radio and Gamma-Rays", Eds.: Savolainen, T., Ros, E., Porcas, R. W., and Zensus, J. A.*, page 41, June 2010.

[Cash, 1979] W. Cash. Parameter estimation in astronomy through application of the likelihood ratio. *The Astrophysical Journal*, 228(1):939–947, March 1979.

[Çelik, 2008] Ö. Çelik. *Crab Nebula and Pulsar with VERITAS*. PhD thesis, University of California Los Angeles, 2008.

[Chiang and Böttcher, 2002] J. Chiang and M. Böttcher. Synchrotron and synchrotron self-compton spectral signatures and blazar emission models. *The Astrophysical Journal*, 564(1):92–96, January 2002.

[Costamante and others, 2011] L. Costamante et al. Challenges to the standard models from gamma-ray spectra of blazars at the two ends of the blazar sequence. In *Proceedings of the 3rd Fermi Symposium, Rome, Italy, eConf C110509*, 2011.

[Daniel and others, 2007] M. K. Daniel et al. The veritas standard data analysis. In *The 30th International Cosmic Ray Conference, Mérida, México*, 2007.

[Davies and Cotton, 1957] C. M. Davies and E. S. Cotton. Design of the quartermaster solar furnace. *The Journal of Solar Energy*, 1(2, 3):16–22, April, July 1957.

[Dermer and Menon, 2009] C. Dermer and M Menon. *High Energy Radiation from Black Holes: Gamma Rays, Cosmic Rays, and Neutrinos*. Princeton University Press, 2009.

[Domínguez and others, 2011] A. Domínguez et al. Extragalactic background light inferred from aegis galaxy-sed-type fractions. *Monthly Notices of the Royal Astronomical Society*, 410(4):2556–2578, February 2011.

[Errando and others, 2011] M. Errando et al. Automated analysis of fermi-lat data to trigger ground-based gamma-ray observations. In *Proceedings of the 32nd International Cosmic Ray Conference, Beijing, China*, 2011.

[Finke and others, 2010a] J. D. Finke et al. Modeling the extragalactic background light from stars and dust. *The Astrophysical Journal*, 712(1):238–249, March 2010.

[Finke and others, 2010b] J. D. Finke et al. Modeling the extragalactic background light from stars and dust. *The Astrophysical Journal*, 712(1):238–249, March 2010.

[Fossati and others, 1998] G. Fossati et al. A unifying view of the spectral energy distributions of blazars. *Monthly Notices of the Royal Astronomical Society: Letters*, 299(2):433–448, September 1998.

[Fossati and others, 2008] G. Fossati et al. Multiwavelength observations of markarian 421 in 2001 march: An unprecedented view on the x-ray/tev correlated variability. *The Astrophysical Journal*, 677(2):906–925, April 2008.

[Franceschini and others, 2008] A. Franceschini et al. Extragalactic optical-infrared background radiation, its time evolution and the cosmic photon-photon opacity. *Astronomy and Astrophysics*, 487(3):837–852, September 2008.

[Furniss and others, 2013] A. Furniss et al. The firm redshift lower limit of the most distant tev-detected blazar pks 1424+240. *The Astrophysical Journal Letters*, 768(2):L31, May 2013.

[Gehrels and others, 2004] N. Gehrels et al. The swift gamma-ray burst mission. *The Astronomical Journal*, 611(2):1005–1020, August 2004.

[Georganopoulos and others, 2010] M. Georganopoulos et al. A method for setting upper limits to the extragalactic background light with fermi-lat and tev observations of blazars. *The Astrophysical Journal*, 714(1):L157–L161, May 2010.

[Ghisellini and others, 1998] G. Ghisellini et al. A theoretical unifying scheme for gamma-ray bright blazars. *Monthly Notices of the Royal Astronomical Society*, 301(2):451–468, December 1998.

[Ghisellini and others, 2009] G. Ghisellini et al. The fermi blazars' divide. *Monthly Notices of the Royal Astronomical Society*, 396(1):L105–L109, May 2009.

[Gioia and others, 1984] I. M. Gioia et al. The medium sensitivity survey - a new sample of x-ray sources with optical identifications and the revised extragalactic log n-log s. *The Astrophysical Journal*, 283(1):495–511, August 1984.

[Griffin and others, 2011] S. Griffin et al. Searching for fast optical transients using veritas cherenkov telescopes. In *Proceedings of the 32nd International Cosmic Ray Conference, Beijing, China*, 2011.

[Hanna and others, 2002] D. S. Hanna et al. The stacee-32 ground based gamma-ray detector. *Nuclear Instruments and Methods in Physics Research Section A*, 491(1-2):126–151, September 2002.

[Hillas, 1985] A. M. Hillas. Cerenkov light images of eas produced by primary gamma. *Proceedings of the 19th International Cosmic Ray Conference*, 3:445–448, 1985.

[Hofmann and others, 1999] W. Hofmann et al. Comparison of techniques to reconstruct vhe gamma-ray showers from multiple stereoscopic cherenkov images. *Astroparticle Physics*, 12(3):135–143, November 1999.

[Horns and others, 2004] D. Horns et al. Tev observations of h1426+428 with hegra. *New Astronomy Reviews*, 48(5-6):387–390, April 2004.

[Hovatta and others, 2009] T. Hovatta et al. Doppler factors, lorentz factors and viewing angles for quasars, bl lacertae objects and radio galaxies. *Astronomy and Astrophysics*, 494(2):527–537, February 2009.

[Huan and others, 2011] H. Huan et al. A new model for gamma-ray cascades in extragalactic magnetic fields. *The Astrophysical Journal Letters*, 735(2):L28, July 2011.

[Katarzyński, 2011] K. Katarzyński. Correlation between x-ray and gamma-ray emission in tev blazars. *Memorie della Societa Astronomica Italiana*, 82:168, 2011.

[Kellermann and others, 1989] K. I. Kellermann et al. Vla observations of objects in the palomar bright quasar survey. *Astronomical Journal*, 98:1195–1207, October 1989.

[Kembhavi and Narlikar, 1999] A. K. Kembhavi and J. V. Narlikar. *Quasars and Active Galactic Nuclei: An Introduction*. Cambrigde University Press, 1999.

[Kieda, 2011] D. Kieda. Status of the veritas gamma-ray telescope upgrade. In *American Physical Society, APS April Meeting 2011, April 30-May 3, 2011, http://meetings.aps.org/link/BAPS.2011.APR.B11.3*, 2011.

[Kranich and Stark, 2003] D. Kranich and L. S. Stark. An new method to determine the arrival direction of individual air showers with a single air cherenkov telescope. *Proceedings of the 28th International Cosmic Ray Conference*, page 3023, July 2003.

[Krawczynski and others, 2004] H. Krawczynski et al. Multiwavelength observations of strong flares from the tev blazar 1es 1959+650. *The Astrophysical Journal*, 601(1):151–164, January 2004.

[Lanzetta and others, 1993] K. M. Lanzetta et al. Ultraviolet spectra of qsos, bl lacertae objects, and seyfert galaxies. *Astrophysical Journal Supplement Series*, 84(2):109–184, February 1993.

[Lefa and others, 2011] E. Lefa et al. Formation of very hard gamma-ray spectra of blazars in leptonic models. *The Astrophysical Journal*, 740(2):9, October 2011.

[Lessard and others, 2001] R. W. Lessard et al. A new analysis method for reconstructing the arrival direction of tev gamma rays using a single imaging atmospheric cherenkov telescope. *Astroparticle Physics*, 15(1):1–18, March 2001.

[Li and Ma, 1983] T.-P. Li and Y.-Q. Ma. Analysis methods for results in gamma-ray astronomy. *The Astrophysical Journal*, 272(1):317–324, September 1983.

[Maier and others, 2007] G. Maier et al. Monte carlo studies of the veritas array of cherenkov telescopes. In *The 30th International Cosmic Ray Conference, Mérida, México*, 2007.

[Mannheim and Biermann, 1989] K. Mannheim and P. L. Biermann. Photomeson production in active galactic nuclei. *Astronomy and Astrophysics*, 221(2):211–220, January 1989.

[Maraschi and others, 1992] L. Maraschi et al. A jet model for the gamma-ray emitting blazar 3c 279. *The Astrophysical Journal*, 397(1):L5–L9, September 1992.

[Mattox and others, 1996] J. R. Mattox et al. The likelihood analysis of egret data. *The Astrophysical Journal*, 461:396–407, April 1996.

[Mazin and F., 2007] D. Mazin and Goebel F. Break in the very high energy spectrum of pg 1553+113: New upper limit on its redshift? *The Astrophysical Journal Letters*, 655(1):13–16, January 2007.

[McCann and others, 2010] A. McCann et al. A new mirror alignment system for the veritas telescopes. *Astroparticle Physics*, 32(6):325–329, January 2010.

[Miller and others, 1978] J. S. Miller et al. Optical spectra of bl lacertae objects. In *Pittsburgh Conference on BL Lac Objects, Pittsburgh, Pa., April 24-26,1978, Proceedings. (A79-30026 11-90) Pittsburgh, Pa.*, 1978.

[Mücke and Protheroe, 2001] A. Mücke and R. J. Protheroe. A proton synchrotron blazar model for flaring in markarian 501. *Astroparticle Physics*, 15(1):121–136, March 2001.

[Mullaney and others, 2011] J. R. Mullaney et al. Defining the intrinsic agn infrared spectral energy distribution and measuring its contribution to the infrared output of composite galaxies. *Monthly Notices of the Royal Astronomical Society*, 414(2):10821110, June 2011.

[Murase and others, 2012] K. Murase et al. Blazars as ultra-high-energy cosmic-ray sources: Implications for tev gamma-ray observations. *The Astrophysical Journal*, 749(1):15, April 2012.

[Nieppola and others, 2006] E. Nieppola et al. Spectral energy distributions of a large sample of bl lacertae objects. *Astronomy and Astrophysics*, 445(2):441–450, January 2006.

[Nieppola and others, 2008] E. Nieppola et al. Blazar sequence - an artefact of doppler boosting. *Astronomy and Astrophysics*, 488(3):867–872, September 2008.

[Nolan and others, 2012] P. L. Nolan et al. Fermi large area telescope second source catalog. *The Astrophysical Journal Supplement*, 199(2):46, April 2012.

[Ong, 1998] R. A. Ong. Very high-energy gamma-ray astronomy. *Physics Reports*, 305(3-4):93–202, November 1998.

[Orr and others, 2011] M. R. Orr et al. Strong new constraints on the extragalactic background light in the near- to mid-infrared. *The Astrophysical Journal*, 733(2):77, June 2011.

[Otte and others, 2011] N. Otte et al. The upgrade of veritas with high efficiency photomultipliers. In *Proceedings of the 32nd International Cosmic Ray Conference, Beijing, China*, 2011.

[Padovani and Giommi, 1995] P. Padovani and P. Giommi. The connection between x-ray- and radio-selected bl lacertae objects. *The Astrophysical Journal*, 444(2):567–581, May 1995.

[Paré and others, 2002] E. Paré et al. Celeste: An atmospheric cherenkov telescope for high energy gamma astrophysics. *Nuclear Instruments and Methods in Physics Research Section A*, 490(1-2):71–89, September 2002.

[Perkins and others, 2009] J. S. Perkins et al. Veritas telescope 1 relocation: Details and improvements. In *Proceedings of the 2nd Fermi Symposium, Washington, D.C., USA*, 2009.

[Peterson, 1997] B. M. Peterson. *An Introduction to Active Galactic Nuclei*. Cambridge University Press, 1997.

[Poutanen and Stern, 2010] J. Poutanen and B. Stern. Gev breaks in blazars as a result of gamma-ray absorption within the broad-line region. *The Astrophysical Journal*, 717(2):L118–L121, July 2010.

[Prandini and others, 2011] E. Prandini et al. Constraining blazars distances with combined gev and tev data. In *Proceedings of the 3rd Fermi Symposium, Rome, Italy, eConf C110509*, 2011.

[Pühlhofer and others, 2003] G. Pühlhofer et al. The technical performance of the hegra system of imaging air cherenkov telescopes. *Astroparticle Physics*, 20(3):267–291, December 2003.

[Reinthal and others, 2012] R. Reinthal et al. Connection between optical and vhe gamma-ray emission in blazar jets. *Journal of Physics: Conference Series*, 355(1):2013, March 2012.

[Schroedter and others, 2009] M. Schroedter et al. A topological trigger system for imaging atmospheric-cherenkov telescopes. In *Proceedings of the 31st International Cosmic Ray Conference, Łódź, Poland*, 2009.

[Schwinger and others, 1998] J. Schwinger et al. *Classical Electrodynamics*. Westview Press, 1998.

[Senturk and others, 2011] G. D. Senturk et al. The disp method for analyzing large zenith angle gamma-ray data. In *Proceedings of the 32nd International Cosmic Ray Conference, Beijing, China*, 2011.

[Senturk and others, 2013] G. D. Senturk et al. Gamma-ray observational properties of tev-detected blazars. *The Astrophysical Journal*, 764(2):id. 119, February 2013.

[Soldi and others, 2008] S. Soldi et al. The multiwavelength variability of 3c 273. *Astronomy and Astrophysics*, 486(2):411–425, August 2008.

[Stocke and others, 1985] J. T. Stocke et al. Optical and radio properties of x-ray selected bl lacertae objects. *The Astrophysical Journal*, 298(1):619–629, November 1985.

[Stocke and others, 1989] J. T. Stocke et al. The optical and radio properties of x-ray selected bl-lacertae objects. In *BL Lac Objects. Proceedings of a workshop held in Como, Italy, September 20-23, 1988.*, 1989.

[Stocke and others, 1990] J. T. Stocke et al. No evidence for radio-quiet bl lacertae objects. *The Astrophysical Journal*, 348(1):141–146, January 1990.

[Tagliaferri and others, 2008] G. Tagliaferri et al. Simultaneous multiwavelength observations of the blazar 1es 1959+650 at a low tev flux. *The Astrophysical Journal*, 679(2):1029–1039, June 2008.

[Tanihata and others, 2003] C. Tanihata et al. Implications of variability patterns observed in tev blazars on the structure of the inner jet. *The Astrophysical Journal*, 584(1):153–163, February 2003.

[Thompson and others, 1993] D. J. Thompson et al. Calibration of the energetic gamma-ray experiment telescope (egret) for the compton gamma-ray observatory. *The Astrophysical Journal Supplement Series*, 86(2):629–656, June 1993.

[Tueller and others, 2010] J. Tueller et al. The 22 month swift-bat all-sky hard x-ray survey. *The Astrophysical Journal Supplement*, 186(2):378–405, February 2010.

[Urry and Padovani, 1995] M. Urry and P. Padovani. Unified schemes for radio-loud active galactic nuclei. *Publications of the Astronomical Society of the Pacific*, 107(715):803–845, September 1995.

[Vaughan and others, 2003] S. Vaughan et al. On characterizing the variability properties of x-ray light curves from active galaxies. *Monthly Notices of the Royal Astronomical Society*, 345(4):1271–1284, November 2003.

[Veres and others, 2010] P. Veres et al. Physical parameters of a relativistic jet at very high redshift: the case of the blazar j1430+4204. *Astronomy and Astrophysics*, 521:A6, October 2010.

[Weekes and others, 1989] T. C. Weekes et al. Observation of tev gamma rays from the crab nebula using the atmospheric cerenkov imaging technique. *The Astrophysical Journal*, 342(1):379–395, July 1989.

[Weekes, 2003] T. C. Weekes. *Very High Energy Gamma-Ray Astronomy*. CRC Press, 2003.

[Weinstein and others, 2007] A. Weinstein et al. The veritas trigger system. In *Proceedings of the 30th International Cosmic Ray Conference, Mérida, México*, 2007.

[Willott and others, 2008] C. J. Willott et al. Photometric calibration of the swift ultraviolet/optical telescope. *Monthly Notices of the Royal Astronomical Society*, 383(2):627–645, January 2008.

[Willott and others, 2010] C. J. Willott et al. The canada-france high-z quasar survey: Nine new quasars and the luminosity function at redshift 6. *The Astronomical Journal*, 139(3):906–918, March 2010.

[Wilson and Colbert, 1995] A. S. Wilson and E. J. M. Colbert. The difference between radio-loud and radio-quiet active galaxies. *The Astrophysical Journal*, 438(1):62–71, January 1995.

[Xiang and Dai, 2007] Y. Xiang and B.-Z. Dai. A possible estimate of the doppler factors for blazars. *Publications of the Astronomical Society of Japan*, 59(6):1061–1069, December 2007.

[Zhang and others, 2012] J. Zhang et al. Radiation mechanisms and physical properties of gev-tev bl lac objects. *The Astrophysical Journal*, 752(2):157, June 2012.

Part VI

Appendices

Appendix A

The *Disp* Method

The *Disp* method is a direction reconstruction algorithm that has been used mostly in single telescope observations (e.g. [Lessard and others, 2001; Kranich and Stark, 2003]). The introduction of a new generation of ground-based gamma-ray instruments operating in array mode with multiple telescopes allowed for new and more accurate techniques for direction reconstruction, that made use of stereo image information. However, due to a larger (on average) impact parameter of the air showers with respect to the center of the IACT array and projection effects, these geometrical reconstruction techniques do not perform well in the case of large zenith angle (LZA) observations. The *Disp* method compensates for this loss in quality of the angular reconstruction, and thus improves angular resolution of stereo shower images in the case of LZA data. Here we present the implementation of the *Disp* method in the VERITAS data analysis package VEGAS. This work has been published in [Senturk and others, 2011]. With the *Disp* method improvement in the analysis chain, VERITAS has been able to observe the galactic center and detect a strong signal. Other LZA targets include gamma-ray bursts, which VERITAS observes at zenith angles up to 70°. In addition, LZA observations have the advantage of increased effecive areas, combined with a natural selection of high energy events, since relatively more distant air showers are observed (see Figure A.1), which allows for a better sensitivity in high-energy studies.

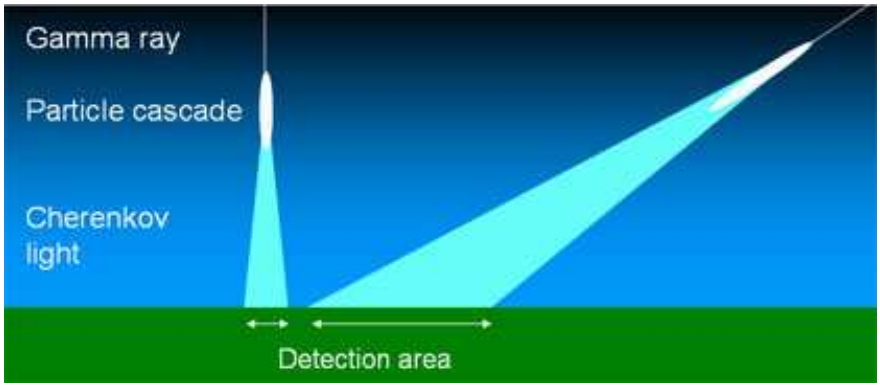

Figure A.1: The effective area increases in the case of LZA observations, while selecting the air showers that are bright enough to be detected and analyzed, despite the larger distance. Since the energy threashold and the effective area are both raised, a sensitive study of high energy spectra is possible. Figure from the HESS website.

A.1 Description of the algorithm

A description of the VEGAS analysis steps prior to direction reconstruction (calibration, image cleaning and image parameterization) can be found in 2.4. At the latter step, a second moment parameterization with *Hillas* parameters is performed on each shower image [Hillas, 1985]. See Figure A.2b for a detailed representation of relevant *Hillas* parameters *disp*, *width* and *length*. *Disp* is the segment of the major axis that lies between the image centroid and the projection of the real source location onto the axis. Another important image parameter is *size*, defined as the total integrated charge in image pixels, representing a measure of brightness for the image. Figure A.2a shows the stereoscopic image of an air shower after parameterization, and the calculated arrival direction using the geometrical (hereafter *geo*) technique. The reconstructed direction in the *geo* method is the point with the smallest total distance from each major axis (see Figure A.2a), and it works quite well for low to moderate zenith angles. The error associated with the *geo* calculation is inversely related to the angles between the major axes. In other words, images that have major axis alignments close to parallel with respect to one another (see Figure A.2c) result in large errors in direction reconstruction. Parallel images more often occur in the case of LZA data, since in this case the air showers tend to land outside the array.

The *Disp* method implemented in VEGAS makes use of multidimensional lookup tables (here-

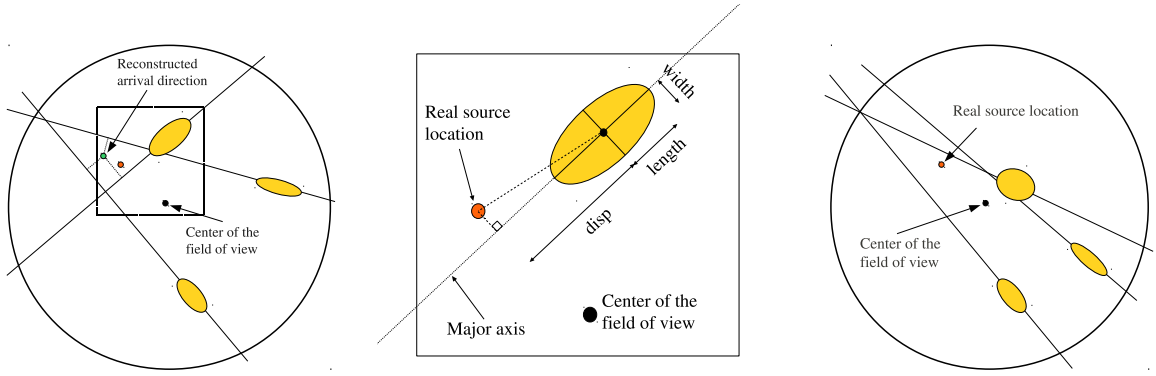

Figure A.2: a) Representation of an air shower stereo image, seen by three different telescopes. b) Detail from (a), *Hillas* parameters that are used in the *Disp* algorithm. c) Stereo images for LZA events tend to have mostly parallel major axes with respect to each other. In all three figures, reconstructed and real source locations are represented by green and red dots, respectively.

after 'disp tables') that contain the image information coming from Monte Carlo (MC) simulated air shower data. For each simulated shower image, the disp table stores the *Hillas* parameters *size*, *width*, *length* and *disp*. These quantities are related to each other by the following geometrical argument: the projected images of air showers that fall near the source location on the camera plane look circular (the shower orientation is perpendicular to the optical plane), and they become flatter as they move away from it (the shower orientation is slightly tilted with respect to the camera plane). For a visualisation of this argument, compare shower images in Figure A.2, right. Therefore, *disp* should increase with increasing image ellipticity, which can be quantitatively described by *width* and *length* parameters. The dependence on *size* has been verified from parameter distribution plots. Additional dimensions present in the disp tables are zenith and azimuth angles, NSB noise level and telescope ID.

The *disp* reconstruction algorithm works in the following way: for a given shower image, *size*, *width* and *length* parameters are retrieved and the corresponding *disp* is read from the disp table. This tells us how far the arrival direction is from the image centroid along the major axis, but it does not tell at which side of the ellipse it should be located, an issue known as the head-tail ambiguity [Hofmann and others, 1999]. To address this problem, the closest cluster of points is picked, one coming from each shower image (see Figure A.3). In this way, the arrival direction

is estimated for each telescope image and a weighted average is calculated. The novelty of this implementation is that the *width* and *length* parameters are being used as separate table dimensions, and not as one combined *width*/*length* parameter, as was formerly used for this type of analysis [Hofmann and others, 1999]. Separating *width* and *length* yields better angular resolution for LZA data.

A.2 Application and Results

A.2.1 LZA Crab Nebula observations

The *disp* method has been tested on MC simulations and LZA Crab data. A study on the zenith angle dependence of angular resolution (68% containment radius) comparing the two reconstruction methods is shown in Figure A.4, illustrating the improvement that we see with the *disp* method. A significant improvement in the signal to noise ratio for data with zenith angles starting around 45° is obtained. We measure an increase in significance of ∼20% for a Crab-Nebula-like source and ∼30% for a source having 1% Crab Nebula strength. For small zenith angles, the geometrical method has the best angular resolution.

A.2.2 Galactic Center Analysis

VERITAS observed the galactic center at the position of Sgr A* for ∼15 hours with 62° average zenith angle, from April to June 2010. This is the first science application of the *Disp* method with VERITAS. The detection significance is more than 11 standard deviations [Beilicke and others, 2012]. Figure A.5 shows the skymap for the VERITAS detection.

A.3 Further Tests and Improvements

An important parameter to consider in the direction reconstruction study is energy. We see that the reconstruction of the *disp* method fails for energies larger than ∼ 1 TeV, particularly for small zenith angles (Section A.3.1). In addition, we compared the *geo* and *disp* methods in large wobble

offset data analysis, motivated by the fact that the shower images on the camera plane would be similar to the LZA ones (Section A.3.2). We have also checked the core distance dependence of both methods and applied a *loss* cut to study the performance of the *disp* method in case of truncated shower images (Section A.3.3). Finally, in Section A.3.4, we summarize the effects of using the *distance* parameter as a disp table dimension.

A.3.1 Performance of *Disp* as a function of energy

We have tested the point spread function (PSF) as a function of the energy for zenith angles ranging from 0° to 65° (See Figure A.6). The PSF is defined as the 68% containment of the θ^2 parameter, where θ is the angular distance between the putative source location and the reconstructed direction.

As a general pattern, the *disp* method performs poorly for high energies in the case of small zenith angles. For zenith = 0°, *disp* and *geo* are comparable at low energies. But then the *disp* PSF undergoes a steep increase. The crossing energy is around 700 GeV for 0° and goes up to several tens of TeV as zenith goes to 65°, at which point the *disp* outperforms the *geo* for all energies. See Figure A.6 for PSF versus energy at zenith angles of 20°, 45°, 55° and 65°.

In an attempt to understand better the energy dependence of the reconstruction performances from both methods, we look at the PSF vs. energy plots for different telescope combinations and for small (20°) and large (55°) zenith angles (Figure A.7,A.8 and A.9).

As expected, the *disp* method performs better at large zenith values. In all cases, the angular resolution improves with increasing number of telescopes. The *disp* method is expected to outperform the *geo* method for 2-telescope shower events (that mostly land outside the array and thus have parallel images), but this does not seem to be the case at large energies. The issue is still under investigation. Table binning in particular stands out as an area that has not yet been optimized.

A.3.2 Off-axis Reconstruction

In large wobble offset data analyzed by VEGAS, the PSF appears to be asymmetric, elongated along the wobble offset direction. This could stem from a similar effect as in the case of the large zenith angle data, where shower images tend to be parallel on the camera plane, increasing the

error associated with the geometrical reconstruction. To test this hypothesis, we have compared the *geo* and *disp* methods for increasing wobble offset values from 0° to 2° for small (20°) zenith angles. No improvement is seen with the *disp* method, and contrary to what we originally expected, the *geo* method seems to outperform the *disp* at large wobble offsets, as shown in Figure A.10. In addition, an interesting observation is that the two methods yield identical results below 1 TeV and the *disp* PSF worsens at higher energies, for all offset values.

A.3.3 Effect of the *loss* cut

To understand the events that are reconstructed with large θ^2 values, we applied a *loss* cut ($loss < 0.1$) with the *disp* method. *Loss* is the fraction of the charge deposited in the outer pixels of the camera, which may be considered a proxy for how significantly truncation at the edge of the field of view affects an image. Thus, we excluded events with more than 10% of the total charge located near the rim of the camera. This eliminates a significant number of outliers for all energies (see Figure A.11). For zenith=20°(55°), the fraction of events with $\theta^2 > 0.2$ drops from 8%(11%) to 2%(6%). We also see that the loss cut has a similar effect in the case of core distance reconstruction. To conclude, an important portion of the misreconstructed events in the *disp* method consists of truncated images, for which the current Hillas parameterization method does not work well. On the other hand, the newly implemented HFit method, which uses a two-dimensional gaussian fit to parameterize each image, is more reliable in the case of truncated events, and so is promising for the performance of the *disp* method.

A.3.4 Effect of the *distance* dimension

The *distance* parameter is defined as the angular distance from the image centroid to the center on the camera plane. Since we mostly run 0.5° MC files for producing disp tables, the *distance* and the *disp* turn out to be correlated. Consequently, using *distance* as a disp table dimension introduces bias. This is manifested in the θ^2 plots as increased background rate within the signal region. It is still possible that the *distance* parameter might prove to be a useful and bias-free table dimension if the disp tables are generated using a complete set of MC files, including all wobble offset values.

A.4 Combining *Geo* and *Disp*

Based on our results, *geo* and *disp* methods perform differently for different zenith angles, with *geo* yielding a better angular resolution for small zenith angles and vice versa. In order to obtain the best angular resolution at any given zenith angle, we implemented a new reconstruction method that combines the results from both algorithms, as a function of the zenith angle. For each shower event, the direction is reconstructed using both *geo* and *disp* methods. Then, a weighted average based on the cosine of the zenith angle of each particular event is calculated, which gives the final result for the shower direction. The weighting formula was empirically optimized for the Eventdisplay analysis package, and is expressed as follows [Beilicke, 2010]:

$$direction = geo \times (1 - w) + disp \times w \tag{A.1}$$

where

$$w = \begin{cases} 1 & cos(z) > 0.4 \quad (z > 66.4^{\circ}) \\ e^{-12.5 \times (cos(z) - 0.4)^2} & \text{otherwise} \end{cases} \tag{A.2}$$

A.5 Conclusion and Outlook

The *disp* method improves the angular resolution significantly in the case of LZA data analysis, where shower images tend to be mostly parallel on the camera plane. Another similar case with parallel shower images occurs with 2-telescope events. However, the *disp* method performance is not as successful as expected for high energy 2-telescope events. This is under investigation, and table binning stands out, in particular, as an area that needs to be optimized. In addition, it has been verified that truncated events affect the *disp* performance negatively, since the Hillas parameterization is not as successful in these cases. The next step in this issue is to test the combined HFit and *disp* performance, to see how much it reduces the misreconstructed events by the *disp* method. Another parameter that is worth exploring for the improvement of *disp* reconstruction is the time gradient for each shower event, as recorded by individual telescopes.

Finally, the generation of disp tables is cumbersome, and there is always the problem of low statistics for extreme values of the table parameters. Using boosted decision trees algorithm instead of disp tables could be very useful in improving the accuracy and the practicality of the *disp* method.

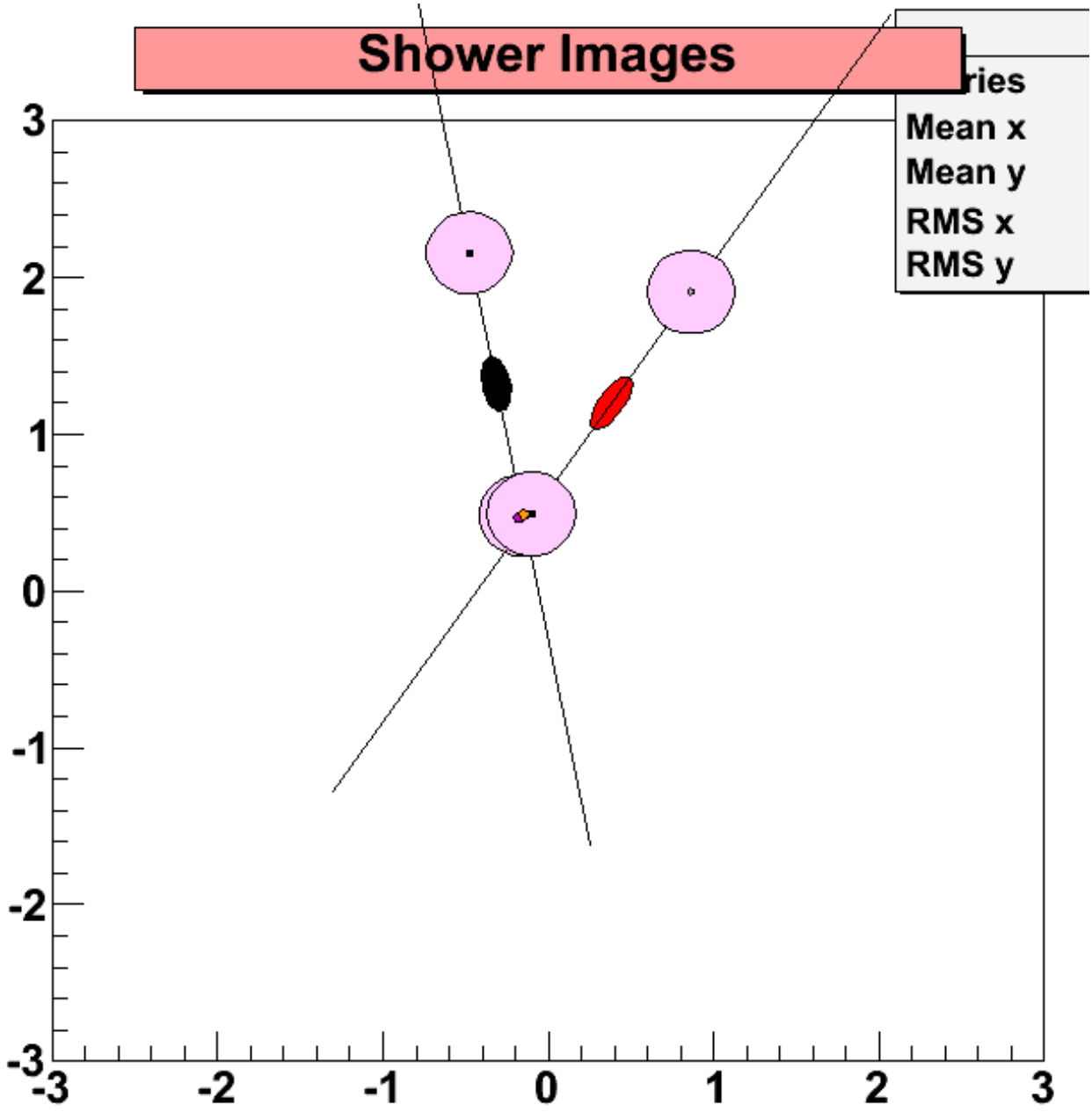

Figure A.3: A simulated gamma event seen by two telescopes. Red and black ellipses represent individual shower images. Two arrival directions are calculated for each shower image, on either side of the ellipse (gray and black dots), resulting in four directions in total, among which the closest two are picked. The weighted average of these two points yields the final result for arrival direction (orange dot). Pink circles represent the error associated with each arrival direction. The magenta dot represents the real arrival direction.

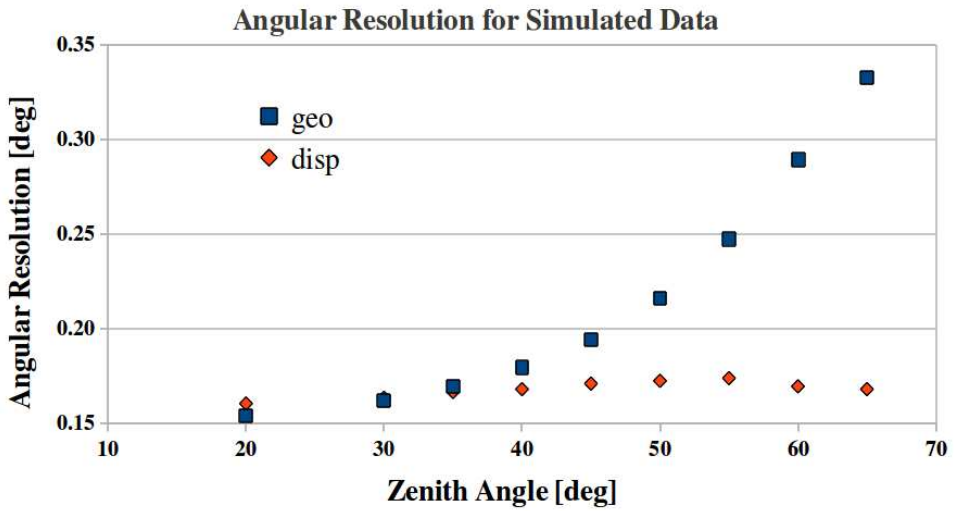

Figure A.4: In the case of the *geo* method, the angular resolution worsens with increasing zenith angle (blue squares). On the other hand, it is largely independent of zenith angle with the *disp* method (red diamonds).

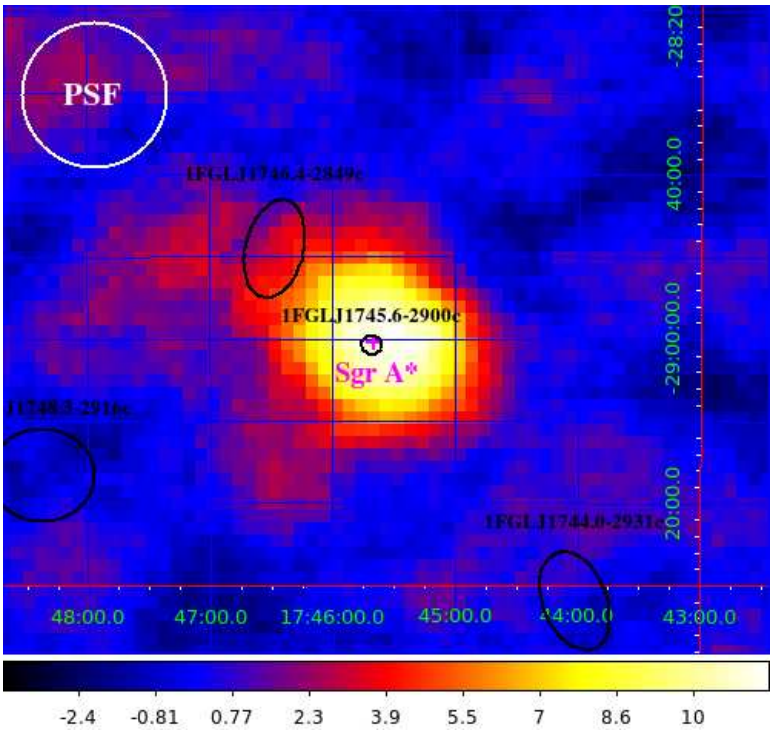

Figure A.5: VERITAS significance map for Sgr A*. *Fermi*-LAT error ellipses are shown in black. The 68% containment radius is 0.13° (White circle at the top left corner).

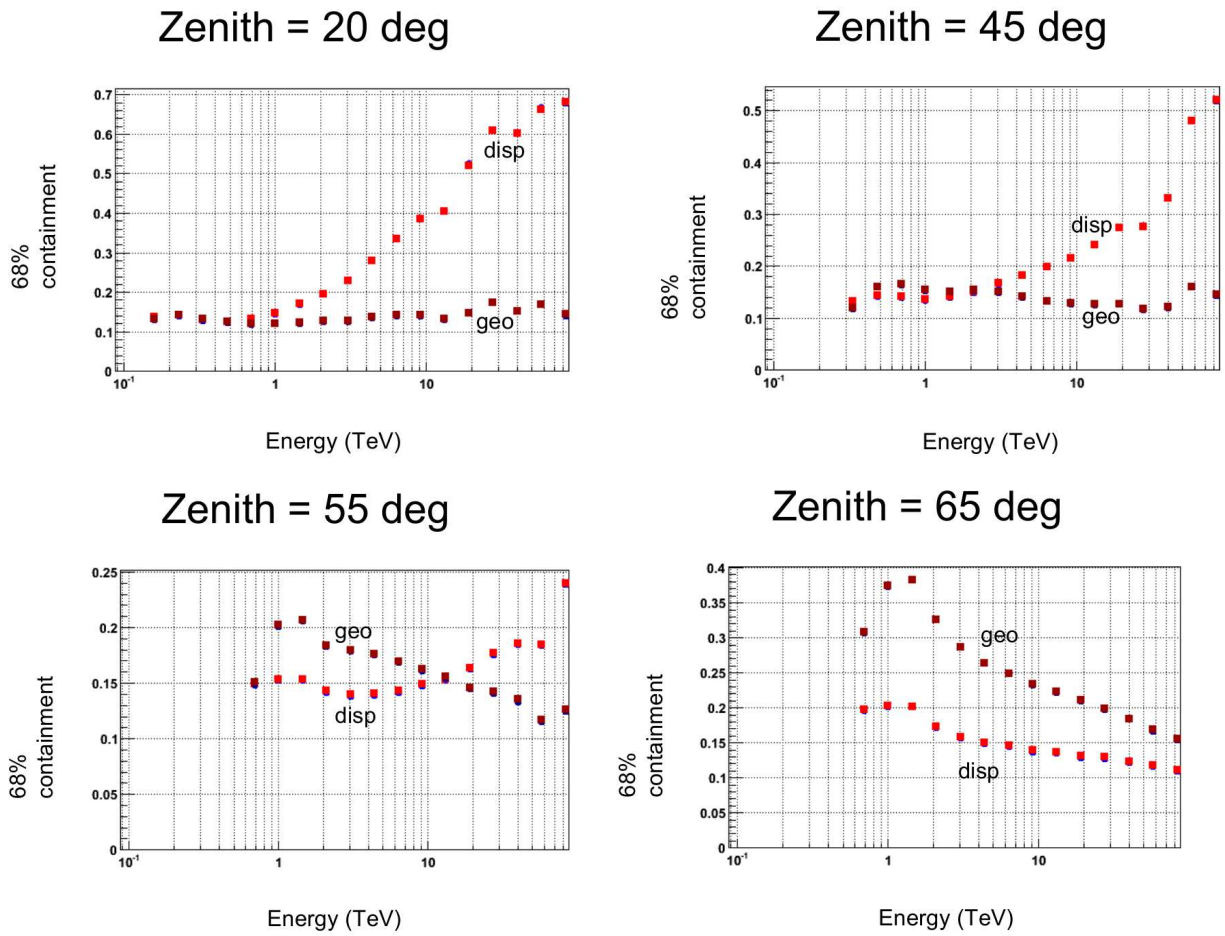

Figure A.6: PSF vs. energy for zenith angles ranging from 0° to 65°.

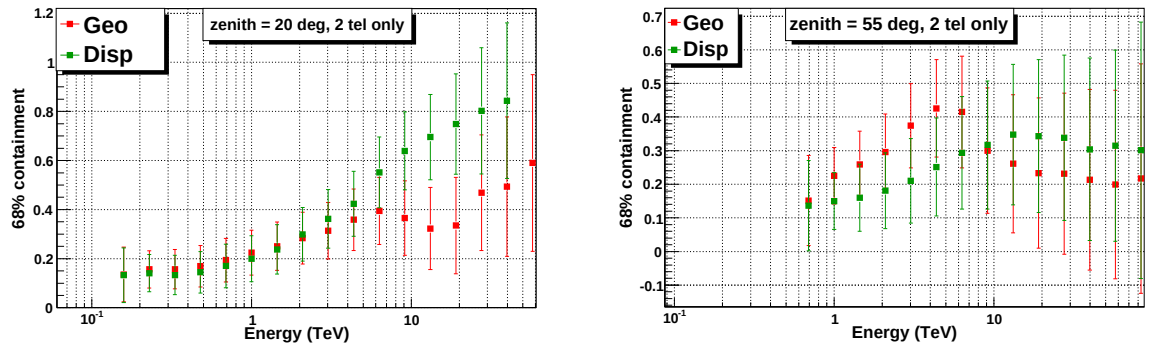

Figure A.7: PSF vs. energy for zenith angles 20° and 55°, for 2-telescope events.

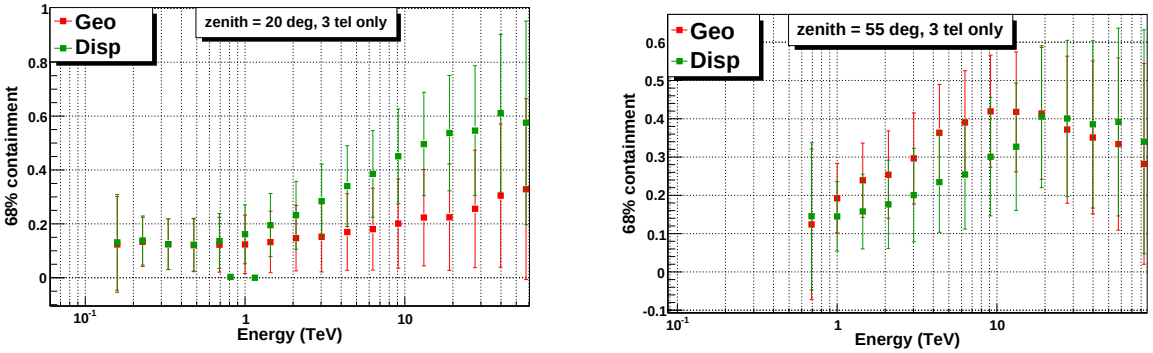

Figure A.8: PSF vs. energy for zenith angles 20° and 55°, for 3-telescope events.

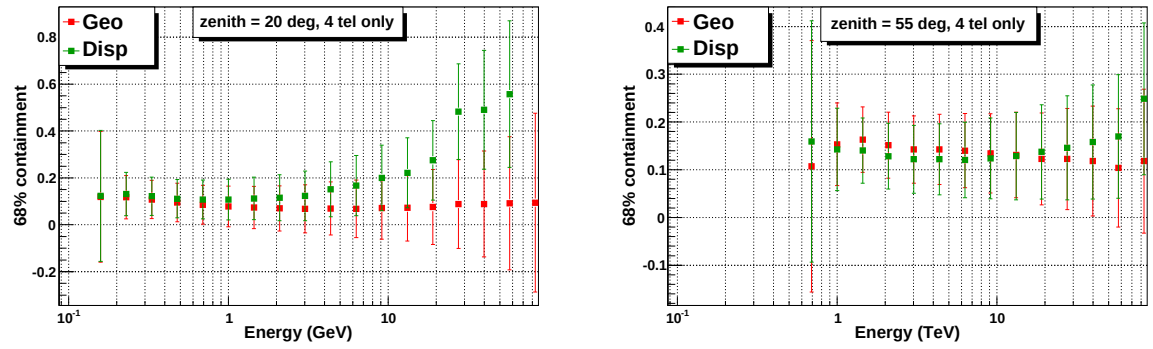

Figure A.9: PSF vs. energy for zenith angles 20° and 55°, for 4-telescope events.

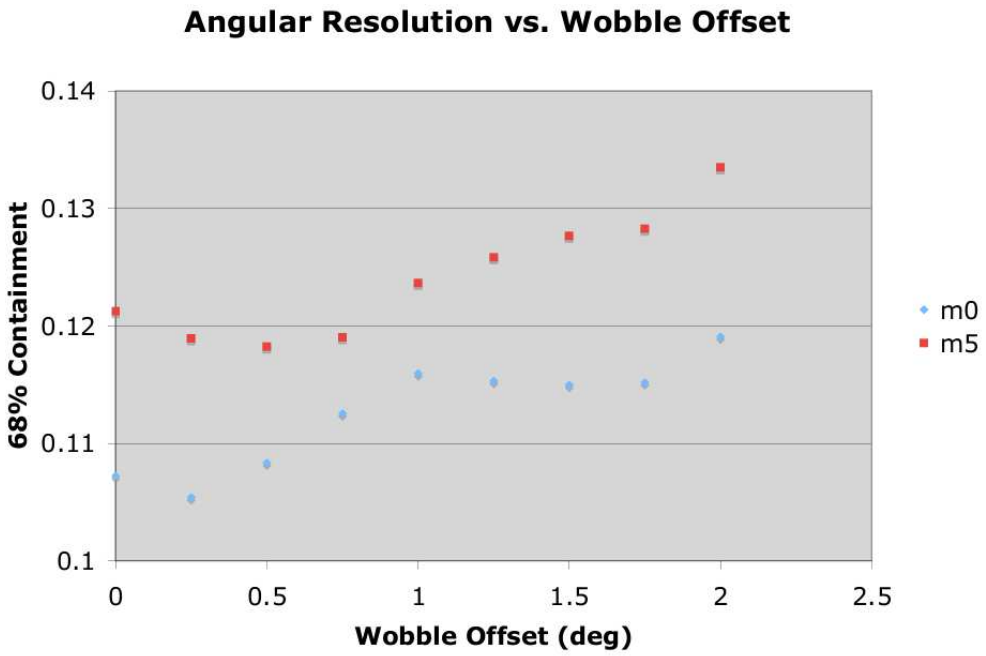

Figure A.10: Angular resolution as a function of the wobble offset, for 20° zenith angle. Red data points represent the *disp* method results and the blue ones the *geo* results. The *geo* method outperforms the *disp* at all offset degrees.

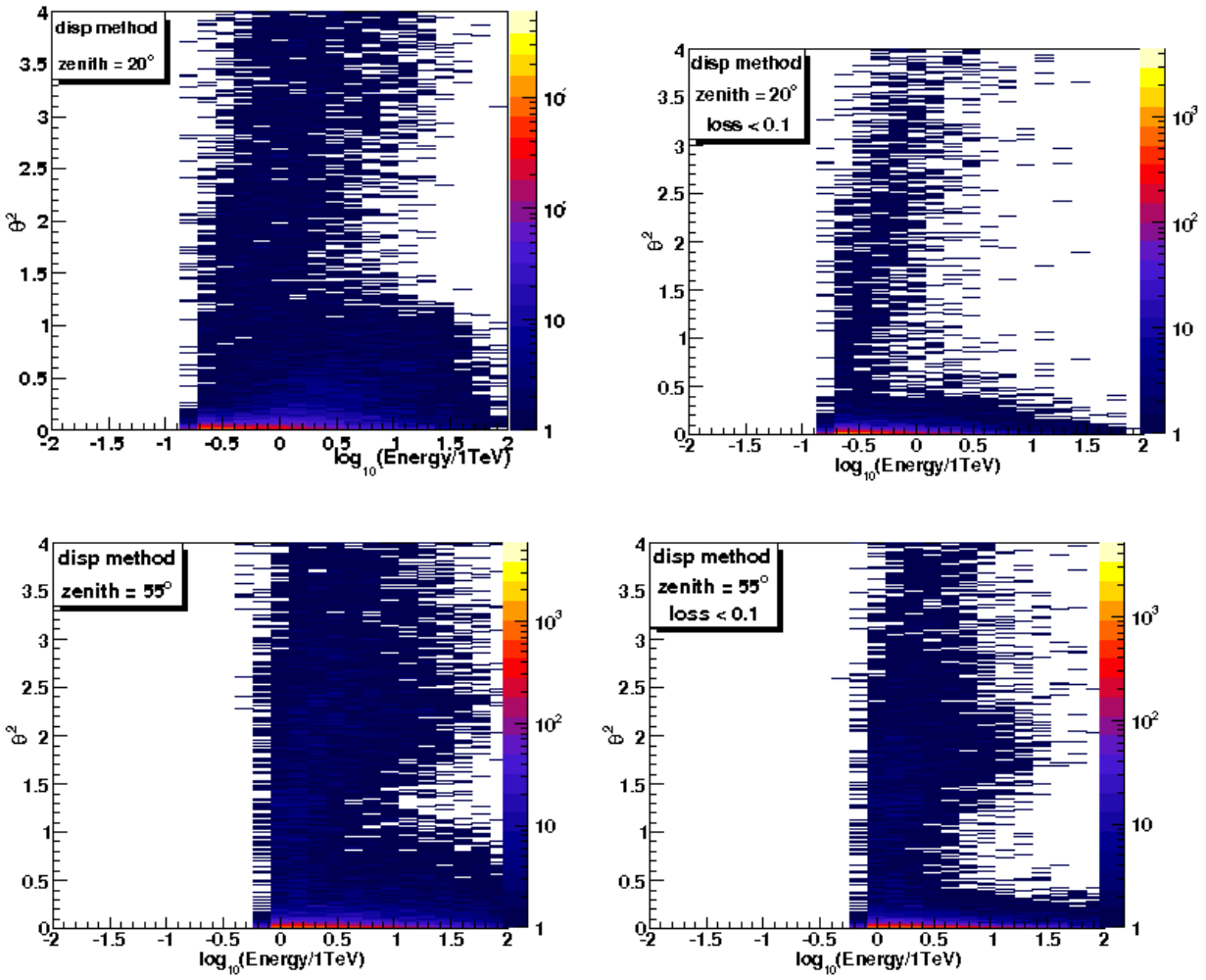

Figure A.11: θ^2 vs. energy for zenith angles 20° and 55°, with (right) and without (left) loss cuts. Introducing a loss cut reduces the fraction of events that are misreconstructed. See the text for the details.